University of Alberta

Numerical Simulation of Thin Liquid Film Drainage Under the Influence of Pressure and Electrical Forcing

by

David Glen Crawford 

A thesis submitted to the Faculty of Graduate Studies and Research in partial fulfillment of the requirements for the degree of Master of Science.

Department of Mechanical Engineering

Edmonton, Alberta

Spring 2008

Your file Votre référence
ISBN: 978-0-494-45799-3
Our file Notre référence
ISBN: 978-0-494-45799-3

Abstract

Thin liquid films are encountered in a broad spectrum of physical systems, and have been widely studied. Recently, thin films have become relevant in novel nano-fabrication applications. The primary objective of this study was to develop a mathematical model of film drainage in presence of pressure and an electric field to elucidate the patterns that can form under different types of forcing.

A 'long-wave' asymptotic analysis was used to condense the governing fluid and electrostatic equations into a single partial differential equation for film thickness. A numerical solution of the highly non-linear equation was obtained using finite differences in space and a differential algebraic solver in time.

A large parametric phase-space was explored to elucidate the influence of forcing, frequency of the periodic heterogeneity, and relative orientations of the chemical and electrical heterogeneity on the drainage dynamics and the ensuing quasi-equilibrium structures of the film.

Acknowledgements

I would like to take this opportunity to acknowledge the following individuals and groups who helped me during the course of this work.

Dr. Bhattacharjee for his selfless contribution of time, insight and invaluable wealth of knowledge.

Dr. Koch for his insight, knowledge, encouragement and financial support.

The Natural Science and Engineering Research Council for their generous financial support.

Thanks to my colleagues in the Complex Fluids and Colloids research and in the Thermo-Fluids, Engines and Controls laboratory for their valued technical advice and laughs over coffee. My parents for their continued love and encouragement throughout all of my challenges, academic or otherwise.

Table of Contents

List of Tables

List of Figures

NOMENCLATURE

Note that $\bar{}$ denotes a vector quantity. The double bar $\bar{\bar{}}$ indicates a tensor. Bold face denotes a matrix.

Roman symbols:

A_L, A	Effective Hamaker constant that accounts for interactions between the lower surface, surrounding fluid and fluid interface through the fluid film [J]
A_U	Effective Hamaker constant that accounts for interactions between the upper surface, surrounding fluid and fluid interface through the fluid film [J]
B_L	Born-like close range repulsion constant at lower surface $[J/m^6]$
B_U	Born-like close range repulsion constant at upper surface $[J/m^6]$
C_n	Scaling for the unit normal vector $[m]$
C_{t1}	Scaling for the 1^{st} unit tangent vector $[m]$
C_{t2}	Scaling for the 2^{nd} unit tangent vector $[m]$
$\vec{D}$	Electric displacement $[C/m^2]$
$\vec{E}$	Electric field $[MV/m]$
E_p	Electric field at fluid interface $[MV/m]$

G	Functional representation of the interface between the two fluids [-]
H	Non-dimensional film thickness [-]
$\bar{\bar{I}}$	Identity tensor [-]
K_c	Critical wave number [-]
L	Domain length $[m]$
L_p	Periodicity of striped pattern (center to center distance of adjacent stripes of the same type) $[m]$
$\vec{P}$	Dielectric polarization $[C/m^2]$
P	Normalized pressure [-]
$\bar{P}$	Modified non-dimensional pressure [-]
P_{ext}	Pressure in surrounding fluid $[Pa]$
R	Radius of curvature $[R]$
Re	Reynolds number of the thin film [-]
T	Non-dimensional slow time [-]
U	Non-dimensional x component of $\vec{u}$ [-]
V	Non-dimensional y component of $\vec{u}$ [-]
W	Non-dimensional z component of $\vec{u}$ [-]
X	Non-dimensional cartesian coordinate [-]
Y	Non-dimensional cartesian coordinate [-]

Z	Non-dimensional cartesian coordinate [-]
d	Spacing between upper and lower surface. Also called electrode spacing in electrostatic cases $[m]$
$\vec{f}$	Body forces applied to the liquid film $[N]$
$\vec{f}_e$	Surface forces applied to the liquid film $[N]$
h	Film thickness $[m]$
h_0	Initial film thickness $[m]$
k	Scaling factor used in long wave asymptotic analysis $[-]$
l_0	'Absorbed Layer' thickness $[m]$
$\vec{n}$	Normal unit vector [-]
n_x	Normal unit vector x component [-]
n_y	Normal unit vector y component [-]
n_z	Normal unit vector z component [-]
p	Pressure in liquid film $[Pa]$
t	Time $[s]$
t^*	Scaling time $[s]$
$\vec{t^j}$	Unit tangential vector [-]
t_x^j	Unit tangential vector x component [-]
t_y^j	Unit tangential vector y component [-]

t_z^j	Unit tangential vector z component [-]
$\vec{u}$	Velocity $[m/s]$
u	x velocity component $[m/s]$
u_0	Scaling velocity $[m/s]$
v	y velocity component $[m/s]$
w	z velocity component $[m/s]$, Width of stripe with lower applied electric field or effective Hamaker constant patterning [-]
w_1	Width of stripe with higher applied electric field of effective Hamaker constant patterning [-]
x	Cartesian coordinate $[m]$
x^*	Scaling length $[m]$
y	Cartesian coordinate $[m]$
z	Cartesian coordinate $[m]$

Greek symbols:

$\bar{\bar{\delta}}$	Kronecker delta [-]
ψ	Electric potential $[V]$
$\bar{\psi}$	Non-dimensional electric potential [-]
ψ_{up}	Electric potential on upper electrode $[V]$
ψ_{low}	Electric potential on the lower electrode $[V]$

ϵ_0	Permittivity of free space $[F/m]$
ϵ	Relative permittivity [-]
μ	Viscosity $[Pa\ s]$
γ	Interfacial tension $[N/m]$
$\bar{\gamma}$	Long-wave interfacial tension $[N/m]$
λ	Length of the dominant disturbance used in the long wave asymptotic formulation $[m]$
λ_c	The length of a critical disturbance as predicted by linear theory $[m]$
ϕ	Conjoining/Disjoining pressure $[Pa]$
Φ	Non-dimensional conjoining/disjoining pressure [-]
ρ	Fluid density $[kg/m^3]$
ρ_f	Density of free charge carriers $[C/m^3]$
κ	Interfacial curvature $[m^{-1}]$
$\bar{\bar{\sigma}}$	Fluid stress tensor $[Pa]$
$\bar{\bar{\sigma^M}}$	Maxwell stress tensor $[Pa]$
Ψ	Thin film intermediate variable [-]
Δ	Mesh point spacing [-]
∇	Cartesian gradient operator

Miscellaneous:

1	Subscript: Liquid Film in Mathematical formulation. Also used to indicate different values for patterning.
2	Subscript: Bounding Fluid in Mathematical formulation. Also used to indicate different values for patterning.
ES	Subscript: Electrostatic Component
$LVDW$	Subscript: Lifschitz van der Waals Component
BU	Subscript: Close Range Repulsive Constant for Lower Surface
BL	Subscript: Close Range Repulsive Constant for Upper Surface
L	Subscript: Interactions that Account for Interaction with the Lower Surface
U	Subscript: Interactions that Account for Interaction with the Upper Surface
i	Subscript: Counter that Indicates Different Domains
(i,j)	Subscript: Location in the Mesh where i represents the i^{th} row and j indicates the j^{th} row.
T	Superscript: Tensor Transpose
j	Superscript: j^{th} Unit Tangent Vector

Chapter 1

Introduction

1.1 Thin Film Dynamics

Thin liquid films occur in a wide range of biological, physical and engineering systems, such as cell membranes, foams, emulsions, paints, and coatings. When such films are subjected to mechanical, thermal, chemical, or structural perturbations, they can experience a diverse range of dynamics such as wave propagation, wave steepening, and chaotic responses. The films may or may not rupture, holes or dry spots may form, and other complicated structures may result. The phenomena that govern the dynamics of thin films are different than those in typical bulk fluids and present unique challenges [Oron et al., 1997]. In thin films, with thickness < 100 nm, fluid molecules interact not only with surrounding fluid molecules (as in a typical bulk environment) but also the surrounding molecules of other materials [Sharma and Jameel, 1993, Ruckenstein and Jain, 1974]. The intermolecular interactions that occur between the fluid molecules in a thin film and the surrounding materials are commonly referred to as excess intermolecular interactions. The strength and range of the inter-

molecular forces depend on the physical and chemical properties of the system, and are predominantly classified as the Lifshitz van der-Waals (LVDW), electrostatic, and polar interactions [Sharma and Jameel, 1993]. The excess intermolecular interactions result in a conjoining/disjoining pressure, which causes film drainage [Verma et al., 2005, Wu et al., 2005].

When an electric field is applied normal to a film interface, a pressure is produced in the film similar to that generated by excess intermolecular forces [Verma et al., 2005]. In recent years, electric fields have gained popularity in the actuation and induction of thin film dynamics. The use of electric fields in film drainage allows for greater adaptability and control in the conjoining/disjoining pressure that the film experiences. The use of thin polymer films in micro and nano-fabrication has gained popularity since the work of

1.2 Technological Applications

Thin films are present in a wide range of physical systems. Knowledge of film dynamics is useful in the study of biological films, such as the mucosal coatings of the lung or in the study of adhesion and coatings. Thin films also occur in various chemical processes and are important in foam dynamics. Thin films are used to control heat and mass flux and to protect surfaces. They are important in membranes and paints. Various polymer manufacturing techniques use thin polymer films to create desired structures for biomedical and micro-electro-mechanical (MEM) applications. These applications include Electro-Hydrodynamic Lithography (EHD),

Lithography Induced Self Assembly (LISA), and Lithography Induced Self Construction (LISC) [Schaffer et al., 2000, Wu et al., 2006]. EHD is of interest due to its wide array of potential application in micro and nano scale fabrication. As the fields of MEMS and biomedical engineering have grown, so have their requirement for new and diverse fabrication methods. EHD is promising for MEMS and biomedical fabrication because of its adaptability and small length scales for which it is applicable. EHD can produce structures of scale less than 100 nm, a scale which typically limits optical lithographic methods [Schaffer et al., 2000].

A sample EHD configuration is shown in Figure 1.1. In EHD, an electric field is applied normal to the surface of the thin film. The upper electrode is patterned and the pattern produces a spatially heterogenous non-uniform electric field. The difference in applied electric field creates a pressure gradient that induces fluid motion and creates a pattern in the film.

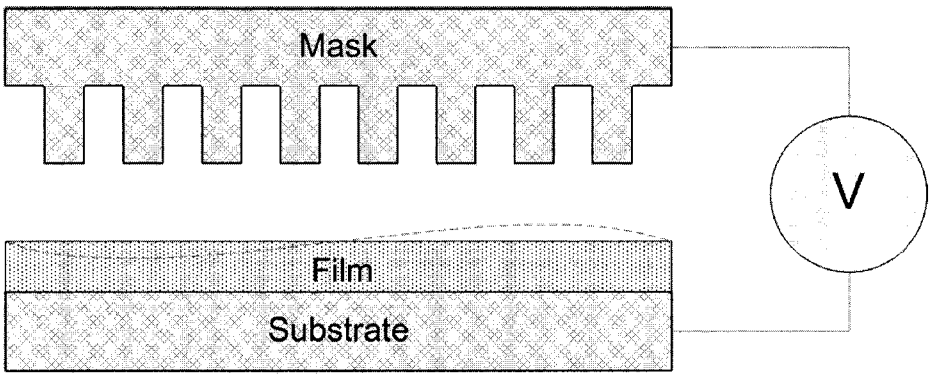

Figure 1.1: Schematic representation of a typical electrohydrodynamic lithography (EHD) cell: The application of an electric field allows the replication of a structure patterned on the mask (upper capacitor plate).

Unfortunately, the dynamic behaviour of thin films under the influence of electric fields and excess intermolecular forces is not well understood. The fluid flow that

occurs is called the films 'drainage' and may produce a variety of different structures. The variety of forces that can exist and the different length and time scales of the film drainage make the study of thin films difficult. A better understanding of the underlying physics of thin films and how transitions between dominant and competing phenomena occur is of importance for future understanding and future efficient application of this technology.

1.3 Thin Fluid Film Interface Dynamics

The premise of the thesis is the study of the drainage of a thin liquid film. Through a numerical model, the drainage behaviour is studied under a broad range of conditions, including drainage of films on chemically homogeneous and heterogeneous substrates, drainage in the presence of an applied electric field, which can either be homogeneous or heterogeneous, and finally, drainage in the presence of combined chemical and physical heterogeneity. Here, the fundamental aspects of the thin film drainage problem formulation are briefly outlined.

A thin liquid film resting on a homogenous substrate with a second inactive medium above may become unstable due to small perturbations to the system. These small perturbations begin to grow in waves that have lengths much larger than the mean film thickness. The chemical, electrical and fluid mechanical properties of the fluids and substrate determine the character of the deformation. Figure 1.2 shows a representative schematic of a thin fluid film placed between two electrodes depicting the perturbed interface between the film and bounding fluid. The bounding fluid will

be modeled as chemically and physically inert. The perturbation can be caused by various means, but in this work, the focus will primarily be on the situation where an electric field is applied between the two electrodes. The film drainage induced by spatial heterogeneity in chemical properties or applied electric field will also be studied. The upper electrode will be treated as chemically inert, and its interaction with the fluid will be limited to steric interactions.

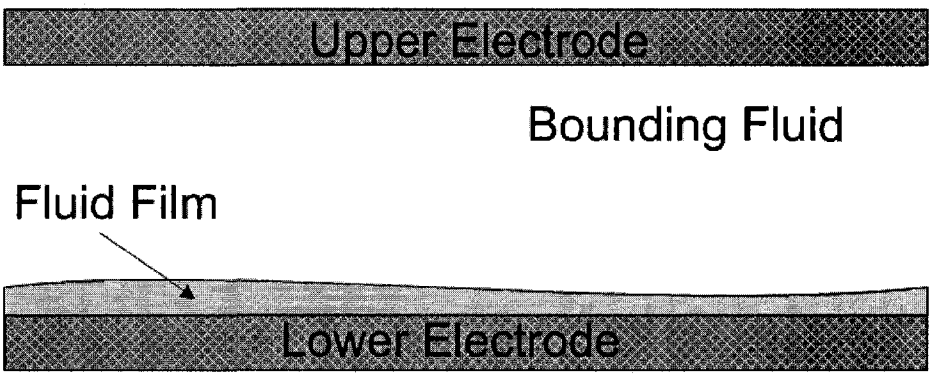

Figure 1.2: Schematic representation of the deformation of a thin fluid film resting on a homogenous surface and sharing an interface with a second inert bounding fluid.

The shape that the free interface between the fluid film and bounding fluid assumes is dictated by a pressure balance within the film. The excess intermolecular interaction can accelerate or retard film rupture. The application of an electric field also induces film motion due to the stress created at the interface. When chemical or electrical heterogeneity exists, a pressure gradient is created in the film, which results in drainage. A comprehensive analysis of the problem would require a coupled solution of the fluid momentum (Navier-Stokes) and continuity equations, along with the appropriate equations describing the imposed force fields. However, the study of thin films takes advantage of the length scale disparity inherent in the system.

The films studied here have thickness between $10 - 100\ nm$, with the length scales of the structures on the interface ranging from $1 - 300\ \mu m$. This allows the use of the so-called 'long-wave' asymptotic procedure [Atherton and Homsy, 1976], and the system can be reduced to a single non-linear partial differential equation (PDE). The study of thin films has been significantly extended by the use of numerical methods, since experimentation is challenging at the length scales required.

This study examines the deformation of an initially planar thin Newtonian liquid film resting on a solid substrate, with a second solid surface at some distance above the film. The film is interacting with a second inert phase above and the two fluids are immiscible. The film is sufficiently thick that the continuum assumption remains valid, but sufficiently thin that the effects of gravity can be disregarded. The films are so thin (thicknesses typically less than $100\ nm$) that excess intermolecular interactions play a role in film dynamics. The film, solid substrates, and inactive surrounding medium will be modeled as perfect dielectric materials, so no free charge carriers are present in the system. The thickness of films studied is maintained below $100\ nm$ to allow LVDW interactions to play a significant role in film drainage. The assumption of an inert upper fluid reduces the numerical complexity, while not dramatically altering the type of drainage observed. The experimental work of [Lin et al., 2001] considers the drainage of a thin liquid film interacting with a second active fluid above. They noted that although the length scales of structures are reduced, the same morphologies generally result from the drainage. The major difference for bi-layers is the increased speed that drainage occurs at, hence, studying a fluid suspended below an inert fluid

is easier to observe experimentally.

1.4 Objectives and Scope

The objectives of this study are:

1. To develop a general numerical model to track the three-dimensional morphology of thin films and the drainage kinetics under a diverse range of imposed perturbations and boundary conditions.

2. To predict the similarities and differences between drainage of thin films solely under the influence of chemical (intermolecular) interactions and externally applied electric fields.

3. To predict the influence of chemical patterning of the solid substrate on thin film drainage.

4. To predict the influence of spatial inhomogeneity of applied electric fields on the film drainage.

5. To study the coupled influence of chemical patterning and electric field inhomogeneity on the drainage kinetics, and morphology of the drained film.

Although the terms heterogeneity or spatial inhomogeneity might have a connotation of randomness, the study uses highly structured periodic patterns as models of chemical and electrical heterogeneity.

This research facilitates an investigation into the behaviour of EHD systems. The dynamics of thin films are difficult to observe experimentally and experimental uncertainty can have a significant impact on the results, since even minor heterogeneity can influence film dynamics significantly. Currently, most EHD and other chemical based lithography methods are carried out independent of one another. It is hoped that this research will help demonstrate that the use of combinations of electrical and chemical patterns will allow for more versatile dynamic fabrication methods. The combination of electrical and chemical patterning has the potential to open new avenues of fabrication.

1.5 Outline of this Dissertation

In Chapter 2, the history of thin film research is reviewed, with important results highlighted. Particular attention is given to the studies of films deforming on chemically and electrically heterogeneous surfaces. A summary of numerical investigations is also provided. The contributions of this thesis in the context of what is reported in the literature is also summarized.

The theoretical basis for this work is examined in Chapter 3, the governing equations are discussed including the fluid mechanics and the electrostatics, then the thin film equation is derived from the governing equations. A discussion of body forces follows and the section is completed by a discussion of length scales. The numerical method is detailed in the second part of the chapter. It shows the finite difference approximations, the interpolation scheme, the boundary condition application and

the general numeric algorithm employed.

The first component of Chapter 4 is a comparison of the forcing created by electrostatic and intermolecular forces. Pressure based film drainage is presented initially. These results are contrasted in the next section with electrostatic dominated drainage results. Validation cases for the numerical technique are presented in conjunction with the film drainage results. The results of the numerical simulations are compared with linear and non-linear theory, and found to accord well with reported results. Testing of the numerical method against similar computational techniques is carried out.

In Chapters 5 and 6, heterogeneous substrates with chemical and electrical patterning are considered, respectively. In both chapters, the influence of heterogeneity is first investigated by considering how a spatial step in chemical or electrical properties influences film drainage. The study is then extended to consider more complex patterns on the substrate and how they influence the film dynamics. The results are then compared based on pattern replication and length scales. In Chapter 7, combined chemical and electrical patterning is considered. The similarities and differences with either individual case are compared and noted.

In Chapter 8, conclusions are drawn and future research avenues discussed.

Chapter 2

Literature Review

2.1 Theoretical Studies

Microscopic liquid films have been studied in science and engineering for many years due to their presence in a wide array of physical systems [Oron et al., 1997]. They occur in biophysical systems such as films that occur in the lungs [Grotberg, 1994] or tear films in the eyes [Sharma and Ruckenstein, 1986]. In engineering systems, they occur in many different applications such as coatings, membranes, Micro-Electro Mechanical (MEMs) system and foams [Oron et al., 1997]. The initial theoretical studies of thin films were theoretical and used linear stability analysis to predict film motion after a small perturbation.

2.1.1 Linear Stability

One of the first theoretical explorations of thin films used linear stability to model film drainage [Ruckenstein and Jain, 1974]. Ruckenstein and Jain studied the rupture of a thin fluid film with an inactive medium above, resting on a solid substrate. The

authors used the slow nature of the films' dynamics to simplify the Navier-Stokes equations and the large relative length of the disturbance to the film thicknesses to warrant the use of a lubrication approximation. The film stability to small periodic perturbations was studied using a linear stability analysis. The stability analysis uses superposition of the films Fourier components of interface displacement around equilibrium state to predict whether film rupture will occur. Films with active surface agents, thin films, and free films all have the stability parameters established based on linear theory. One of the main contributions of this work was the definition of the body force term (conjoining/disjoining pressure) in the Navier-Stokes equations due to extra intermolecular forces.

The excess intermolecular forces [Ruckenstein and Jain, 1974] due to Lifshitz London van der Waals (LVDW) and double layer forces were considered by Ruckenstein and Jain and a form that has become the standard for thin films was derived. The body force term, called the conjoining/disjoining pressure, is added to the NS equations to account for the difference between a thin film and a typical bulk liquid. In the thin film, intermolecular interactions between the solid, gas and liquid are significant, while the intermolecular interactions of a liquid with itself are typically not. This body force is the derivative of a potential energy function that accounts for the molecular difference previously described.

Ruckenstein and Jain start from classic theory for LVDW forces by modeling the potential energy of interaction for a solid surface and a single liquid molecule. The solid surface is modeled as being semi-infinite and the final form of interaction

potential energy per unit volume of fluid as:

$$\phi_0 = \phi_B + \frac{A}{6\pi h^3} \tag{2.1}$$

Where ϕ_0 is the interaction energy per unit volume of the liquid, ϕ_B is the interaction energy between a liquid molecule at the solid surface, A is the effective Hamaker constant $A = A_{11} - A_{12}$, where A_{11} is the Hamaker constant for a liquid-liquid interactions and A_{12} is the Hamaker constant for liquid-solid interactions. The work of Ruckenstein and Jain captured the linearly predicted film dynamics and the dominant length and time scales for a number of film configurations. Subsequent to the work of Ruckenstein and Jain the mathematics used in theoretical modeling of thin films was simplified by the work of [Atherton and Homsy, 1976] using the theory of [Benney, 1966].

The basis of the majority of theoretical studies of thin film dynamics employ a 'long-wave' asymptotic expansion to simplify the governing Navier-Stokes equations. The 'long-wave' asymptotic method was first developed by [Benney, 1966] for a thin film flowing down an inclined plane. Benney used a shallow water parameter k that related the film thickness to the length of the characteristic disturbance. This parameter was used to expand the stream and pressure functions:

$$\psi(x,y,t) = \psi^{(0)}(x,y,t) + k\psi^{(1)}(x,y,t) + k^2\psi^{(2)}(x,y,t) + ... \tag{2.2a}$$

$$P(x,y,t) = P^{(0)}(x,y,t) + \mu P^{(1)}(x,y,t) + k^2 P^{(2)}(x,y,t) + ... \tag{2.2b}$$

Where ψ is the stream function and P is the pressure in the fluid flow. These expansions are then combined with a relation for the fluid thickness and a single partial differential equation in terms of the fluid thickness is derived. This formulation is the basis for the 'long-wave' theory used for the thin film equations studied by future authors. The form of the thin film equations in terms of pressure and velocity were first presented by [Atherton and Homsy, 1976].

The first authors to use a 'long-wave' analysis for a thin film on a uniform solid substrate were [Atherton and Homsy, 1976]. They presented a general study of wave motion of fluid interfaces in multi-phase systems. As part of there study they consider the dynamics of a thin film resting on a solid substrate that is perturbed with a periodic disturbance. They use the 'long-wave' theory demonstrated by [Benney, 1966] to simplify the Navier-Stokes equations and derive a single partial differential equation for the film thickness (h). They presented a frame work for the derivation of film evolution equations that has been followed by many authors since [Williams and Davis, 1982, Oron et al., 1997, Khanna and Sharma, 1997]. Benney and Atherton and Homsy established a frame work for the study of thin liquid films that has since been employed by a variety of authors. The first theoretical studies after the work of Atherton and Homsy focused on film stability and dynamics to predict rupture time.

2.1.2 Non-linear Stability

The work of [Sharma and Ruckenstein, 1986] presented a non-linear stability analysis for both wetting and free films. The study focused on the definition of dominant

wave lengths, time scales and times to fluid rupture in thin films. They note that non-linear analysis is required since linear theory requires the use of small amplitude perturbations which are not physically realistic. The study concludes that the predictions of linear theory are only valid initially during film evolution. The predictions of the non-linear stability analysis employed show that linear stability analysis fails to predict accurately time or length scales of film motion. The non-linear theory predicts faster film thinning and shorter dominant wave lengths for the majority of cases. This analysis demonstrated that linear theory is not sufficient in predicting film dynamics. The study by Sharma and Ruckenstein used a form of the conjoining/disjoining pressure similar to that shown by [Ruckenstein and Jain, 1974], but this formulation leads to a singularity when films completely de-wet a surface (form dry spots). The general form of the intermolecular interaction used can be seen in equation (2.1). The conjoining/disjioning pressure is a function of h^{-3} so becomes undefined as the film nears complete drainage ($\phi \rightarrow \infty$ as $h \rightarrow 0$). Modeling of film de-wetting and an appropriate definition of conjoining/disjoining pressure was addressed by [Mitlin, 1993].

The study of film dynamics, both numerical and theoretically was initially limited to times up to the initial film de-wetting. This was due to the form used for the films conjoining/disjoining pressure. When the conjoining/disjoining pressure is model by an LVDW dominated term as seen in equation (2.1) it has the potential of generating physically unrealistic results if left unchecked. This was until the work of [Mitlin, 1993] who proposed the use of an 'absorbed layer' model. In the 'absorbed layer'

model the singularity that typically occurred at a point of drainage was prevented by assuming that some small portion of fluid always remained on the solid surface. In the 'absorbed layer' model Born close range repulsive forces are considered and they prevent complete drainage from occurring [Mitlin, 1993]. The Born close range forces preserve a fluid layer along the solid substrate of some thickness (l_0). The excess intermolecular forces are well described for all times of film evolution by:

$$\phi(h) = \frac{B}{h^9} + \frac{A}{h^3} \tag{2.3}$$

where B is the Born repulsion constant, and A is the effective Hamaker constant ($A < 0, B > 0$ in Mitlin's formulation). The film layer thickness (l_0) is determined by the chemical properties of the film and solid substrate. The Born constant B is found by setting the conjoining/disjoining pressure to zero at the 'absorbed layer' thickness $\phi(h = l_0) = 0$. Use of the 'absorbed layer' model allows long time modeling of thin film dynamics.

2.2 Numerical Studies

The first numerical simulation of non-linear thin film dynamics was performed by [Williams and Davis, 1982]. In their study the dynamics of a thin film in $2D$ using the 'long-wave' model assumptions of [Atherton and Homsy, 1976] to derive a single partial differential equation that defined the interface dynamics. The thin film equation was solved using central differences in space and the midpoint rule in time. The conjoining/disjoining pressure used by Williams and Davis was that of [Ruck-

enstein and Jain, 1974], so they did not have a way of dealing with the singularity created by complete drying of the film. This limited there simulations to the point of complete drainage ($h = 0$). They demonstrated that linear theory even for small amplitude perturbations (0.1% h_0) still does not accurately predict the time scales of the dynamics or the time taken for film drainage. Williams and Davis were the first authors to study non-linear film dynamics numerically and many authors followed. The results of Williams and Davis were reaffirmed by the numeric study of [Sharma and Jameel, 1993].

The numeric work of [Khanna and Sharma, 1997] was one of the first to numerically solve for $3D$ film morphologies. The film is modeled using the 'absorbed layer' form of conjoining/disjoining pressure as suggested by [Mitlin, 1993]. The non-dimensional thin film equation took the form:

$$\begin{aligned} \frac{\partial H}{\partial T} + \frac{\partial}{\partial X}\left[H^3 \frac{\partial \Psi}{\partial X}\right] + \frac{\partial}{\partial Y}\left[H^3 \frac{\partial \Psi}{\partial Y}\right] &= 0 \\ \Psi = \frac{\partial^2 H}{\partial X^2} + \frac{\partial^2 H}{\partial Y^2} - \frac{1}{3H^3}\left[1 - \left(\frac{l_0}{H}\right)^6\right] & \end{aligned} \tag{2.4}$$

where H is the non-dimensional film thickness and Ψ is an intermediate function used to simplify writing of the film equation. The study focused on the large scale structures that occur as a film drains. The film rapidly evolves from random perturbations (imagined as thermal noise) to large scale structures which eventually lead to the formation of circular holes. The study presents scaling arguments for film dynamics based on linear theory. A critical wave length λ_c is found for waves on the surface of the film. If wave exist with lengths above this value then the film will

break down, otherwise it will return to a stable state. This theory was demonstrated by performing simulations on different domain sizes. When the domain size was less then the critical length drainage would not occur and the film would return to a flat state, but if it was larger then drainage would result in the formation of a dimple in the film surface that grew until it de-wet the film from the lower surface creating a dry spot or hole. [Khanna and Sharma, 1997] is used to validate the numeric results for pressure based drainage.

In two complimentary papers [Sharma and Khanna, 1998, Sharma and Khanna, 1999] $3D$ film evolution are studied numerically . They use a $2D$ equation for film thickness $H = H(x, y)$, similar to equation (2.4), to numerically simulate the full $3D$ dynamics of film evolution. Intermolecular forces are modeled using LVDW forces and (relatively) short range interactions using a term similar to the first term in equation (2.3) [Sharma, 1993]. Two separate possible pathways of film evolution subjected to the LVDW and short range molecular interactions are reported. The first is for films that are thick enough ($h > 8\ nm$) that the short range interactions are not significant. For these films circular holes are formed which develop uneven rims and eventually coalesce to form networks of film intermingled with dry areas. For thin enough films ($h < 8\ nm$) the influence of close range intermolecular interactions occur during the entire film evolution. Thus, these films rupture by spontaneously breaking into a series of circular drops. These results match well with experimental results reported by such authors as [Xie et al., 1998, Reiter et al., 1996, Zhao et al., 1993]

The works of [Sharma and Khanna, 1998, Sharma and Khanna, 1999] present

discussion of the potential benefits of topographic (surface patterns) and chemical patterning. They noted that de-wetting of a thin film (rupture), occurs as a function of the minimum of the the conjoining/disjoining pressure (ϕ). On a heterogeneous surface more then one local minimum can exist and as a result combinations of de-wetting mechanisms may co-exist. The authors also point out that in most experimental studies the system is subject to some heterogeneity and as a result the presence of a combination of de-wetting mechanisms should be expected. They also note that the use of linear theory by experimentalists is very common and the short comings of linear theory are again reiterated.

2.3 Experimental Studies

2.3.1 Film Drainage

The use of numerical and theoretical studies is important in understanding the physics of thin films, but experimental results are required to validate theory. In the experimental study of [Zhao et al., 1993] thin film dynamics of various polymer melts was observed. The film thickness and roughnesses were studied using X-ray reflectivity and the film morphologies were observed using atomic force microscopy. The study concludes that polymers that would typically wet a surface will de-wet if there thickness is less then the radius of gyration of the polymer blend (R_g). The drainage morphologies produced for different thickness of films show striking similarities to the morphologies shown in the numerical studies of [Sharma and Khanna, 1998, Sharma and Khanna, 1999]. This demonstrates the utility of thin film theory to model the film

dynamics of polymer melts. Zhao proposed a formulation for the conjoining/disjoining pressure for polymer melts. A thermal term was added to the excess intermolecular terms. The thermal term accounts for the induced dynamics of changing temperature, which are significant for polymer films.

The experimental study of [Xie et al., 1998] observed the de-wetting of polymer films of various thicknesses. They discuss the stipulation of other authors that de-wetting by hole growth only occurs as a results of chemical imperfections in the system [Bischof et al., 1996]. [Xie et al., 1998] report two distinct paths to de-wetting. The first occurs in thick films where holes are formed which then interact and coalesce. In the second de-wetting path, which occurs in thinner films ($h \leq 100\dot{A}$), where surface undulations occur and grow until they reach a scale on the order of the initial film thickness at which point the film breaks into droplets. These two pathways to film rupture are in agreement with the rupture mechanisms proposed by [Sharma and Khanna, 1998] based on numerical simulation. [Xie et al., 1998] also noted that at later times the holes in the films coalesce and form droplets through this coalescence process.

2.4 Chemical and Topographical Patterning

The use of chemical and topographical patterning (where a height difference is induced in the film by an underlying pattern engraved into the surface that the film lies on) are areas of active research. Chemical patterning has the potential to allow formation of structures on length scales that cannot be achieved by other traditional micro and

nano fabrication methods [Schaffer et al., 2000].

2.4.1 Numerical Studies

[Kargupta et al., 2000] presented a numerical study of thin film dynamics on chemically patterned substrates. The authors report a number of morphological phenomena that occur in heterogeneous cases that do not occur on homogenous surfaces. These phenomena include, abrupt film rupture which occurs without any surface waves, the formation of different distinct patterns on different parts of the substrate and a 'castle and moat' structure of a drop surrounded by a depression. The influence of chemical heterogeneities on the evolution time of film dynamics shows little dependence on the initial film thickness. This results in chemical patterning having a greater influence on thicker films. The authors also note that the presence of chemical heterogeneity can create significant changes in times scales which can change by up to two orders of magnitude.

Stripes of alternating wettability, were studied numerically by [Kargupta and Sharma, 2001] to find limits of size and periodicity for 'perfect' pattern replication. The study focused on determining when a bounded film would ideally take on the chemical pattern applied to the lower surface. The study is parameterized by considering the stripe periodicity (L_p) which is the center to center distance of consecutive stripes, and the width of the less wettable stripe (W). They found that there were limits on the stripe periodicity. If the periodicity became too small, the stripes would be ignored by the fluid and only randomly distributed sites separated by $\lambda_h \sim \lambda$ would

de-wet. The length scales given are the dominant length of disturbance for heterogeneity (λ_h) and dominant length scale for homogeneous films (λ) based on linear theory. For ideal templating with contact lines remaining close to stripe boundaries the stripe periodicity must exist in the interval $\lambda_h < L_p < 2\lambda_h$. The stripe width must lie between a critical width (W_c) that results in heterogenous rupture but below a transition width (W_t) where the de-wetting occurs at the center of the less wettable stripe. The numerical results of [Kargupta and Sharma, 2001] are compared to the numerical results produced in the current work.

2.4.2 Experimental Studies

In the experimental work of [Rockford et al., 1999] the drainage of polymer films was studied on chemically patterned substrates. The chemical heterogeneity generated was alternating silicon oxide (polar) and gold (non-polar) stripes. The authors present results on how the polymer length and there interaction on chemical patterning. They conclude that the polymers obtain a very ordered structure in cases of chemical striping even when de-wetting does not occur, if the length scales of the polymer and surface pattern are similar. The substrate pattern will produce good pattern replication if it is within 25% of the dominant length scale for the polymer. The results of [Rockford et al., 1999] are used as a basis of reference for discussion of some of the numerical results produced.

In the work of [Sehgal et al., 2002] the influence of polymer film thickness, pattern scale and long time evolution are studied. The authors show that the influence of

chemical patterning is largely independent of film thickness and have a larger influence on thicker films. They show progressively thinner films on the same chemically patterned surface and demonstrate that there is a transition from the thicker films draining along the pattern to the thinner films not producing any appreciable pattern at all. Although there may not appear to be any replication of the chemical patterning, the authors note that the dominant length scales of the structures formed have been influenced by the pattern. [Sehgal et al., 2002] also show results for long scale evolution of films that de-wet and form droplets. The size, shape and orientation of drops are reported for a variety of pattern widths. The droplet configuration shifts from pairs of droplets per stripe, to disorganized single droplets to highly order droplets. If the width of the stripes gets to small, the droplets will bridge from one stripe to another and coalesce to form heterogenous drop structures. The study of chemical heterogeneity both numerically and experimentally has shown many interesting results for film evolution. [Sehgal et al., 2002] is used to help validate the numerical results and contrast them to the existing literature.

2.5 Perfect Dielectric Films

The dynamics of thin films can also be influenced by the application of an electric field and the works on thin films under the influence of electrostatic forces will be discussed in the following section.

2.5.1 Experimental Studies

In the early studies of thin films pressure based drainage, which is dominated by intermolecular forces, was the primary focus. The idea of using the forces created by the application of an electric field on a thin film was first presented by [Schaffer et al., 2000]. The use of electric fields to influence thin film dynamics has since become very popular due to its versatility.

In the work of [Schaffer et al., 2000] the influence of the application of an electric field on dynamics of a thin polymer film was studied experimentally. In the study, a thin polymer films was placed between two electrodes and a variety of patterns were produced. The experiments involved the application of uniform potentials on the two electrodes, where a variance in the electric field was achieved by a physical patterning on the upper surface.

The pattern on the upper surface changes the distance between the film and electrode and thus alters the electric field. The application of an electric field of sufficient strength resulted in the formation of a well organized series of circular cylindrical columns. After the initial column formation, coalescence may occur resulting in more complicated structures. The patterns produced are a function of the physical properties of the polymer, applied field, electrode patterning and time of evolution. This method of patterning called electrostatic lithography (EHD) [Schaffer et al., 2000] can create structures with length scales smaller then 100 nm, which is a length that typically limits such manufacturing methods as photo lithography. Two main experimental arrangements are used, one with a linear grooved pattern of the upper

electrode and a smooth upper electrode. The wavelength of the fastest growing mode is reported as:

$$\lambda_m = 2\pi\sqrt{\frac{2\gamma}{\frac{\partial P_{el}}{\partial h}}} \tag{2.5a}$$

Where λ_m is the fastest growing wavelength, γ is the interfacial tension, P_{el} is the electrostatic pressure and h is the film thickness. Schaffer *et al* report the electrostatic pressure as a function of the electric field strength and permittivity of the polymer.

$$P_{el} = -f(\epsilon)E_p^2 \tag{2.6a}$$

Where ϵ is the permittivity of the polymer film, E_p is the electric field in the polymer at the fluid interface. The exact functional dependance of P_{el} on ϵ is not known. The results of equation (2.5a) show good agreement with the experiments conducted.

In the experiments of [Schaffer et al., 2000], it was demonstrated experimentally that precise periodic patterns could be produced using EHD. When uniform electrodes were used, changing the electric field varied the resulting column size and packing in the film structure. When a periodic slot and groove pattern was applied to the upper electrode it resulted in a similar pattern being formed in the underlying film.

In the work of [Schaffer et al., 2001] the dominant wave length in structure formation on thin films under the influence of applied electric fields was studied. Here

the dominant instability is first established as:

$$\lambda_m = 2\pi\sqrt{\frac{U\gamma}{\epsilon_0\epsilon_p(\epsilon_p-1)^2}}E_p^{-3/2} \tag{2.7a}$$

Where the electric field in the polymer is written as:

$$E_p = \frac{U}{\epsilon_p d - (\epsilon_p - 1)h} \tag{2.8a}$$

Where U is the applied voltage. The experimental data is generalized by using the scaling variables

$$\lambda_0 = \frac{\epsilon_0\epsilon_p(\epsilon_p-1)^2U^2}{\gamma} \tag{2.9a}$$

$$E_0 = \frac{U}{\lambda_0} \tag{2.9b}$$

$$\frac{\lambda}{\lambda_0} = 2\pi\left(\frac{E_p}{E_0}\right)^{-3/2} \tag{2.9c}$$

Equation (2.9c) shows very good agreement with the experimental results. This relation allows the comparison of different electric field strengths and other parameters using a non-dimensional scale.

[Lin et al., 2001] consider the drainage of a thin film with an active fluid above it sandwiched between two electrodes and subjected to an applied electric field. The study demonstrated both experimentally and theoretically that length scales of a film interacting with a second viscous liquid are smaller then those for a film interacting with an inert second fluid. The theoretically derived wave length of the fastest growing

disturbance is given as:

$$\lambda_{max} = 2\pi\sqrt{\frac{\gamma_{12}U(\epsilon_1\epsilon_2)^{1/2}}{\epsilon_0(\epsilon_2-\epsilon_1)^2}}(E_1E_2)^{-3/4} \tag{2.10}$$

where γ_{12} is the interfacial tension between the fluids, U is the applied potential, ϵ_i is the permittivity in fluid i, ϵ_0 is the permittivity of free space and E_i is the electric field in fluid i. The electric field in the two fluids is given by equation (2.11), where $i, j = 1, 2$ and $i \neq j$.

$$E_i = \frac{\epsilon_j U}{\epsilon_1\Delta h_2 + \epsilon_2\Delta h_1} \tag{2.11}$$

and the characteristic response time is given as:

$$\tau_{max} = \frac{3C(\eta)\gamma_{12}U^2\epsilon_1\epsilon_2}{(-h_1h_2)^{3/2}\epsilon_0^2(\epsilon_2-\epsilon_1)^4(E_1E_2)^3} \tag{2.12}$$

The experiments of [Lin et al., 2001] demonstrate that the time required for the evolution of structures in the thin film can be significantly reduced by using a second fluid in place of air. The length scales of structures and there periodicity can also be modified by using a non-inert second fluid. They suggest that varying interfacial tension is the best way to achieve desired film patterning properties. They theorize that interfacial tension is widely variable and does not face the physical limitations that permittivity and applied voltage do. Linear theory was applied to predict the fastest growing length scale reasonable for two of the reported cases. The theoretic results are $\lambda_{max} = 13.75\ \mu m$ and $\lambda_{max} = 12.94\ \mu m$, as compared to the experimental

results $\lambda_{max} = 12.7\ \mu m$ and $\lambda_{max} = 7.6\ \mu m$. The main discrepancy comes in the prediction of characteristic length scale, the theoretical results are off by an order of magnitude. The linear theory predicts that no change in time should occur between a film with a second fluid other then air and a fluid with air, while experimentally the two fluid system developed structures 50 times faster. The primary conclusion of this work is that the time required for film dynamics can be significantly reduced through the use of an active second fluid above the liquid film.

After the detailed numerical study [Verma et al., 2005], [Voicu et al., 2006] under took a series of experiments to test the fabrication strategies suggested by the numerical simulation. The late stage morphology of the film is determined by the so called fill factor of the film (f), is defined as the volume fraction ($\varphi = h_0/d$). For small volume fractions the film takes on a periodic structure of columns which are spaced at roughly the fastest growing wave length of the film. For higher volume fractions ($\varphi \sim 0.5$) the columns coalesce into larger structures that make a morphology difficult to predict. When the film occupies less than half the space between the electrodes an array of columns is formed, but if the film starts with ($\varphi > 0.5$) then a system of holes is formed after the fluid wets the upper electrode. The influence of heterogeneous electrode patterns were also considered. The first was a single point defect on the surface of the upper electrode. The point defect created a single column which was then surrounded by a circle of columns nucleating outwards. In some cases the central column disappeared but in others it remained through out the interface evolution. The second situation experimentally produced was that of a step change

of field between two adjacent domains. In this case the patterns formed along the discontinuity initially and then spread through out the domain. An increased degree of order is observed along the step boundary. The final configuration studied was that of a serious of linear grates (lines of alternating potential). The experimental results do not agree with the numerical predictions of [Verma et al., 2005]. In the experiments columns were formed with highly ordered spacing along the grates as opposed to a uniform reproduction of the pattern as predicted by [Verma et al., 2005]. The experimental works of [Voicu et al., 2006] are used to validate the numerical results presented.

2.5.2 Theoretic and Numerical Studies

Theoretical studies of thin films under the influence of electric fields are typically differentiated based on the assumptions used in modeling charge dynamics. In a perfect dielectric formulation, no free charge carriers are considered. In a leaky dielectric formulation, free charge carriers and their motion along the film interface are modeled while the bulk of the fluid is still considered electro-neutral. The first theoretic work proposed for a leaky-dielectric was developed by [Pease and Russel, 2002]. The model was proposed to address the discrepancies in the fastest growing wave length and characteristic time scale reported by such authors as [Lin et al., 2001]. Detailed parameter studies for growth exponents and other values were performed to determine there influence on a leaky-dielectric film and the patterns it would produce. The wave length and time scales that were found using linear stability analysis were

closer to experimental results then perfect dielectric results. The differences between the theoretical results and experiments is credited to the inherent non-linearity in the system.

The first numerical modeling of $2D$ thin film evolution for leaky dielectrics was performed by [Craster and Matar, 2005]. They start by developing interfacial charge and film evolution equations that are then solved numerically in $2D$ using spectral and finite difference methods. A parameter study of the conductivities, permittivities, film thickness ratio and others were performed. The general conclusions from these results are limited to some general structures that can be expected and the times taken for them to evolve.

One of the most complete numerical studies of thin film evolution was conducted by [Merkt et al., 2005]. A general film evolution equation for a $3D$ film is derived and solved numerically. They note that a $3D$ formulation has the addition of a mean flow term F that only influences the time for film evolution and not the structures produced so may be neglected if a study of the structures is being undertaken. The analysis is divided into short and long time domains. The initial short time interactions are the film interaction with the initial perturbation and are much quicker then the development of the patterns that are typically the focus of this type of study.

The numerical modeling of a perfect dielectric film under the influence of an applied electric field was first carried out in $2D$ by [Wu and Chou, 2003]. In this

work the use of Lithographically self-assembly (LISA) and Lithographically induced self-construction (LISC) are discussed. LISA is a process where polymer films form periodic sets of column under an applied electric field and LISC is a process where polymer films form larger entities called "mesas" under an applied electric field. The study focused on the transition between these two types of structure formation for an electrically perturbed thin polymer film. It was found that the size of the electrode L and the ratio of electric and interfacial tension forces γ/U^2 (where γ is the interfacial tension and U is the applied voltage). Three distinct regimes of structure creation in a perfect dielectric film are shown. The first is distinct pillars that remain separate; the second is distinct pillars that coalesce; and final regime is the formation of mesas. A set of two linear equations could be found that related the size of the fastest growing wavelength as predicted by linear theory to the electrode size. The validity of these questions shows good agreement with the experimental results, but problems with linear theory in predicting film dynamics have been reported by a number of authors

The full $3D$ modeling of a perfect dielectric film was developed simultaneously by [Wu and Russel, 2005] and [Verma et al., 2005]. In the work of [Wu and Russel, 2005] pseudo spectral methods are used to study the influence of electrode patterning on the evolution of the film. The electrode patterning takes the form of a topographic pattern on the upper electrode. This physical patterning creates a difference in electric field for the film, which could also be achieved by the imposition of a variable applied potential. [Wu and Russel, 2005] conclude that electrode patterning can increase or

decrease the regularity and spacing of the columns that form. Numerical results are compared to experimental results for various sizes and shapes of electrode patterns. If initial film thickness are greater then $h/d > 0.6$ then the patterns formed tend to form less structured hexagonal patterns. The pattern growth starts at the edges of the patterns where the gradients in electric field are most pronounced and then propagate inward.

The numerical studies of [Wu and Russel, 2005] were continued in a second paper [Wu et al., 2005]. In this work they present both weakly non-linear and fully non-linear $1D$ and $2D$ simulations of film evolution. The authors recommend the use of a series of small patterns on an electrode if highly ordered cylinders are desired. When a large pattern is used a less order hexagonal structure occurs at locations far from the boundaries. Thus by creating a high number of boundaries, through the use of a series of small elements in a pattern, a highly ordered structure can be produced over the entire domain.

In the work of [Verma et al., 2005] a range of geometries and there influence on the film pattern formation were studied. The geometries considered were: uniform, striped, checkered and circles. [Verma et al., 2005] uses a volume fraction ($\varphi = V_{film}/V_{Total} = h_0/d$) to study the different patterns that are formed and how the thickness of the fluid influences the results. For small volume fractions ($\varphi < 0.25$) quasi-stable hexagonally packed columns of cylindrical columns are found. As the volume fraction is increased the ordering of columns and there cross section becomes

more difficult to define with a variety of column cross sections and patterns formed during coalescence of columns. For a large volume fraction ($\varphi \geq 0.75$) liquid columns quickly coalesce and a phase inversion occurs, in that air holes are dispersed within the fluid instead of vice versa.

The influence of electrode patterning was examined and the best patterning occurred when the pattern periodicity (L_p) slightly exceed the spinodal length scale evaluated based on the maximum e-field strength $\lambda_{m-d_{min}}$. A second bound was found for the pattern length and it was based on the spinodal length for mean separation λ_m. The two conditions give a recommended interval for linear patterning which can be seems as the inequality in equation (2.13):

$$\lambda_m \geq L_p \geq \lambda_{m-d_{min}}. \tag{2.13}$$

[Verma et al., 2005] also noted that for the case when the electrode patterning is greater then the mean spinodal length ($Lp > \lambda_m$) secondary structures could occur if the patterning was not sufficiently deep. All variations in electric field are produced by changing the electrode spacing locally. If the amplitude (a_h) ratio of the pattern on the upper electrode relative to the average thickness (d_{avg}) between the two surfaces $A_h = a_h/d_{avg}$ is large enough then the secondary structures can be suppressed. If the amplitude ratio is $A_h > 0.25$ then secondary structures will not result. The numerical results of [Verma et al., 2005] were used to help validate the code developed.

2.6 Summary

The study of thin film drainage to date has produced a variety of interesting experimental and theoretical results. The studies of pressure and electrostatically based drainage have been conducted separately with a wide range of motives and goals. The influence of electrical and chemical heterogeneity have been investigated independently but little work has been done on comparing these two methods of drainage. When studying pressure based drainage there has been little consideration of pressure based drainage with an upper bounding surface. This study will discuss the influence of an upper inert bounding surface on the drainage induced in a thin film.

Studies of chemically and heterogeneous surface have focused on the ability to manipulate film drainage and reproduce the underlying pattern on the surface. In the case of chemically patterned surfaces, this typically means the amount of area de-wet as the film drains. For electrostatically patterned surfaces, patterning tends to focus on wetting of the upper bounding surface and typically uses thick films (with a ratio of electrode spacing to initial film thickness of less than 2).

The objective of this study is to study the drainage of thin films on chemically or electrostatically patterned surfaces for intermediate thickness films. This study will examine how fabrication methods such as EHD can be expanded by looking at structures that form when non-ideal pattern replication occurs. The use of different film thickness and patterning dimensions allows a range of different potential drainage morphologies. Using these conventional techniques in new ways could help increase the range of potential operation for a single EHD configuration. The time and length

scales that occur in pressure and electrostatically dominated drainage will also be discussed to aid in the understanding of drainage behaviour.

2.7 Contributions

The following will briefly outline some of the major contributions to thin film theory. An early significant work on thin films was that of [Ruckenstein and Jain, 1974] who first formulated the Lifshitz van-der Waals (LVDW) interactions experienced in thin films. The 'long-wave' models that allow the reduction of the Navier-Stokes equations were first applied by [Atherton and Homsy, 1976] using the mathematical construct of [Benney, 1966]. The modeling of the contact line singularity that occurs at the solid/liquid/gas interface was greatly simplified by the work of [Mitlin, 1993]. The 'absorbed layer' model he proposed accurately captures film dynamics while removing the complication of modeling a moving contact line.

The first $2D$ numerical studies of thin film evolution were carried out by [Williams and Davis, 1982]. This was followed by one of the first $3D$ numerical studies of film drainage by [Sharma and Jameel, 1993]. The work of [Khanna and Sharma, 1997] helped clarify the dominant wave lengths in pressure based drainage. The study of chemical heterogeneity was well addressed by a series of papers on the topic produced by [Kargupta et al., 2000, Kargupta and Sharma, 2001, Kargupta and Sharma, 2002]. In these studies an array of heterogeneities were discussed including stripes, and checkered patterns. The study of patterning due to electric field variation was well summarized by the work of [Verma et al., 2005]. A variety of homogeneous

and spatially varying electric fields are presented in this study. The work of [David G. Crawford, 2008] presents a comparison of the time taken for electrostatic and pressure based drainage on homogeneous substrates.

One of the first experimental studies on thin film drainage was performed by [Zhao et al., 1993]. This experimental work on thin polymer films was used to validate much of the early numerical work in this field. The rate and quantity of structure formation in polymer melts was later studied by [Xie et al., 1998]. The experimental study of chemical patterning and thin film dynamics were studied by [Rockford et al., 1999]. The influence of chemical patterning was examined and pattern replication due to striped patterning was observed. The study of chemical patterning was extended by [Sehgal et al., 2002]. In this work the varying influence of different width and pitch stripes was studied for polymer films, demonstrating that a transition from good pattern replication to random de-wetting occurs as pattern size is diminished. The first experimental studies of electrical patterning and thin films were performed by [Schaffer et al., 2000]. This work demonstrated that electric fields could be used to reproduce patterns on an upper electrode by inducing film drainage. The experimental study of electrically actuated film drainage was then continued in [Schaffer et al., 2001] and [Lin et al., 2001]. The work of [Voicu et al., 2006] demonstrates a series of experimental validations of cases studied by various authors numerically. The results are an excellent guide for model validation.

The contributions listed above are very succinct and all efforts were made to avoid excluding any major contributions.

CHAPTER 3

THEORY AND NUMERICAL FORMULATION

This chapter will be split into two parts, the first half will present the mathematical model and the second half will present the numerical method of thin films. The chapter will begin by defining the governing equations and boundary conditions for the thin film system. The 'long-wave' asymptotic analysis will then be presented and the film evolution equation will be derived. A discussion of the forces that affect film drainage will then be presented. A description of the non-dimensionalization leading to the scaled governing equations and film evolution equation follows. The chapter concludes by presenting the numerical methods employed.

3.1 Mathematical Model

3.1.1 Governing Equations

When a thin film is perturbed by an infinitesimal disturbance, the perturbations may grow, remain the same or be attenuated. If the film is thicker than a critical thickness, the perturbations will grow in a periodic manner creating waves on the film

surface [Williams and Davis, 1982, Ruckenstein and Jain, 1974]. The perturbations grow with a characteristic wave length (λ). The wave lengths of the disturbance are much larger than the mean film thickness. This difference in length scale between the film thickness and the waves that form on the film interface allow the simplification of the governing equations. A 'long-wave' asymptotic analysis can be used to simplify the governing equations [Oron et al., 1997].

The thin film system studied is shown schematically in Figure 3.1. It depicts a liquid film and bounding fluid on top, sandwiched between two electrodes. As shown in Figure 3.1, d is the electrode spacing, $h(x, y, t)$ is the film thickness at spatial coordinates (x, y) and time (t), h_0 is the average initial film thickness, subscript i indicates the fluid phase under consideration with $i = 1$ for the film and $i = 2$ for the bounding fluid, ϵ_i indicates the permittivity of fluid $(i = 1, 2)$, μ_i is the viscosity of fluid $(i = 1, 2)$, λ is the wave length of disturbances on the film interface, ψ_{up} is an applied voltage at upper electrode $(z = d)$ and ψ_{low} is the applied voltage at the lower electrode $(z = 0)$. The figure shows a (x, z) plane view but is representative of the full $3D$ system and disturbances on the film surface would have the same dominant length scale (λ) in both the (x, y) directions.

The fluids are modeled using a continuum assumption and the motion is defined by the Navier-Stokes (NS) equations and a continuity relation.

$$\begin{aligned} \rho_i \left(\tfrac{\partial \vec{u_i}}{\partial t} + (\vec{u_i} \cdot \nabla)\vec{u_i}\right) &= -\nabla P_i + \nabla \cdot [\mu_i(\nabla \vec{u_i} + (\nabla \vec{u_i})^T)] + \vec{f_i} \\ \nabla \cdot (\rho_i \vec{u_i}) &= 0 \end{aligned} \tag{3.1}$$

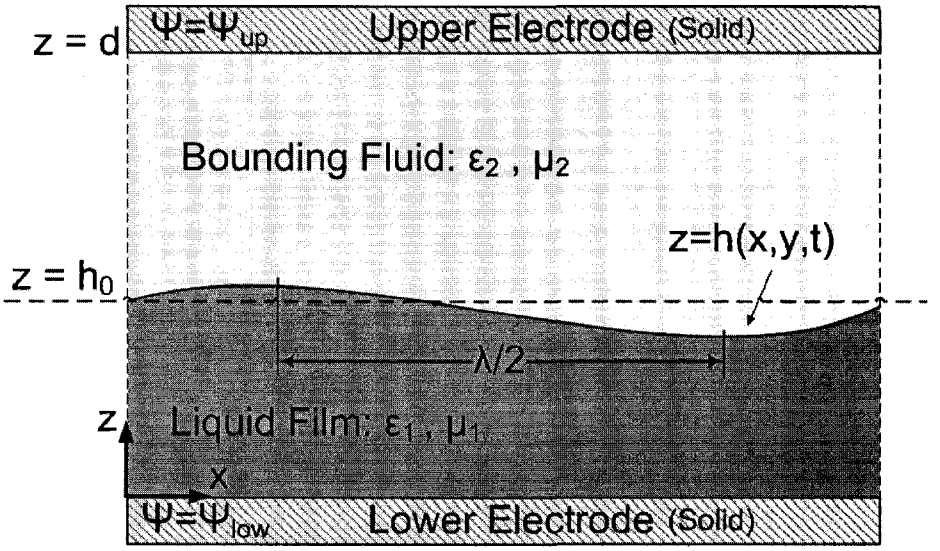

Figure 3.1: Schematic representation of the thin film system. The liquid film under consideration is supported by the lower electrode. The bounding fluid is modeled as an inert fluid (similar to air) with $\mu_2 \ll \mu_1$. For electrostatic force induced drainage, a potential difference of $\psi_{low} - \psi_{up}$ is applied between the two electrodes, with ψ_{up} typically set as ground. The initial height of the unperturbed film is h_0 and the vertical distance between the two electrodes is d.

$\vec{u_i}$ is the velocity vector ($\vec{u} = [u, v, w]$) in fluid ($i = 1, 2$), P_i is the pressure in fluid ($i = 1, 2$), ρ_i is the density in fluid ($i = 1, 2$), ∇ is the cartesian operator $\vec{\nabla} = (\partial/\partial x, \partial/\partial y, \partial/\partial z)$, $\vec{f_i} = -\nabla(\phi)$ represents the body forces, where ϕ_i is the conjoining/disjoining pressure. The conjoining/disjoining pressure is an excess energy per unit volume function that describes forces that exist on the film. The Navier-Stokes system shown in equations (3.1) is applied for both the film and bounding fluid ($i = 1, 2$).

The general formulation for thin film drainage is completed by the definition of boundary conditions. At the upper and lower electrodes, no penetration and no slip boundary conditions are applied.

$$\begin{aligned} \vec{u_1} &= 0 \quad \text{at} \quad z = 0 \\ \vec{u_2} &= 0 \quad \text{at} \quad z = d \end{aligned} \tag{3.2}$$

At the interface between the fluids, continuity of velocity and a stress balance exist. The two fluids are modeled as immiscible; so no fluid mixing or mass transfer occurs at their interface. This ensures that a sharp interface is maintained and that velocity is continuous across it.

$$\vec{u_1} = \vec{u_2} \quad \text{at} \quad z = h(x,y,t) \tag{3.3}$$

The velocity of the fluids at the interface is related to the film thickness by a kinematic condition [Williams and Davis, 1982]. The kinematic condition is obtained by taking the definition of the film thickness, $z = h(x, y, t)$, and taking the partial derivative with respect to time. The chain rule and velocity definitions can then be used to relate the film thickness to the interfacial velocity.

$$w = \frac{\partial h}{\partial t} + u\frac{\partial h}{\partial x} + v\frac{\partial h}{\partial y} \quad \text{at} \quad z = h(x,y,t) \tag{3.4}$$

where $u = \frac{dx}{dt}$ and $v = \frac{dy}{dt}$. The kinematic condition in equation (3.4) will be used in place of the continuity of velocity equation (3.3). At the interface, a stress balance between the two fluids is performed by taking the normal and tangential projections of the stresses at the fluid interface.

$$\vec{n} \cdot [\bar{\bar{\sigma}}_1 \cdot \vec{n} - \bar{\bar{\sigma}}_2 \cdot \vec{n}] = \kappa\gamma + \vec{f_e} \cdot \vec{n} \tag{3.5}$$

$$\vec{t^j} \cdot [\bar{\bar{\sigma}}_1 \cdot \vec{n} - \bar{\bar{\sigma}}_2 \cdot \vec{n}] = \vec{f}_e \cdot \vec{t^j} \tag{3.6}$$

where $\vec{t^j} = (t_x^{(j)}, t_y^{(j)}, t_z^{(j)})$ is the j^{th} unit tangent vector to the fluid interface where $(j = 1, 2)$, $\vec{n}$ is the normal unit vector to the fluid interface, which points from the film to the bounding fluid with components $\vec{n} = (n_x, n_y, n_z)$, κ is the mean interfacial curvature, γ is the interfacial tension, $\vec{f}_e$ is the external surface force vector and $\bar{\bar{\sigma}}_i$ is the stress tensor for the i^{th} fluid phase $(i = 1, 2)$. The stress tensor $(\bar{\bar{\sigma}}_i)$ is defined as:

$$\bar{\bar{\sigma}}_i = -\bar{\bar{I}} P_i + \mu_i \left(\nabla \vec{u_i} + \nabla \vec{u_i}^T \right) \tag{3.7}$$

The film surface can be described mathematically as a $3D$ surface having the form $G(x, y, z, t) = h(x, y, t) - z = 0$. Using differential geometry, the surface curvature, normal and tangential vectors can be defined. The surface curvature is represented by the two principal radii of curvature.

$$\kappa = \left(\frac{1}{R_1} + \frac{1}{R_2} \right) \tag{3.8}$$

where the principal radii of curvature can be defined in terms of the the film thickness and yields the expression [Atherton and Homsy, 1976]

$$\frac{1}{R_1} + \frac{1}{R_2} = \frac{\frac{\partial^2 h}{\partial x^2}\left(1 + \left(\frac{\partial h}{\partial y}\right)^2\right) + \frac{\partial^2 h}{\partial y^2}\left(1 + \left(\frac{\partial h}{\partial x}\right)^2\right) - 2\frac{\partial^2 h}{\partial x \partial y}\frac{\partial h}{\partial x}\frac{\partial h}{\partial y}}{(1 + \left(\frac{\partial h}{\partial x}\right)^2 + \left(\frac{\partial h}{\partial y}\right)^2)^{3/2}} \tag{3.9}$$

The normal and tangential unit vectors can then be defined using differential geometry

[Atherton and Homsy, 1976, Williams and Davis, 1982].

$$n_x = \frac{1}{C_n}\left(\frac{\partial h}{\partial x}\right) \quad n_y = \frac{1}{C_n}\left(\frac{\partial h}{\partial y}\right) \quad n_z = \frac{-1}{C_n} \tag{3.10}$$

The scaling for the normal unit vectors is $C_n = \sqrt{1 + (\partial h/\partial x)^2 + (\partial h/\partial y)^2}$.

$$t_x^{(1)} = \frac{1}{C_{t1}}(-\frac{\partial h}{\partial y}) \quad t_y^{(1)} = \frac{1}{C_{t1}}(\frac{\partial h}{\partial x}) \quad t_z^{(1)} = 0 \tag{3.11}$$

$$t_x^{(2)} = \frac{1}{C_{t2}}(\frac{\partial h}{\partial x}) \quad t_y^{(2)} = \frac{1}{C_{t2}}(\frac{\partial h}{\partial y}) \quad t_z^{(2)} = \frac{1}{C_{t2}}((\frac{\partial h}{\partial y})^2 + (\frac{\partial h}{\partial x})^2) \tag{3.12}$$

where the scaling for unit tangent vector one ($j = 1$), is $C_{t1} = \sqrt{(\partial h/\partial x)^2 + (\partial h/\partial y)^2}$ and the scaling for tangent vector two ($j = 2$) is $C_{t2} = \sqrt{(\partial h/\partial x)^2 + (\partial h/\partial y)^2 + ((\partial h/\partial x)^2 + (\partial h/\partial y)^2)^2}$. The motion of a thin film is described by the Navier-Stokes system shown in equations (3.1 - 3.6).

3.1.2 Film Evolution Equation

The NS equation system presented in the previous section is difficult to solve since the interface between the fluids is a free boundary. Fortunately, the problem scaling and physics allow the system to be reduced to a single evolution equation for the film thickness. The 'long wave' or 'small slope' scaling argument uses the fact that dominant wave length of disturbances, λ, which dictates the length scale of the problem are much larger than the film thickness, h [Shankar and Sharma, 2004, Williams and Davis, 1982, Oron et al., 1997, Khanna and Sharma, 1997]. The length of the waves

(λ) that occur on the film surface are dictated by the physical parameters of the system. For the cases studied numerically in this work, the minimum ratio of dominant wave length as predicted by linear theory was $\lambda = 630\ nm$ for a film of thickness $h_0 = 20\ nm$ which has a ratio of $\lambda/h_0 = 31.5$. Thus the ratio of the dominant film structure to the initial film thickness is at least $\lambda/h_0 \geq 31.5$ for all cases considered. For simplicity, a scaling factor 'k' will be defined to indicate the difference in lengths and aid in the equation derivation.

$$k = \frac{h_0}{\lambda} << 1 \tag{3.13}$$

The lengths are non-dimensionalized by using the mean film thickness h_0 for z. The (x, y) dimensions are scaled by the dominant length of the fastest growing disturbance on the film. The fastest growing disturbance on the film is represented by the wave length (λ), which is uniform in both the x and y directions. The non-dimensionalized spatial dimensions and the spatial derivatives are explicitly given by (the uppercase variables represent the non-dimensional quantities).

$$\begin{gathered} x = \lambda X \qquad y = \lambda Y \qquad z = h_0 Z \\ \frac{\partial}{\partial x} = \frac{1}{\lambda}\frac{\partial}{\partial X} \quad \frac{\partial}{\partial y} = \frac{1}{\lambda}\frac{\partial}{\partial Y} \quad \frac{\partial}{\partial z} = \frac{1}{h_0}\frac{\partial}{\partial Z} \end{gathered} \tag{3.14}$$

Equations (3.14) are simplified using equation (3.13) and can be used to determine the other problem parameters. If the fluid velocity in the lateral dimensions (x, y) has values $u_0, v_0 = O(1)$ then the non-dimensional velocities in these directions can

be written as:

$$U = \frac{u}{u_0} \qquad V = \frac{v}{u_0} \tag{3.15}$$

where u_0 is a characteristic velocity of the film flow. The continuity relation, equation (3.1), is reduced using equations (3.14) and (3.15).

$$\frac{u_0 k}{h_0}\frac{\partial U}{\partial X} + \frac{u_0 k}{h_0}\frac{\partial V}{\partial Y} + \frac{1}{h_0}\frac{\partial w}{\partial Z} = 0 \tag{3.16}$$

which suggests a scaling of the fluid velocity in z direction as

$$W = \frac{w}{u_0 k} \tag{3.17}$$

The time is re-scaled to reflect the long length scales considered, defining a new slow time (T) based on the characteristic velocity (u_0) and long length scale (λ)

$$T = \frac{k u_0}{h_0} t \tag{3.18}$$

Following the work of [Oron et al., 1997], the flow within the film will be locally parallel so that $p_x \sim \mu u_{zz}$ and $p_y \sim \mu v_{zz}$. This suggests scaling for the pressure (P) and the conjoining/disjoining pressure (Φ) as:

$$(P, \Phi) = \frac{k h_0}{\mu u_0}(p, \phi) \tag{3.19}$$

where $\mu = \mu_1$ is the viscosity of the fluid film and (P, Φ) are non-dimensional pres-

sure and conjoining/disjoining pressure. Re-writing the NS system with the scalings introduced by equations (3.14 - 3.19) and assuming that the fluids are Newtonian, incompressible, and iso-thermal with constant properties gives:

$$kRe\,(U_T + UU_X + VU_Y + WU_Z) = -(P+\Phi)_X + k^2(U_{XX} + U_{YY}) + U_{ZZ} \quad (3.20a)$$

$$kRe\,(V_T + UV_X + VV_Y + WV_Z) = -(P+\Phi)_Y + k^2(V_{XX} + V_{YY}) + V_{ZZ} \quad (3.20b)$$

$$\begin{aligned} &k^3 Re\,(W_T + UW_X + VW_Y + WW_Z) = \\ &-(P+\Phi)_Z + k^2[k^2(W_{XX} + W_{YY}) + W_{ZZ}] \end{aligned} \quad (3.20c)$$

$$0 = \frac{\partial U}{\partial X} + \frac{\partial V}{\partial Y} + \frac{\partial W}{\partial Z} \quad (3.20d)$$

where the Reynolds number is defined as $Re = \rho u_0 h_0/\mu$. Equations (3.20a-3.20c) apply for both fluids. The subscripts in the above equations represent derivatives with respect to the non-dimensional variable, e.g. $\partial Q/\partial X \equiv Q_X$. The boundary conditions at the upper and lower surface are independent of the scaling, but will be re-written for completeness.

$$\begin{aligned} &\vec{U}_1 = 0 \qquad \text{at} \quad \mathrm{Z} = 0 \\ &\vec{U}_2 = 0 \qquad \text{At} \quad \mathrm{Z} = \mathrm{d/h_0} \end{aligned} \quad (3.21)$$

At the fluid interface, the kinematic condition becomes:

$$W = H_T + UH_X + VH_Y \quad \text{at} \quad \mathrm{Z} = \mathrm{H(X,Y,T)} \quad (3.22)$$

The normal and tangential vectors are also scaled and take the forms:

$$\vec{n} = \frac{1}{\sqrt{1+k^2(H_X^2+H_Y^2)}}\left(kH_X,\ \ kH_Y,\ \ -1 \right) \tag{3.23}$$

$$\vec{t^1} = \frac{1}{\sqrt{H_X^2+H_Y^2}}\left(-H_Y,\ \ H_X,\ \ 0 \right) \tag{3.24}$$

$$\vec{t^2} = \frac{1}{\sqrt{H_X^2+H_Y^2+k^2(H_X^2+H_Y^2)^2}}\left(H_X,\ \ H_Y,\ \ k(H_X^2+H_Y^2) \right) \tag{3.25}$$

The scaled stress boundary conditions are written as:

$$\begin{aligned}
&-P + P_{ext} - k(kH_Y f_X + kH_Y f_Y - f_Z) \\
&-\gamma k^3 \frac{\left(H_{XX}(1+k^2H_Y^2)+H_{YY}(1+k^2H_X^2)-2k^2H_{XY}H_XH_Y\right)}{(1+k^2(H_x^2+H_Y^2))^{3/2}} \\
&+\{\ k^2H_X\left[2k^2U_XH_X + k^2H_Y(U_Y+V_X) - (k^2W_X+U_Z)\right] \\
&+k^2H_Y\left[k^2H_X(U_Y+V_X) + 2k^2H_YV_Y - (k^2W_Y+V_Z)\right] \\
&-k[kH_X(k^2W_X+U_Z) + kH_Y(k^2W_Y+V_Z) - 2kW_Z]\ \} = 0
\end{aligned} \tag{3.26}$$

$$\begin{aligned}
&-H_Y\left[2k^2U_XH_X + k^2H_Y(U_Y+V_X) - (k^2W_X+U_Z)\right] \\
&+H_X\left[k^2H_X(U_Y+V_X) + 2k^2H_YV_Y - (k^2W_Y+V_Z)\right] = 0
\end{aligned} \tag{3.27}$$

$$\begin{aligned}
&H_X\left[2k^2U_XH_X + k^2H_Y(U_Y+V_X) - (k^2W_X+U_Z)\right] \\
&+H_Y\left[k^2H_X(U_Y+V_X) + 2k^2H_YV_Y - (k^2W_Y+V_Z)\right] \\
&+k(H_X^2+H_Y^2)[kH_X(k^2W_X+U_Z) + kH_Y(k^2W_Y+V_Z) - 2kW_Z] = 0
\end{aligned} \tag{3.28}$$

where the interfacial tension must be re-scaled to ensure that its influence is not lost $\bar{\gamma} = k^3\gamma = O(1)$. The scaling of the interfacial tension ensures that the time scale for

capillary based (interfacial tension driven) instabilities will be on the same time scale as all other phenomena. The general film formulation, is defined by equations (3.20a - 3.20d) and the boundary conditions in equations (3.21 - 3.22 , 3.26 - 3.28).

The focus of this study is confined films where a viscosity ratio of the film to bounding fluid is large ($\mu_2/\mu_1 << 1$). Therefore, in the fluid films studied, the bounding fluid acts like an inert gas and eliminates the requirement for solving the evolution equations for both fluids. Since the fluid film is thin ($h_0 < 100\ nm$) the inertial effects will be dominated by the fluid viscosity. This means that the Reynolds number will be negligible $Re << 1$. These simplifications, along with consideration of the leading order terms in equations (3.20a - 3.28), yield:

$$-(P_X + \Phi_X) + U_{ZZ} = 0 \tag{3.29a}$$

$$-(P_Y + \Phi_Y) + V_{ZZ} = 0 \tag{3.29b}$$

$$P_Z + \Phi_Z = 0 \tag{3.29c}$$

$$U_X + V_Y + W_Z = 0 \tag{3.29d}$$

The fluid films studied are not subject to thermal gradients or other external disturbances and thus their properties are assumed constant in space and time. Equations (3.29) form the basis for the derivation of the interface motion equation. The boundary conditions used are:

$$\begin{aligned} \vec{U} = 0 \quad &\text{at} \quad z = 0 \\ \bar{P} - P_{ext} = (H_{XX} + H_{YY}) \quad &\text{at} \quad z = h(x,y,t) \\ U_Z = V_Z = 0 \quad &\text{at} \quad z = h(x,y,t) \end{aligned} \tag{3.30}$$

where P_{ext} is the external reference pressure (set to zero). The kinematic condition at the fluid interface $z = h(x, y, t)$ is also used to relate the temporal changes of the interface to the fluid velocity:

$$H_T + UH_X + VH_Y = W \quad \text{at} \quad Z = H(X,Y,T) \tag{3.31}$$

The interface motion equation is derived using equations (3.29) and the kinematic condition (3.31) with the boundary conditions in equations (3.30) . As a simplification of the analysis, the body force and pressure terms are combined to form a modified pressure:

$$\bar{P} = P + \Phi \tag{3.32}$$

Equation (3.29c) demonstrates that the modified pressure $\bar{P}$ is independent of z so equations (3.29a) and (3.29b) can be integrated to give:

$$U = \bar{P}_X Z(\frac{1}{2}Z - H) \tag{3.33a}$$

$$V = \bar{P}_Y Z(\frac{1}{2}Z - H) \tag{3.33b}$$

Equations (3.33) are then substituted into the continuity equation. This yields an

equation for the z velocity component, W, which is solved:

$$U_X + V_Y + W_Z = 0 \tag{3.34a}$$

$$W_Z = -\frac{1}{2}Z^2(\bar{P_{XX}} + \bar{P_{YY}}) + Z[(\bar{P_X}H)_X + (\bar{P_Y}H)_Y] \tag{3.34b}$$

$$W = \frac{1}{2}Z^2[-\frac{1}{3}Z(\bar{P_{XX}} + \bar{P_{YY}}) + [(\bar{P_X}H)_X + (\bar{P_Y}H)_Y]] \tag{3.34c}$$

The last fluid evolution equation can be found by substituting the relations for the fluid velocity equations (3.33 - 3.34) and pressure equations (3.30 and 3.32) into the kinematic condition equation (3.31). The final evolution equation for the film can be written as:

$$\frac{\partial H}{\partial T} + \frac{\partial}{\partial X}\left[H^3\frac{\partial \Psi}{\partial X}\right] + \frac{\partial}{\partial Y}\left[H^3\frac{\partial \Psi}{\partial Y}\right] = 0 \tag{3.35}$$

$$\Psi = \frac{\partial^2 H}{\partial X^2} + \frac{\partial^2 H}{\partial Y^2} - \Phi \tag{3.36}$$

The function Φ is an energy density function called the conjoining/disjoining pressure. It represents the overall body forces acting on the film, which result from intermolecular and electrostatic interactions.

3.1.3 Body Forces

In the thin film drainage system considered, the Navier-Stokes equations take on a pseudo stationary form where the temporal dependence occurs due to time varying

body forces. The film experiences body forces as a result of intermolecular and electrostatic interactions.

The intermolecular forces considered in the present work consist of long range Lifshitz-van der Waals (LVDW) and a short range repulsion similar to Born repulsion. The forces that act on an element of fluid in a thin film differ from those in a bulk fluid, since the length scale of intermolecular interactions are comparable to the film thickness [Ruckenstein and Jain, 1974]. If a single fluid molecule is considered, it has intermolecular interactions with not only other fluid molecules but also the surrounding gas and solid surface upon which the film rests [Ruckenstein and Jain, 1974]. The energy per unit volume or conjoining/disjoining pressure in the film due to the LVDW forces can be written as [Ruckenstein and Jain, 1974, Verma et al., 2006]:

$$\phi_{LVDW_L} = \frac{A_L}{6\pi h^3} \tag{3.37}$$

$$\phi_{LVDW_U} = \frac{A_U}{6\pi (d-h)^3} \tag{3.38}$$

where A_L, A_U are the effective Hamaker constants for interactions between the free surface of the film and the upper and lower solid surfaces through the fluid film with units of Joules (J). The calculation of the effective Hamaker constant is typically dominated by the fluid solid interaction. Thus, the effective Hamaker constant can be written as [Masliyah and Bhattacharjee, 2006]:

$$A = (A_{fluid} A_{solid})^{1/2}$$

In pressure based drainage, the LVDW forces are responsible for the film drainage and may lead to the formation of dry spots (also called holes) where the liquid film has de-wet the lower solid surface. Equation (3.37) increases without bound as the film dries out at the lower surface ($h = 0$). The formation of a hole in the film leads to a singularity in the form of a contact line between the film, solid and surrounding medium. The contact line is modeled by using an 'adsorbed layer' asymptotic method as suggested by [Mitlin, 1993]. In an adsorbed layer model a very thin layer of fluid is maintained on the solid surface by the inclusion of a short range repulsive force. The inclusion of a constant film layer on the solid surface removes the contact line singularity by preventing complete film drainage. In this work, an 'absorbed layer' of thickness $l_0 = 1\ nm$ is maintained on both solid surfaces. A 1 nm thick 'absorbed layer' does not significantly influence the film drainage while ensuring the continuity assumption remains valid . A variety of different thicknesses for the 'absorbed layer' have been reported from $l_0 = 0.137 - 2.5\ nm$ [Khanna and Sharma, 1997,Sharma and Khanna, 1998], when these values were varied the final film configurations were not modified unless ultra thin films $h < 8\ nm$ were considered. The close range repulsive terms take the form [Mitlin, 1993]:

$$\phi_{BL} = -\frac{8BL}{h^9} \tag{3.39}$$

$$\phi_{BU} = \frac{8BU}{(d-h)^9} \tag{3.40}$$

The close range repulsive constants are found by setting the conjoining/disjoining

pressure equal to zero at the upper and lower surface.

$$\begin{aligned} BL &= \frac{\phi(z=l_0)l_0^9}{8} \\ BU &= \frac{\phi(z=d-l_0)l_0^9}{8} \end{aligned} \tag{3.41}$$

When a thin film is subjected to an applied electric field the Maxwell stress induced at the fluid interface can induce flow [Taylor and McEwan, 1965]. The thin film system considered in this study, is isolated from magnetic excitation, thus the electrostatic interactions are described by the equations for polarizable media [Landau and Lifshitz, 1960]:

$$\nabla \times \vec{E} = 0 \tag{3.42}$$

$$\nabla \cdot \vec{D} = \nabla \cdot \left(\epsilon_0 \vec{E} + \vec{P}\right) = \rho_f \tag{3.43}$$

where $\vec{E}$ is the electric field, $\vec{D}$ is the electrical displacement, $\vec{P}$ is the polarization, ρ_f is the free charge density and ϵ_0 is the permittivity of free space. The films of interest for this study are modeled as linear isotropic dielectrics. For a linear isotropic dielectric the polarization is [Landau and Lifshitz, 1960]:

$$\vec{P} = \epsilon_0 \left(\epsilon_r - 1\right) \vec{E} \tag{3.44}$$

where ϵ_r is the relative permittivity of the medium. Since the films are perfect dielectrics or perfect insulators, no free charge careers exist $\rho_f = 0$ and thus no current can be produced in the film. The electric field has a standard solution form using the electric potential (ψ):

$$\vec{E} = -\nabla\psi \tag{3.45}$$

Equation (3.43) is simplified using equations (3.44) and (3.45) in the absence of free charge carriers to yield:

$$\nabla^2 \psi_i = 0 \quad (\mathrm{i} = 1, 2) \tag{3.46}$$

where ψ_i is the potential in fluid ($i = 1, 2$). The boundary conditions for the electrostatics problem are defined as:

$$\begin{aligned} &\psi_1 = \psi_{low} && \text{at} \quad z = 0 \\ &\psi_1 = \psi_2 && \text{at} \quad z = h(x,y,t) \\ &\epsilon_1 \tfrac{\partial \psi_1}{\partial z} = \epsilon_2 \tfrac{\partial \psi_2}{\partial z} && \text{at} \quad z = h(x,y,t) \\ &\psi_2 = 0 && \text{at} \quad z = d \end{aligned} \tag{3.47}$$

When a thin film is disturbed by an electric field the instabilities that develop are 'long-wave' in nature and allow the same scaling that was used for the Navier-Stokes equations [Schaffer et al., 2000, Verma et al., 2005]. Electrostatic driven drainage for a thin film is caused by the Maxwell stress at the fluid interface. In the current formulation, the Maxwell stress is included in the body force (conjoining/disjoining pressure) term established previously in the Navier-Stokes derivation. When the 'long-wave' asymptotic analysis is applied for the electrostatic system given by equations (3.45)-(3.47) become:

$$\frac{\partial^2 \bar{\psi}_i}{\partial Z^2} = 0 \quad (\mathrm{i} = 1, 2) \tag{3.48}$$

$$\vec{E} = \left(0, 0, \frac{\partial \bar{\psi}_i}{\partial Z}\right) \quad (\mathrm{i} = 1, 2) \tag{3.49}$$

$$\begin{aligned} \psi_1 &= 1 && \text{at} \quad Z = 0 \\ \bar{\psi}_1 &= \bar{\psi}_2 && \text{at} \quad Z = H(X,Y,T) \\ \epsilon_1 \tfrac{\partial \bar{\psi}_1}{\partial z} &= \epsilon_2 \tfrac{\partial \bar{\psi}_2}{\partial Z} && \text{at} \quad Z = H(X,Y,T) \\ \bar{\psi}_2 &= 0 && \text{at} \quad Z = d/h_0 \end{aligned} \tag{3.50}$$

where $\bar{\psi}_i = \psi_i/\psi^*$ is the scaled potential, and $\psi^* = \psi_{low}$ is a scaling potential. The scaling electric field is taken as a ratio of the electric potential and initial film thickness $E^* = \psi_{low}/h_0$. The above system of equations can be solved analytically for a thin film trapped between two homogeneous electrodes. Integrating between the upper and lower surface yields the electric potential distributions in the bounding gas and liquid film, and suppressing the over bars for convenience:

$$\psi_1 = \psi_{low}\left[1 + \left(\frac{Z}{\epsilon_p D - (\epsilon_p - 1)H}\right)\right] \tag{3.51}$$

$$\psi_2 = \frac{\psi_{low}(Z - D)}{\epsilon_p D - (\epsilon_p - 1)H} \tag{3.52}$$

where $\epsilon_p = \epsilon_1/\epsilon_2$ is the ratio of relative permittivity. The Maxwell stress (σ_{kl}^M at the fluid interface for a dielectric medium with no magnetic effects can be written in cartesian coordinates as [Landau and Lifshitz, 1960]:

$$\bar{\bar{\sigma}}^M = \epsilon_0 \left(\vec{E}\vec{E} - 0.5\vec{E} \cdot \vec{E}\bar{\bar{\delta}}\right) \tag{3.53}$$

where $\bar{\bar{\sigma}}^M$ is the Maxwell stress tensor at the interface between the two fluids, and $\bar{\bar{\delta}}$ is the kronecker delta or identity tensor. When the 'long-wave' scaling is applied to equation (3.53), the tensor becomes diagonal with a magnitude of $-0.5\epsilon_0 E_i^2$ $(i = 1, 2)$. The conjoining/disjoining pressure can thus be derived by substituting the continuity of electrical displacement at the fluid interface and equations (3.51) and (3.52), into the normal projection of the Maxwell stress yielding [Verma et al., 2005]:

$$\phi_{ES} = -0.5\epsilon_0\epsilon_p(\epsilon_p - 1)E_p^2 \tag{3.54}$$

the electric field at the interface between the fluids E_p is:

$$E_p = \frac{\psi_{low}}{\epsilon_p d - (\epsilon_p - 1)h} \tag{3.55}$$

The total conjoining/disjoining pressure can thus be defined with LVDW forcing (equation 3.37), Born-like close range repulsion (equations 3.39 and 3.40) and electrostatic forcing (equation 3.54):

$$\phi = \phi_{LVDW} + \phi_{BL} + \phi_{BU} + \phi_{ES} \tag{3.56}$$

3.1.4 Scaling

Different scaling is performed depending on the purpose of the simulation. The problem scaling is derived from a linear stability formulation for the thin film equation. The general form for the time (t^*) and length (x^*) scales as given by [Verma et al., 2006] from the linear stability analysis:

$$t^* = \frac{12\mu\gamma}{h^3(\partial\phi/\partial h)^2} \qquad x^* = \sqrt{\frac{-8\pi^2\gamma}{\partial\phi/\partial h}} \tag{3.57}$$

In the case of pressure dominated flow, where only LVDW forces are present, the time and length scales can be found using equations (3.57). Following the work of [Khanna and Sharma, 1997] the time scaling (t^*), length scaling (x^*), and dominant length scale (λ_c), for a pressure dominated flow are:

$$t^* = \frac{12\pi^2\mu\gamma h_0^5}{A_L^2} \qquad x^* = h_0^2\sqrt{\frac{2\pi\gamma}{A_L}} \tag{3.58}$$

$$(\lambda_c)_{LVDW} = 2\pi h_0^2\sqrt{\frac{2\pi\gamma}{A_L}} \tag{3.59}$$

The scaling for an electrostatically dominated flow can be seen in equation (3.60). Note that the relations attained for the scaling time and scaling length use the normalizing electric field value E^* in equations 3.57.

$$t^* = \frac{3\mu\gamma h_0^3}{[0.5\epsilon_0\epsilon_p(\epsilon_p-1)\psi_{low}^2]^2} \qquad x^* = 2\pi\sqrt{\frac{\gamma h_0^3}{0.5\epsilon_0\epsilon_p(\epsilon_p-1)\psi_{low}^2}} \tag{3.60}$$

$$(\lambda_c)_{ES} = 2\pi\sqrt{\frac{2\gamma\psi_{low}}{\epsilon_0\epsilon_p(\epsilon_p-1)^2}}(E_p)^{-3/2} \tag{3.61}$$

3.2 Numerical Modeling

3.2.1 Numerical Method

System reduction The solution of Partial Differential Equations (PDE's) of order higher than two is challenging. The thin film evolution equations are fourth order non-linear PDE's. The high order and complexity induced by non-linearity requires numerical solution of the thin film equation (3.35). The solution methodology employed was the discretization of spatial derivatives using Finite Differences (FD) to reduce the PDE system to an algebraic differential equation system in time, which was then solved employing a differential algebraic solver.

3.2.2 Finite Difference Discretization

The finite difference discretization of equation (3.35) begins by generating the mesh to be used. In the simulations performed, a uniform cartesian grid was used. Adaptive meshing and non-uniform mesh spacing could be used and authors such as [Verma et al., 2006, Lenz and Kumar, 2007] have reported good results especially for applications where hole growth dynamics are of interest.

The thin film evolution equation was discretized using central differences in a pseudo staggered grid approach. In a purely staggered grid approach, values are stored at both grid centers and grid edges for different quantities. In the current formulation, this would involve storing film thickness (h) values at both grid centers and grid edges [Minkowycz et al., 1988, Acton, 1970]. The storage locations can be seen in Figure 3.2.

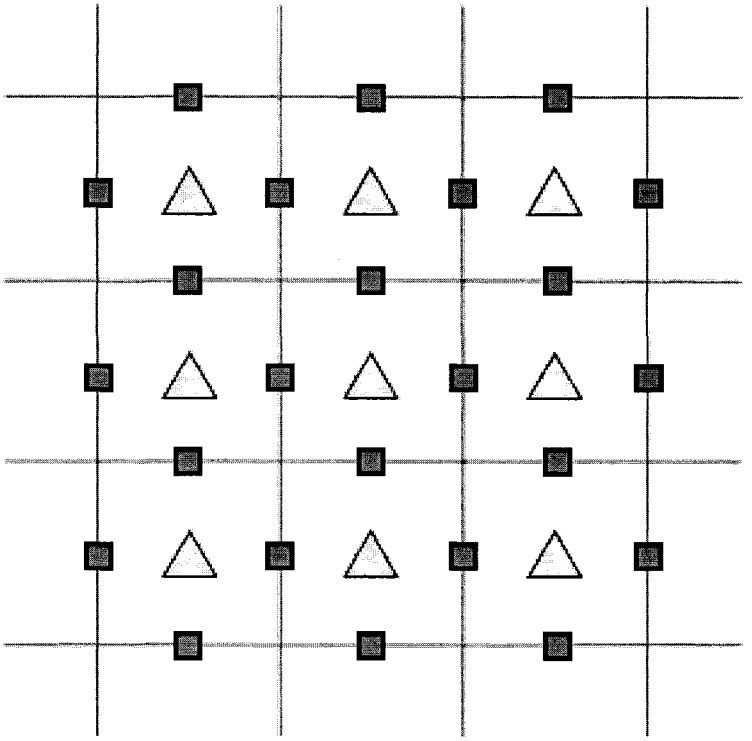

Figure 3.2: Comparison of alternate grid location schemes. Triangular points indicate grid centers while square values are mid-point values. In a staggered grid approach different values would be stored at mid-points and centers to help increase stability.

Figure 3.2 schematically shows a mesh with center locations (triangles) and mid-point or boundary points (squares). In this work, derivatives were taken at mid-points to increase accuracy and prevent checker boarding [1].

Derivative term approximation The general form of the thin film equation is shown as equation (3.35). In this equation, there are two distinct spatial components; one in the non-dimensional X direction and one in the non-dimensional Y direction. The following discussion will be limited to the discretization of X derivative terms

[1] Checker boarding refers to numerical inaccuracies that can occur due to the discritization used. The name refers to the way that adjacent points can be independent of each other in their discrete equations resulting in a checker board like pattern in the result [Minkowycz et al., 1988]

with the Y derivatives discretized in an analogous way.

The full X derivative term can be found by substituting for Ψ into equation (3.35).

$$\frac{\partial}{\partial x}\left[H^3\frac{\partial \Psi}{\partial x}\right] = \frac{\partial}{\partial x}\left[H^3\frac{\partial}{\partial x}\left\{\frac{\partial^2 H}{\partial x^2}+\frac{\partial^2 H}{\partial y^2}-\phi\right\}\right] \tag{3.62}$$

The discretization starts by taking a central difference for the outer most derivative [Minkowycz et al., 1988, Acton, 1970].

$$\frac{\partial}{\partial x}\left[H^3\frac{\partial \Psi}{\partial x}\right]_{(i,j)} \simeq \frac{1}{\Delta}\left[\left(H^3\frac{\partial \Psi}{\partial x}\right)_{(i+1/2,j)} - \left(H^3\frac{\partial \Psi}{\partial x}\right)_{(i-1/2,j)}\right] + O(\Delta^2) \tag{3.63}$$

where $\Delta = x_{(i+1,j)} - x_{(i,j)}$ is the uniform mesh spacing. The derivatives of Ψ are discretized using mid-point central differences (The equation is only scaled by Δ^{-1} due to the use of mid-point values). When equation (3.63) has the Ψ derivatives replaced at a point (i,j) by central differences, the resulting equation depends on values of Ψ at grid centers and H at mid-point values.

$$\begin{aligned}\frac{\partial}{\partial x}\left[H^3\frac{\partial \Psi}{\partial x}\right] \simeq \frac{1}{\Delta}\Bigg[&H^3_{(i+1/2,j)}\left(\frac{\Psi_{(i+1,j)}-\Psi_{(i,j)}}{\Delta}\right) && (3.64)\\ &-H^3_{(i-1/2,j)}\left(\frac{\Psi_{(i,j)}-\Psi_{(i-1,j)}}{\Delta}\right)\Bigg] && (3.65)\end{aligned}$$

Equation (3.64) shows the discretized relation for the x derivative term in equation (3.35). Equation (3.64) only requires the nodal values of Ψ, which can now have its definition substituted. The derivative terms in the definition of Ψ will be

approximated using three point central differences.

$$\Psi = \frac{\partial^2 H}{\partial x^2} + \frac{\partial^2 H}{\partial y^2} - \phi \tag{3.66}$$

$$\Psi_{(i,j)} \simeq \frac{1}{\Delta^2}\left[H_{(i+1,j)} + H_{(i-1,j)} + H_{(i,j+1)} + H_{(i,j-1)} - 4H_{(i,j)}\right] - \phi_{(i,j)} \tag{3.67}$$

When equation (3.67), is substituted into equation (3.64) the final form of the X-component of the spatial derivatives can be written as:

$$\begin{aligned}\frac{\partial}{\partial x}\left[H^3\frac{\partial \Psi}{\partial x}\right] \simeq \frac{1}{\Delta^2}\Big[H^3_{(i+1/2,j)} \\ \left\{\left[\frac{1}{\Delta^2}\left(H_{(i+2,j)} + H_{(i,j)} + H_{(i+1,j+1)} + H_{(i+1,j-1)} - 4H_{(i+1,j)}\right) - \phi_{(i+1,j)}\right]\right. \\ \left. - \left[\frac{1}{\Delta^2}\left(H_{(i+1,j)} + H_{(i-1,j)} + H_{(i,j+1)} + H_{(i,j-1)} - 4H_{(i,j)}\right) - \phi_{(i,j)}\right]\right\} \\ -H^3_{(i-1/2,j)}\left\{\left[\frac{1}{\Delta^2}\left(H_{(i+1,j)} + H_{(i-1,j)} + H_{(i,j+1)} + H_{(i,j-1)} - 4H_{(i,j)}\right) - \phi_{(i,j)}\right]\right. \\ \left. - \left[\frac{1}{\Delta^2}\left(H_{(i,j)} + H_{(i-2,j)} + H_{(i-1,j+1)} + H_{(i-1,j-1)} - 4H_{(i-1,j)}\right) - \phi_{(i-1,j)}\right]\right\} + O(\Delta^2)\Big]\end{aligned} \tag{3.68}$$

Equation (3.68) represents the finite difference approximation to the x component of equation (3.35). The equation is order $O(\Delta^2)$ accurate, with the only complication being the mid-point values of H required. The approximation of the mid-point values of H will be discussed in the following section.

3.2.3 Mid-point Interpolation

The discretization scheme was formulated to avoid so called 'checker boarding' in the solution. The formulation developed uses mid-point values of the film thickness

in non-linear terms. The mid-point values can either be approximated based on calculated values or solved for by adding additional equations. If the system had M_x points in the x direction and M_y points in the y direction, then calculation of the mid-point values would require an additional set of $2M_xM_y-(M_x+M_y)$ equations and the storage of the accompanying values. Since increasing the number of equations was not desirable, the values were approximated using Everett's method [Acton, 1970].

The mid-point values were found using a truncated version of Everett's method which explicitly uses central differences. If the value q is desired then it can be approximated using [Acton, 1970]:

$$q(p) = \begin{cases} (1-p)q_0 + E_0'' \cdot \delta_0'' + E_0^{(iv)} \cdot \delta_0^{(iv)} + \ldots \\ \quad +pq_1 + E_1'' \cdot \delta_1'' + E_1^{(iv)} \cdot \delta_1^{(iv)} + \ldots \end{cases} \tag{3.69}$$

Where

$$\begin{aligned} E_0'' &= \tfrac{-p(p-1)(p-2)}{3!} \\ E_0^{(iv)} &= \tfrac{(p+1)(p-3)}{4\cdot 5} E_0'' \end{aligned}$$

and

$$\begin{aligned} E_1'' &= \tfrac{p(p+1)(p-1)}{3!} \\ E_1^{(iv)} &= \tfrac{(p-2)(p+2)}{4\cdot 5} E_1'' \end{aligned}$$

q_i are the known nodal values at i $(i = 1, 2)$, δ_i'' is the second central difference $(\delta_i'' = q_{i+1} - 2q_i + q_{i-1})$, $\delta_i^{(iv)}$ is the fourth central difference and p is a scaling factor. The scaling factor is a representation of the normalized linear proximity to the right

most point being interpolated between.

$$p = \frac{x_{interp}}{x_1 - x_0}$$

Mid-point values are required in the finite difference approximation and the resulting scaling factor $p = 0.5$ and other values are $E_0'' = E_1'' = -3/48$. Substituting these values into equation (3.69) and truncating after the second differences, the final form of Everett's method can be written as:

$$q_{1/2} = (1/2)\left[q_1 + q_0\right] - (3/48)\left[\delta_1'' + \delta_0''\right] \tag{3.70}$$

where if the equation is written for the thickness (h) at the mid-point locations required for point (i, j) take the form:

$$\begin{aligned}
h_{(i+1/2,j)} &= (1/2)\left[h_{(i+1,j)} + h_{(i,j)}\right] - (3/48)\left[(h_{(i+2,j)}\right. \\
&\quad \left. + h_{(i,j)} - 2h_{(i+1,j)}) + (h_{(i+1,j)} + h_{(i-1,j)} - 2h_{(i,j)})\right] + O(\Delta^3) \\
h_{(i-1/2,j)} &= (1/2)\left[h_{(i,j)} + h_{(i-1,j)}\right] - (3/48)\left[(h_{(i+1,j)} + \right. \\
&\quad \left. h_{(i-1,j)} - 2h_{(i,j)}) + (h_{(i,j)} + h_{(i-2,j)} - 2h_{(i-1,j)})\right] + O(\Delta^3) \\
h_{(i,j+1/2)} &= (1/2)\left[h_{(i,j+1)} + h_{(i,j)}\right] - (3/48)\left[(h_{(i,j+2)} + \right. \\
&\quad \left. h_{(i,j)} - 2h_{(i,j+1)}) + (h_{(i,j+1)} + h_{(i,j-1)} - 2h_{(i,j)})\right] + O(\Delta^3) \\
h_{(i,j-1/2)} &= (1/2)\left[h_{(i,j)} + h_{(i,j-1)}\right] - (3/48)\left[(h_{(i,j+1)} + \right. \\
&\quad \left. h_{(i,j-1)} - 2h_{(i,j)}) + (h_{(i,j)} + h_{(i,j-2)} - 2h_{(i,j-1)})\right] + O(\Delta^3)
\end{aligned}$$

Using Everett's method, the mid-point values were approximated to the third order using central differences. The accuracy of the interpolation procedure was chosen as one order higher then that used in the central differencing scheme. This approximation should maintain the second order accuracy that exists in the rest of the numeric formulation. Everett's method is also used since the differences required are used in the general finite difference calculations, so little additional computation is required.

Boundary condition approximation In the problems considered in this work, two types of boundary conditions were employed. One, periodic boundary conditions are applied when modeling disturbances on homogeneous or periodically heterogeneous substrates. Two, in the case of an abrupt spatial step heterogeneity a combination of stationary fluid boundary conditions and periodic boundary conditions are applied. The stationary fluid boundary conditions are applied on the boundaries parallel to the step change heterogeneity.

When periodic boundary conditions are applied, the the domain modeled is a periodic component of the film which is repeated over the entire area. This means that any flow out of one boundary will result in inflow on the opposite boundary. Following the work of [Williams and Davis, 1982] the boundary condition implies that the first and last points on a row or column of mesh are equal. This means that a continuity of derivatives occurs over the boundaries, where for example the 2^{nd}

derivative in the x direction at the left boundary, $i = m$, is:

$$\frac{\partial^2 H}{\partial x^2}_{(m,j)} \simeq (1/\Delta^2)\left(H_{(2,j)} + H_{(m-1,j)} - 2H_{(m,j)}\right) \tag{3.71}$$

Equation (3.71) or an analogous form was applied at boundaries for periodic cases. The other type of boundary condition used was a stationary fluid boundary condition. When the fluid film is assumed stationary, the velocity components must be zero. Using the definition of the film velocity components defined in equations (3.33 and 3.34), a stationary fluid would imply that the first, second and third partial derivatives of H with respect to (x, y) are zero.

3.2.4 Solution of Numerical System

The thin film evolution equation is solved numerically by reducing the system of PDE's to a differential algebraic equation system using finite difference discretization of the spatial derivatives. The resulting set of algebraic differential equations is then solved using the fortran routine DDASSL.f from the numeric library SLATEC [Petzold, 1983].

Differential Algebraic Solver The DASSL algorithm solves a system of differential algebraic equations of the form [Maier et al., 1993]:

$$B(t, y, y') = 0 \tag{3.72}$$

where B, y and y' are N dimensional vectors, $y' = dy/dt$ is the velocity of y. A consistent set of initial conditions are required, and take the form $y(t_0) = y_0$, $y'(t_0) = y'_0$ and $B(0, y_0, y'_0) = 0$. When the spatial derivatives of equation (3.35) are discretized using the finite difference formulation shown in Section 3.2.2, the resulting equation system takes the form of equation (3.72).

The DASSL algorithm solves the N differential-algebraic equations for y and y', for a specified range of time (Δt). The algorithm first approximates the time derivatives and then solves the resulting non-linear system of equations. The integration algorithm uses backward differences to approximate the time derivatives and then uses a predictor-corrector method to solve the resulting system [Brown et al., 1994]. In the predictor-corrector method, an initial guess for the new solution is found by evaluating predictor polynomials, which interpolate from previous solutions. The solution is improved by the corrector step that evaluates a non-linear system of equations. The predictor and corrector polynomials are found by using backward differencing of order one through five [Maier et al., 1993,Brown et al., 1994]. The order of the differencing is successively increased until the desired accuracy is attained. The absolute solver tolerance was varied for a pressure based drainage case as an example of its influence on film drainage. The problem parameters for the study case are listed in Table 3.2.4. The influence of absolute error tolerance was investigated by comparing the change in volume conservation that occurred as the tolerance was changed. For all cases reported volume was conserved to $+/-1\%$. An absolute solver accuracy of 1×10^{-6} is used for all cases considered, it provides sufficient accuracy while not placing an

Table 3.1: Parameters used for testing of problem parameters

Parameter	Value
Viscosity (film, μ)	1 Pa s
Interfacial Tension (γ)	0.038 N/m
Relative permittivity ratio (ϵ_p)	2.5 [-]
Electrode Spacing (d)	100 nm
Initial film thickness (h_0)	20 nm
Close range repulsion distance (l_0)	0.137 nm
Domain Side Length (L)	30.7 nm
Effective Hamaker Constant (A_L)	1×10^{-20} J
Short-range repulsion constant (B_L)	6.63×10^{-76} J/m^6
Grid spacing	60×60

Table 3.2: Influence of absolute error tolerance

Absolute Error	% Volume Change
1×10^{-1}	5.36%
1×10^{-3}	3.45%
1×10^{-6}	0.024%
1×10^{-10}	−0.004%

undue constraint on the solution time.

The general solution algorithm can be seen in Figure 3.3. The program starts by checking to see if the case under consideration is new or a continuation of a previous run. If it is a new run, the mesh, velocity and thickness distributions are generated for the domain. If the run is a continuation, the mesh, velocities and thickness are loaded from data files that are passed to the program. The finite differencing begins by calculating second derivatives in both spatial directions (x, y) at all points in the domain. The calculated derivatives are then used in mid-point interpolations, after which the complete remaining finite difference discretization is performed. The calculated discretization is then used by DASSL in the solution of the differential-algebraic system. The time stepping within DASSL for a given time interval is automatically

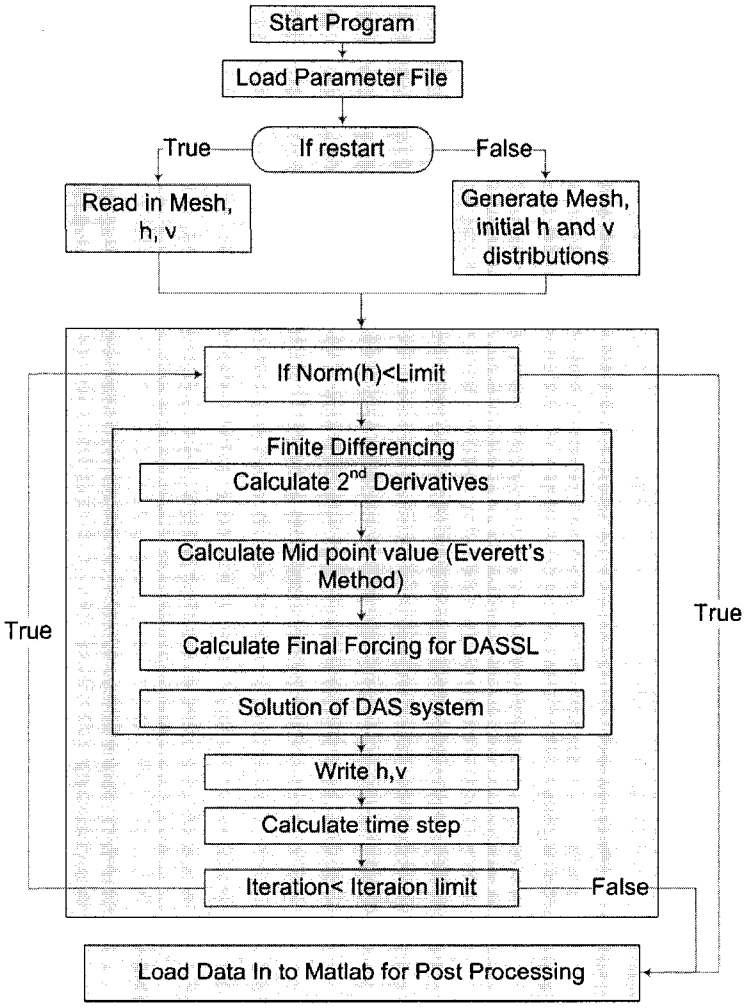

Figure 3.3: Numeric algorithm employed in the solution of the thin film equation.

selected, but to ensure convergence and view intermediate results a time step for DASSL to operate on is set in the main program. The time stepping was performed by using the largest time step from the previous calculation loop used by DASSL. For the first iteration no DASSL time stepping information is available, so a value of 1% of the passed total time is used as a default time in dimensionless units. After a time step is complete the values of velocity and thickness for the domain are written to data files and the iteration limit and convergence criteria are checked. The solution

is assumed converged when the linear norm gets lower than a threshold value Γ.

$$\sum_{i=1,j=1}^{i,j} (h(t) - h(t + \Delta t))^2 < \Gamma \tag{3.73}$$

Where i, j indicates the row and column of the point under consideration. The threshold for convergence was determined by running a number of test cases and finding a value that captured all film dynamics while minimizing extra run time and is varied depending on the dominate phenomena. In cases where pressure scaling is used $\Gamma = 1 \times 10^{-7}$ and $\Gamma = 1 \times 10^{-10}$ for cases that employed electrostatic scaling. The appropriate stop condition on the linear norm of equation (3.73) was found by examining the film drainage for a sample case. Figure 3.2.4 shows the temporal evolution of the maximum film thickness for the 20 nm thick film under the influence of the parameters listed in Table 3.2.4. Five separate simulations were run, one for each of the convergence criteria listed and one with a value of 20^{-20} where the simulation continued until a total iteration limit was violated. The dashed gray lines indicate the stopping location observed for different values of the linear norm stopping condition Γ.

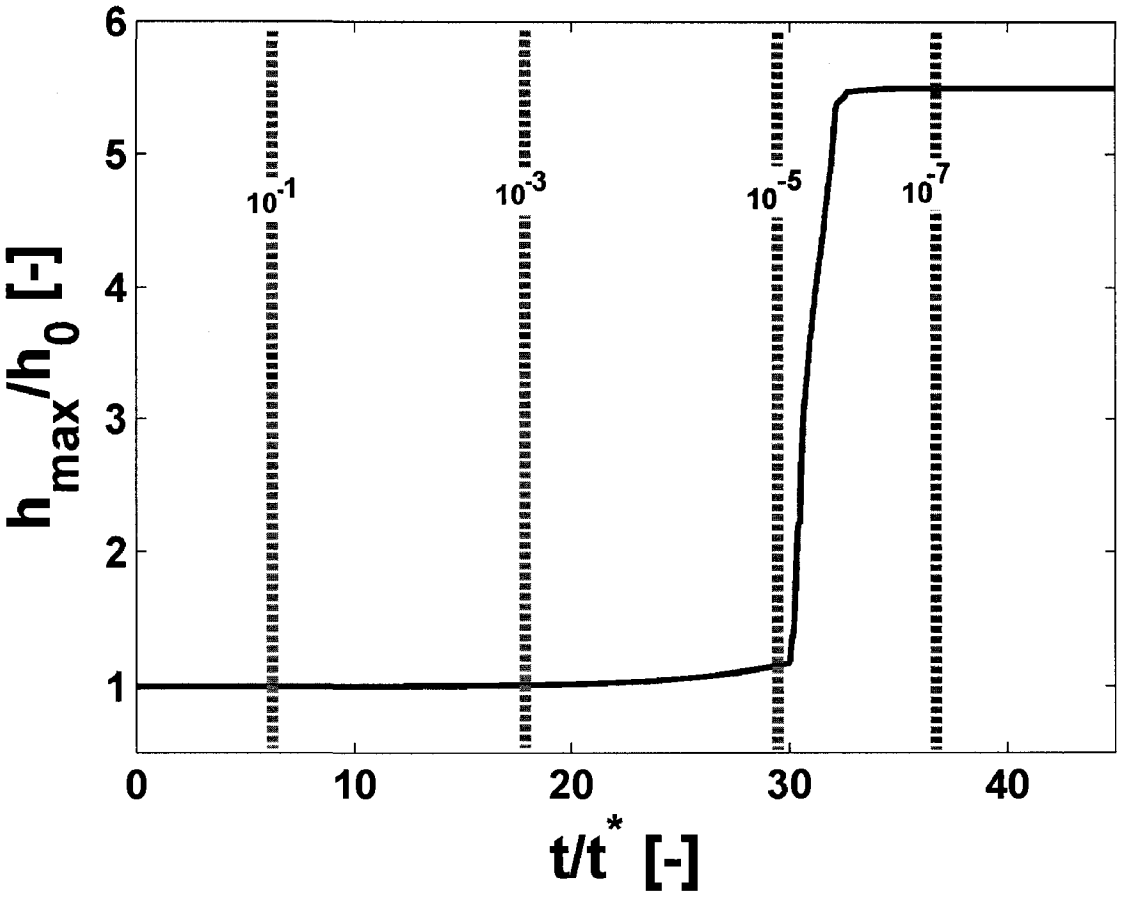

Figure 3.4: Evolution of a 20 nm thick film draining on a homogeneous substrate. All other parameters used are listed in Table 3.2.4. The dashed gray lines indicate where drainage ended for different linear norm stop criteria.

3.2.5 Domain Size and Meshing

For all the simulations performed square domains of side length (L) were used. The domain size chosen is important when periodic disturbances are modeled. [Khanna and Sharma, 1997] used a linear stability analysis of the thin film equation to determine critical length scales and estimate growth rates of disturbances. The critical wavelength (λ_c) was previously written for pressure and electrostatically dominated flows as equations (3.59) and (3.61). If a domain size (L) of less then the critical wave length as predicted by linear theory ($L < \lambda_c$) is chosen then film oscillations will be damped out but if the domain length is chosen larger then the critical wave length ($L > \lambda_c$) the oscillations will grow [Khanna and Sharma, 1997].

The domain size is important since it influences the film morphology and number of disturbance that can be observed. For simulations on homogenous and striped surfaces a domain size of twice the critical wave length (λ_c) will be used for all simulations. For cases an abrupt spatial step change in chemical a domain of $3\lambda_c$ was used and for electrical properties a domain of $6\lambda_c$ was used. The larger domain size was required to ensure that the stationary fluid boundary conditions did not influence the film evolution. Table 3.3 lists the recorded hole spacing at steady state and volume conservation for different mesh sizes for a pressure based drainage on a domain of $2\lambda_c$ with the parameters listed in Table 3.2.4. Linear theory predicts a hole spacing of $\sqrt{2}\lambda_c$ [Khanna and Sharma, 1997] and this will be used as a basis for comparing the mesh as it is refined. The use of a 60×60 grid ensured volume conservation and accuracy in the results for the test case shown. The simulation of

Table 3.3: Mesh refinement results

Mesh size	**Hole Spacing**	**% Volume Change**
30×30	1.25	4.86
60×60	1.3916	0.13
90×90	1.3929	0.09
120×120	1.3946	-0.03

step changes in chemical or electrical properties were on uniform cartesian grids of 90×90, while 60×60 cartesian grids were used for all other cases. The step change results were performed on a larger grid to account for the larger domain sized used.

Chapter 4

Film Drainage on Homogeneous Substrates

The drainage of thin films on homogeneous substrates can be instigated by both pressure and electrostatic forcing. The resulting film drainage varies depending on the dominant phenomenon. In this chapter, the evolved film morphologies and observed time scales will be compared for pressure and electrostatically driven thin film drainage. The comparison of times scales is conducted by studying the times required to reach pseudo stationary states starting from an initial uniform thickness. All simulations were performed on a homogeneous liquid film formed on a chemically homogeneous substrate.

4.1 Comparison of Conjoining/Disjoining Pressure Components

Drainage of thin films is induced by the conjoining/disjoining pressure, ϕ, which occurs as a result of intermolecular and electrostatic contributions as discussed in section 3.1. Film drainage is induced by gradients in the conjoining/disjoining pressure, not the absolute value. The gradient term accounts for both the spatial heterogeneity

and thickness variance of the conjoining/disjoining pressure. This can be seen if a gradient of the conjoining/disjoining pressure is expanded using the chain rule.

$$\nabla\phi = \frac{\partial\phi}{\partial h}\nabla h + \frac{\partial\phi}{\partial A}\nabla A + \frac{\partial\phi}{\partial E_p}\nabla E_p \tag{4.1}$$

where $A = A(x, y)$ is the spatially varying effective Hamaker constant and $E_p = E_p(x, y)$ is the spatially varying applied electric field at the film interface. The first term in equation (4.1) represents the contribution of the change of conjoining/disjoining pressure that occurs as film thickness varies. The second and third terms are contributions to the gradient that occur due to spatially varying properties of the system. Thus, the relative importance of different components can be seen by comparison of there partial derivatives with respect to film thickness ($\partial\phi/\partial h$). The close range Born-like repulsive terms will be neglected since they are only significant at small thickness where they dominate all other components.

Figure 4.1 shows the partial derivatives of the conjoining/disjoining pressure components with respect to film thickness ($\partial\phi/\partial h$) for different film thicknesses. The markers show the electrostatic contribution to the partial derivative of the conjoining/disjoining pressure ($\partial\phi_{ES}/\partial h$) for applied electric potentials 0.01, 1.0, 10 V. The lines show the LVDW contribution to the partial derivative of conjoining/disjoining pressure ($\partial\phi_{LVDW}/\partial h$) for effective Hamaker constants between 0.01, 0.1, 1 $\times$ 10^{-19} J. The base line parameters used in calculating the partial derivatives are listed in Table 4.1. The more negative the partial derivative the larger the disjoining force. The electrostatic contribution to the film drainage is most significant for

Table 4.1: Base line parameters employed in the comparison of conjoining/disjoining pressure components.

Parameter	**Value**
Viscosity (μ)	1 Pa s
Interfacial tension (γ)	0.038 N/m
Relative permittivity ratio (ϵ_p)	2.5 [-]
Electrode spacing (d)	100 nm

moderate to large applied voltages ($1 - 10\ V$) and thicker films $h > 30\ nm$. The magnitude increases as the film thickens. This leads electrostatically dominated drainage to favour the formation of thicker structures such as taller ridges and columns. The LVDW contribution to the partial derivative is significant as the film nears complete drainage ($h \rightarrow 0$). The magnitude increases as the thickness decreases, thus LVDW dominated drainage will typically form dry spots or holes. Based on the behaviour of the partial derivatives of the conjoining/disjoining pressure with respect to film thickness, the structures preferred by electrical and LVDW dominated drainage has been inferred. The film drainage that results from pressure and electrostatically dominated flows will now be investigated on homogeneous substrates.

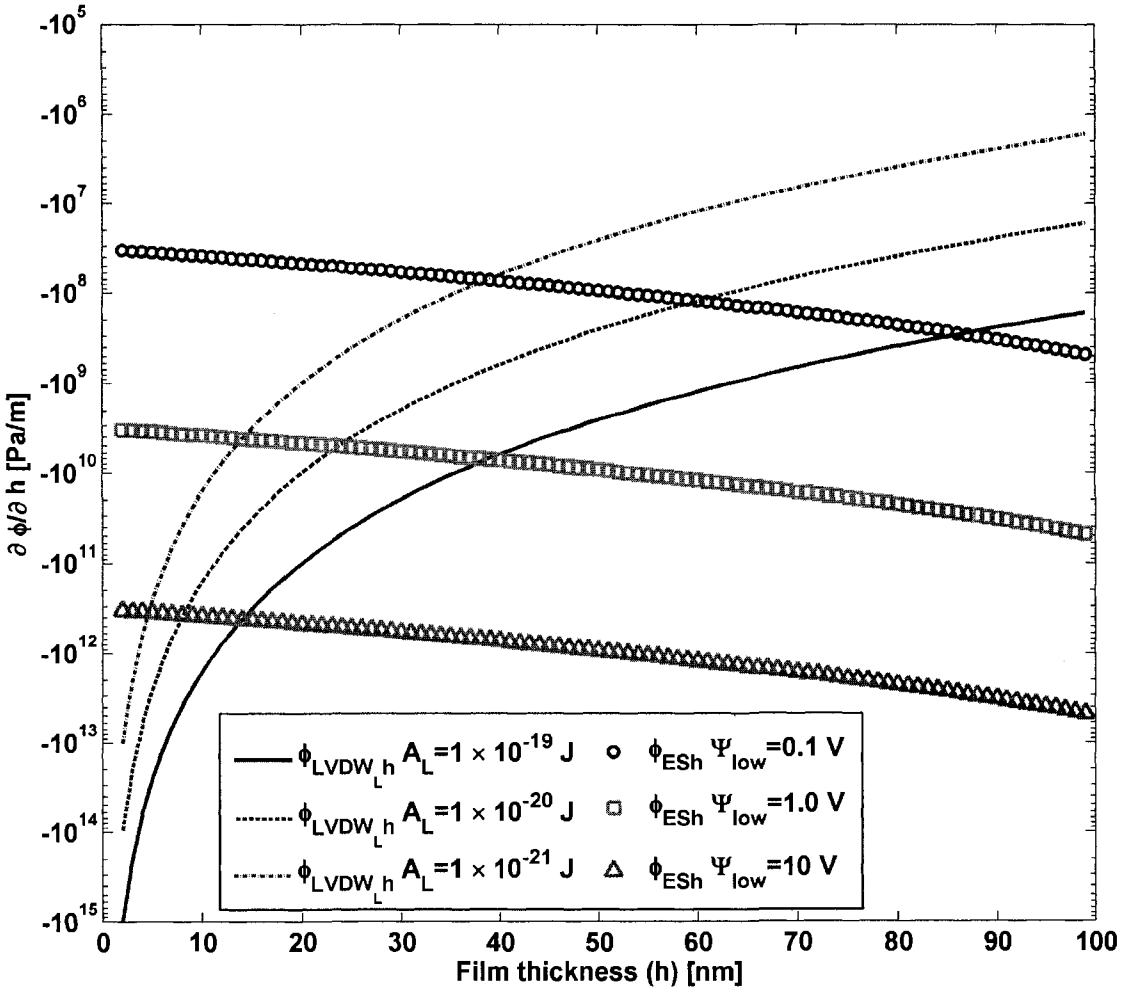

Figure 4.1: The partial derivative of conjoining/disjoining pressure components with respect to film thickness ($\partial\phi/\partial h$). The parameters used are shown in Table 4.1.

4.2 Pressure Based Drainage

The comparison of pressure and electrostatically dominated drainage will begin by examining pressure based drainage on a homogeneous substrate. In pressure based drainage, only LVDW interactions influence the film drainage. The base line parameters for pressure based drainage on a homogeneous substrate are shown in Table 4.2. The values in Table 4.2 were used for all simulations that follow, unless explicitly stated otherwise.

Table 4.2: Base line parameters employed in the simulation of pressure based drainage on a homogeneous substrate.

Parameter	**Value**
Viscosity (film, μ)	1 Pa s
Interfacial Tension (γ)	0.038 N/m
Relative permittivity ratio (ϵ_p)	2.5 [-]
Electrode Spacing (d)	100 nm
Initial film thickness (h_0)	20 nm
Domain Side Length (L)	7.77 μm
Effective Hamaker Constant (A_L)	1×10^{-19} J
Short-range repulsion constant (B_L)	6.63×10^{-76} J/m^6

The time evolution of the pressured based drainage for a film initially 20 nm thick can be seen in Figure 4.2. A square domain of side length $L = 2\lambda_c$, where λ_c is given by equation (3.59) was used in these simulations. The domain is discretized into a 60×60 cartesian grid. The gray-scale images represent the non-dimensional film thickness taken as snap shots in time. The film drains from a small initial perturbation (Figure 4.2a), eventually forming a coherent structure of holes and ridges (Figure 4.2b - f). Some of the depressions randomly turn into the fastest draining part of the film and lead to complete drainage and the formation of circular dry spots or holes (Figure

4.2c). After the formation of the first dry spot or hole, a second hole then forms (Figure 4.2f). In the final stages of drainage, the spacing between two adjacent dry spots (Figure 4.2f) is $1.38\lambda_c$. Linear theory predicts a hole spacing of $\sqrt{2}\lambda_c$ in pressure based drainage. Thus, the results of the numerical simulation are in good agreement with linear theory [Khanna and Sharma, 1997].

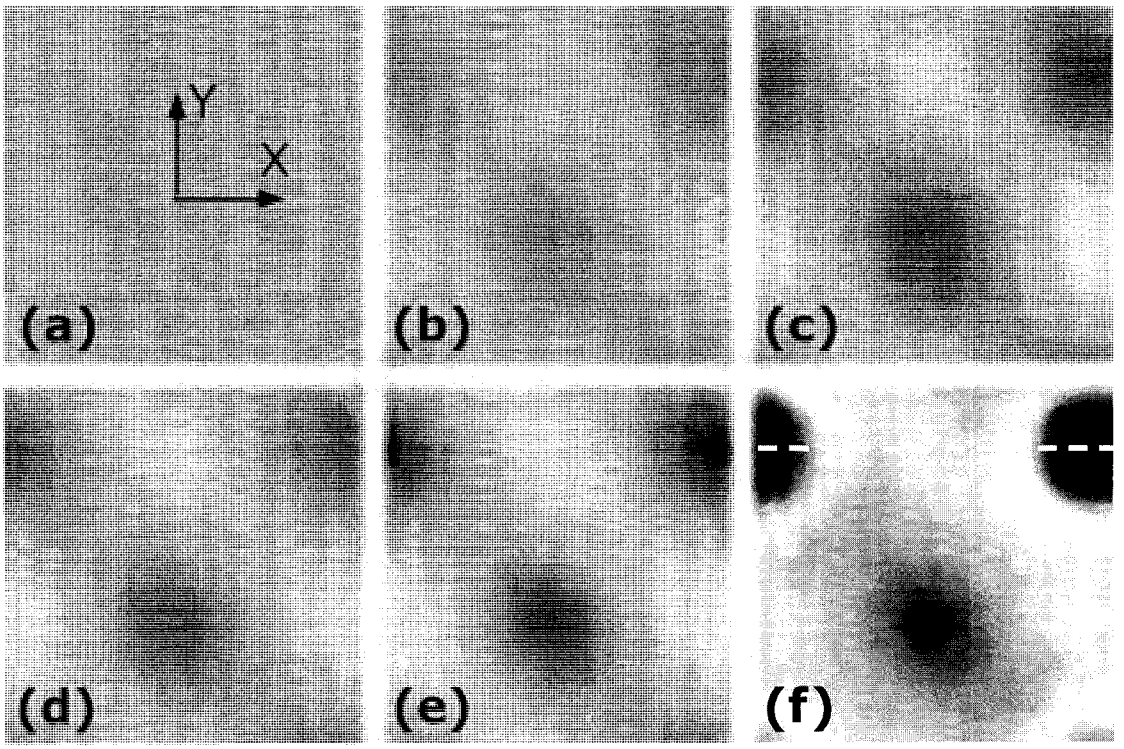

Figure 4.2: Evolution of a 20 nm thick film taken as gray-scale images of the film thickness. The times of the images starting in the upper left hand corner are: $t =$ 0.40, 21.40, 22.90, 23.40, 24.40, 24.80 s. A six point linear gray-scale was used in all images shown. The maximum is 25.96 nm (white) to a minimum of 1 nm (black). All other parameters were taken as base line values (Table 4.2).

The time evolution of the non-dimensional film thickness along a section view, shown as the dashed line in Figure 4.2f, is depicted in Figure 4.3. The $2D$ section views show the non-dimensional film thickness corresponding to the slice at $Y = 1.257$. The section cut was chosen so that it intersected the first hole (dry spot) that forms.

The Figure shows that ridges or lips form around the edges of the hole as it forms. It also demonstrates the films behaviour away from the hole formation. As holes or dry spots in the film form, the remainder of the film thickens and assumes a new equilibrium height but is otherwise not influenced by the formation of the hole. Pressure driven film drainage results in the formation a series of circular holes and surrounding ridges. The drainage is slow initially, but the final stages occur very rapidly in the last few seconds of drainage.

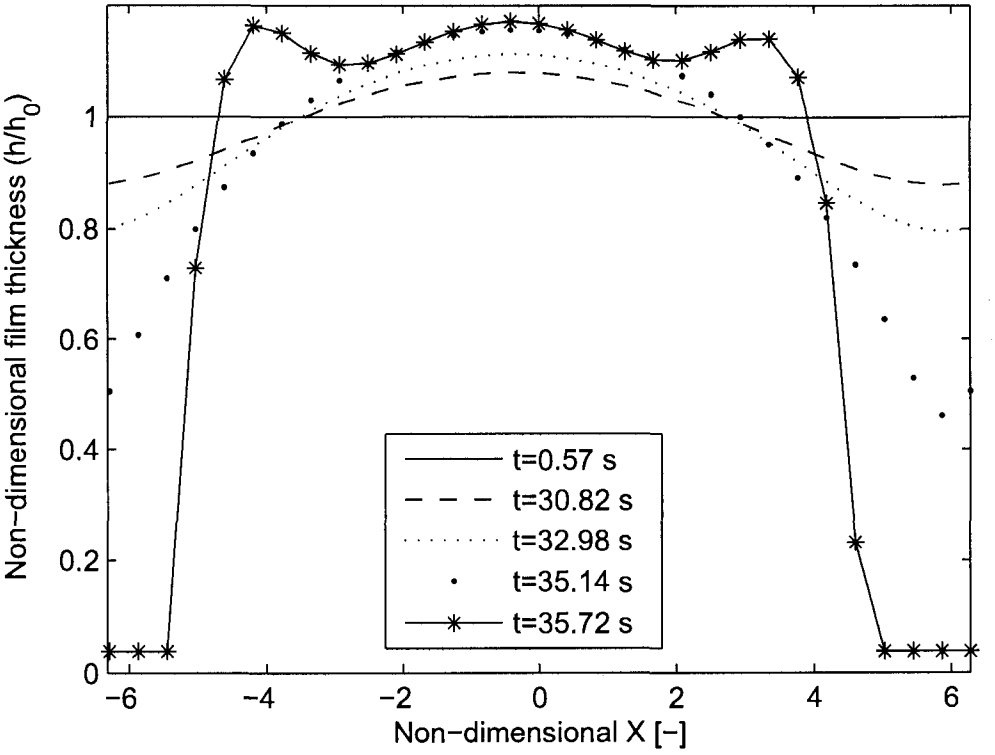

Figure 4.3: Evolution of a 20 nm thick film taken as section views of the non-dimensional film thickness. The section views are taken at $Y = 1.257$ which can be seen as the dashed line in Figure 4.2f.

4.3 Electrostatic Based Drainage

The influence of an applied electric field on the drainage of a thin film will now be discussed. Figure 4.4 shows a series of gray-scale images that represent the final structures formed by a 20 nm thick film subjected to increasing magnitudes of applied electric fields. The simulations are performed on a 60×60 cartesian grid with a side length $L = 7.77\ \mu m$. Comparing Figure 4.4a and Figure 4.4b, the purely pressure based drainage ($E = 0$, Figure 4.4a) is quite similar to the structure attain when an applied electric field of 0.45 MV/m was applied (Figure 4.4b). When the applied field is increased another order of magnitude to 4.50 MV/m (Figure 4.4c), the film morphology changes noticeably. The hole growth has become more uniform with the size of the two holes that form becoming almost equal. The application of small electric fields, even as low as 4.50 MV/m add uniformity to the structures that are formed. This behaviour was also visible in Figure 4.4d with an applied field of 11.36 MV/m. When the applied field was increased to 27.27 MV/m (Figure 4.4e) the drainage that the film under goes is noticeably changed. The size of the dry spots or holes that form is reduced and localized elevated patches or columns can be seen. As the magnitude of the applied field is increased to 45.45 MV/m (Figure 4.4f), the size of holes and columns that form becomes even smaller.

The morphology of the drained film clearly indicates how increasing the applied electric field above a threshold value of *ca.* 5 MV/m changes the nature of the film drainage. At higher applied fields, the film morphology develops subtle differences from those obtained under solely pressure driven drainage. With the application of an

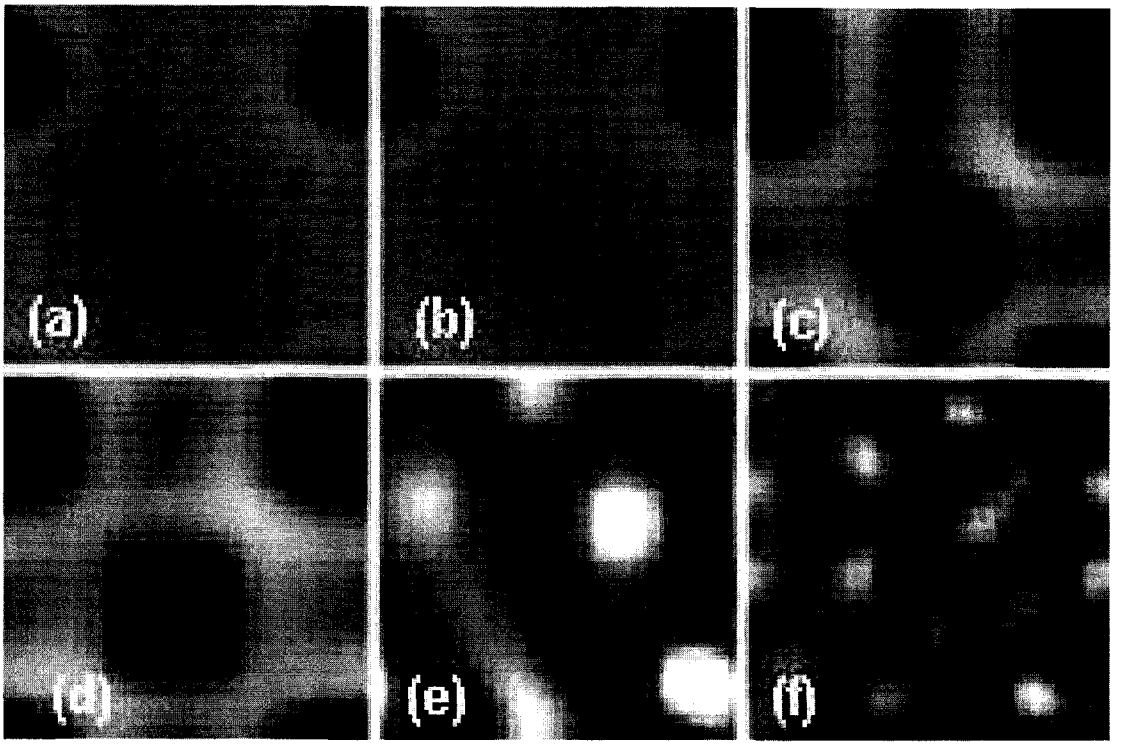

Figure 4.4: Comparison of final film structures for a 20 nm film subjected to different magnitudes of electric field. The magnitude of the applied electric fields are (from upper left to lower right): $E_p = 0.00,\ 0.45,\ 4.50,\ 11.36,\ 27.27\ ,\ 45.45\ MV/m$. A linear gray-scale is shown in all images with a maximum value of 39.61 nm (white) to a minimum value of 1.00 nm (black). All other parameters were taken as base line values.

electric field of magnitude $> 25\ MV/m$, the film drainage becomes dominated by electrostatic effects, as shown by the formation of columnar structures separating smaller holes, as well as an increase in the density of features observed over the simulated region. The application of an electric field will also increase the maximum observed film thickness, and in the case where large fields are applied ($E_p > 25\ MV/m$) columns will form.

Figure 4.5 shows the evolution of the minimum non-dimensional film thickness for an initial 20 nm thick film under the influence of different magnitudes of applied

electric fields evolving with time. The minimum film thickness was found by locating the lowest point in the domain and tracking its drainage. The drainage time decreases as the magnitude of the applied voltage on the lower electrode, ψ_{low}, and therefore, the initial electric field at the interface, *cf.* Eq. (3.55), is increased. Note that the electric field changes with time as the film morphology evolves in each simulation, although the applied potential, ψ_{low} remains fixed. For applied voltages of up to 0.1 V, no perceptible change in the drainage behavior compared to pressure based drainage is observed. At higher applied potentials, the drainage becomes quicker. The initial decrease in height is almost independent of the applied potential, following which, a rapid change in height with time is observed. As the magnitude of the applied electric field is increased, the time taken to attain the final height is considerably reduced. Finally, at an applied voltage of 10 V, the drainage is virtually instantaneous compared to the time taken for drainage of a film under the influence of purely van der Waals interactions.

The application of an electric field allows the manipulation of length and time scales for film drainage. This presents a unique opportunity to use electric fields to aid in pressure drainage, or create structures that would otherwise not occur in purely pressure driven drainage. In pressure dominated drainage, dry spots or holes are the primary structures formed while the growth of columns dominate in electrostatically dominated flows. There is, however, a region of applied field strength that increases the rate of hole growth but does not change the spatial or temporal length scales of the structures formed.

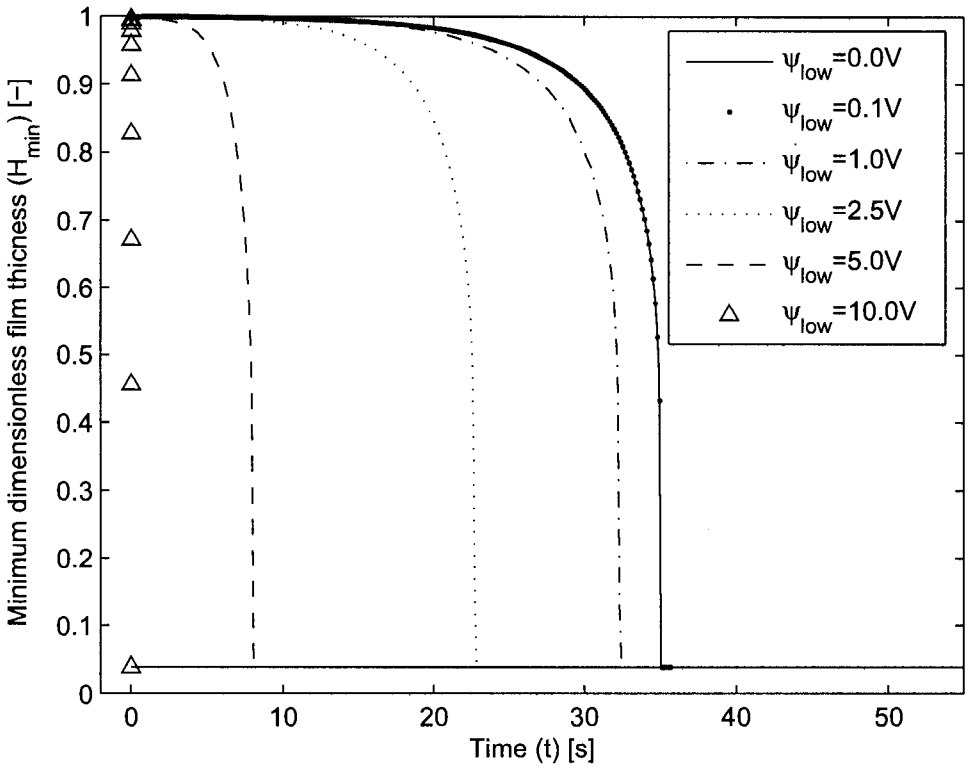

Figure 4.5: Minimum non-dimensional film thickness for a 20 nm thick film for various applied electric fields. All other parameters were taken as base line values.

Film drainage on a homogeneous substrate has established the general drainage behaviour of pressure and electrostatically driven flows. In pressure dominated drainage, independent dry spots are formed with predictable spacing in the domain. The holes are surrounded by ridges in their immediate vicinity but otherwise don't influence the remainder of the film. When electric fields are applied, the film behaviour changes. For small fields $E_p < 11.37\ MV/m$, the pressure drainage is aided and the film drainage occurs more rapidly with the ridges and dry spots that form becoming more uniform. As the strength of the applied electric field is increased $E_p > 27\ MV/m$, the dominant structure observed in the film shifts from holes to columns. Larger

electric fields create drainage dominated by electrostatics and result in periodic arrays of columns forming. Increasing the initial film thickness slows the drainage time for pressure based drainage but speeds the rate of upper surface wetting in electrostatically dominated flows. The film morphologies that are formed by drainage on a homogeneous substrate consist of some combination of holes and columns. If more elaborate film structures are required, alternate means of drainage must be found.

The use of electrical or chemical heterogeneity to influence drainage creates the possibility for a wide array of drainage phenomena. Heterogeneity creates opportunities to produce drainage that would not occur in a film on a homogeneous substrate. The study of electrical and chemical heterogeneity will commence after a series of validation cases are discussed.

4.4 Model Validation

The numerical model was validated by comparing the results to published experimental and numerical studies. In the work of [Khanna and Sharma, 1997] the drainage of a thin film under the influence of pressure was studied using $3D$ numerical simulation of the film drainage. The size of the domain was varied around the predicted critical wave length (λ_c) as calculated from linear theory. When the domain was smaller than this critical length ($L < \lambda_c$) disturbances were damped out, and when the domain was larger film rupture occurred. When scaled the critical wave length $\lambda_c^* = 2\pi$, is used to test the problem scaling.

Figure 4.6 shows gray-scale images of the pressure based film drainage of a 1 nm thick film on two different domain sizes. Figure 4.6a $-$ c show a domain $L = 0.98\lambda_c^*$ and Figure 4.6d $-$ f show a domain $L = 1.02\lambda_c^*$. As predicted by linear theory and reproducing the results of [Khanna and Sharma, 1997], the film drainage is damped out for a domain size $\leq \lambda_c^*$. When the domain size is increased above the critical length, $L = 1.02\lambda_c^*$, drainage results in film rupture. These results demonstrate the problem scaling for pressure based drainage is correct and will produce accurate results.

The drainage that occurs under the influence of an applied electric field is validated by examining a case presented by [Verma et al., 2005], that was experimentally validated by [Voicu et al., 2006]. The drainage of a 50 nm thick film between two electrodes spaced 100 nm apart and subjected to an electric field of $E_p = 400\ MV/m$ ($\psi_{low} = 70\ V$). The film considered is inherently stable since it completely wets

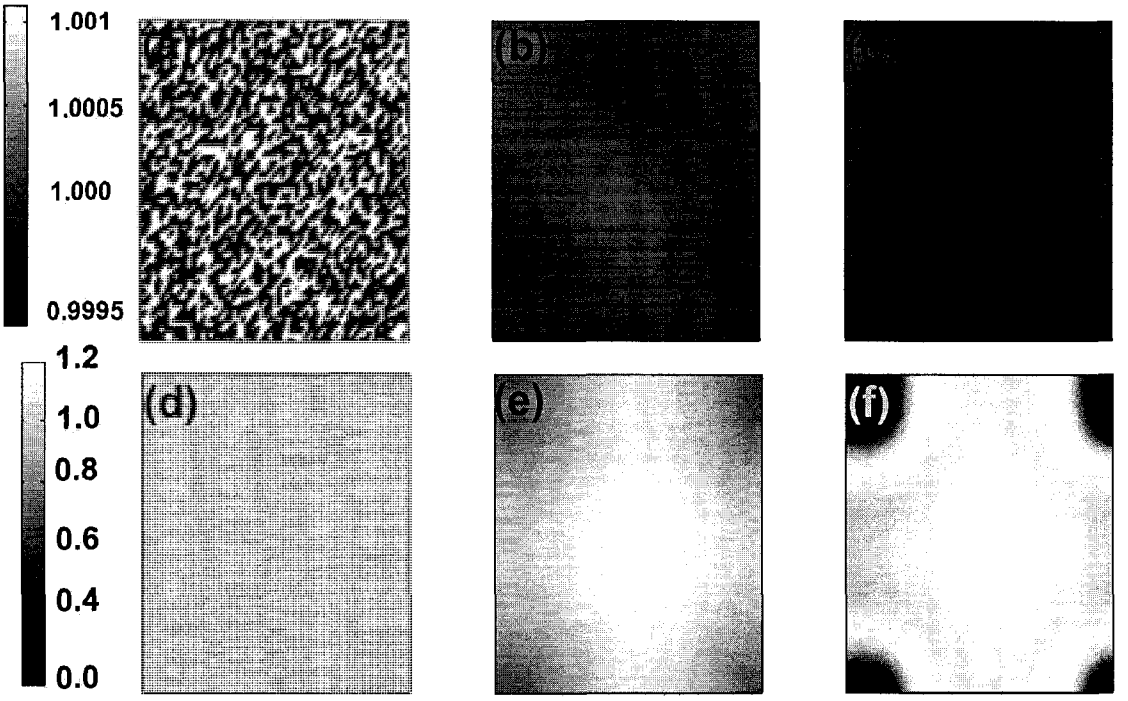

Figure 4.6: Evolution of a 1 nm thick film on a domain sizes of $L = 0.98\lambda_c$ in panels (a $-$ c) and $L = 1.02\lambda_c$ in panels (d $-$ f). The gray-scale images represent the film thickness, as indicated by the scale-bar on the left side of the row the image is located on. The dimensionless times of the drainage for the domain of $L = 0.98\lambda_c$ are $t/t^* = 0,\ 0.20,\ 26.0$ and for $L = 1.02\lambda_c$ are $t/t^* = 0,\ 102.5,\ 300$.

the lower surface. The complete wettability is represented by the effective Hamaker constant which has a value of $-2 \times 10^{-20}\ J$.

Figure 4.7 shows the number of columns observed in the domain evolving in non-dimensional time. This figure shows a comparison of the results produced in the current study (dashed line with circle markers) to the numerical results of [Verma et al., 2005] (square markers with solid lines). The columns are found in the current work by taking snap shots of the non-dimensional film thickness as gray-scale images. These images are then examined and the features that have attained the maximum film thickness are counted as columns. The film evolution predicted numerically is

in good agreement with the numerical results of [Verma et al., 2005]. The numerical results of [Verma et al., 2005] were validated experimentally by the work of [Voicu et al., 2006]. In the work of [Voicu et al., 2006], qualitative agreement between the work of [Voicu et al., 2006] and the numeric work of [Verma et al., 2005] was attained. Good agreement is noted between the current work and the published work of [Verma et al., 2005] and by analogy the experimental work of [Voicu et al., 2006]. These results indicate that film drainage under electrostatic forcing is being accurately captured and heterogeneity will be considered in the following chapters.

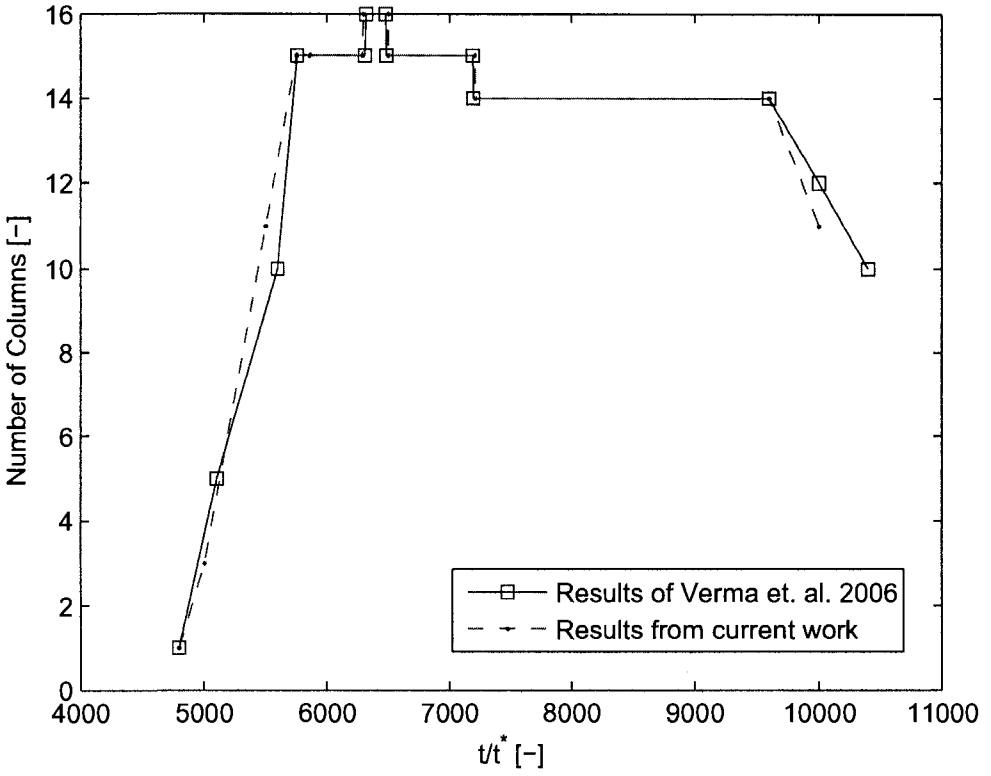

Figure 4.7: Comparison of the number of columns formed by a 50 nm thick film deforming under the influence of an applied electric field. The squares represent the numerical results of [Verma et al., 2005], which were experimentally validated by [Voicu et al., 2006] for a $h_0 \simeq 125$ nm thick film that has the same ratio of electrode spacing to initial film thickness as that seen in the two numerical cases. The film properties for the numerical studies are $h_0 = 50$ nm, $d = 100$ nm, $\epsilon_p = 2.5$, $\mu = 1$ $Pa\ s$, $\gamma = 0.038$ N/m and $A = -2.0 \times 10^{-19}$ J.

Chapter 5

Thin Film Drainage on Chemically Heterogeneous Substrates

In this chapter, the influence of spatial heterogeneity in effective Hamaker constant on pressure based film drainage will be examined. Pressure driven thin film drainage on a homogeneous surface is detailed previously in Chapter 4. The heterogeneity in the effective Hamaker constant considered are an abrupt step change and periodic stripes. A step change is used to examine the film drainage response to an isolated spatial variance in the intermolecular forcing. While a striped pattern demonstrates the interactions induced by a series of changes. The influence of film thicknesses (h_0), ratios of effective Hamaker constants (A_1/A_2), and spacing between the upper and lower surfaces (d) are studied to determine their influence on film drainage. The range of film thicknesses, spacing between surfaces and effective Hamaker constants, as well as other baseline parameters used in the subsequent simulations are shown in Table 5.1.

To simulate chemically heterogeneous surfaces, a small random perturbation to

an initially stationary film of uniform thickness h_0 is introduced. The simulations are then run until the films reached a pseudo stationary state. The film is considered stationary when the linear norm, previously written as equation (3.73), of the non-dimensional film thickness changed less then 10^{-7} over a time step. Details of the numerical methodology employed to solve the system of equations for this case were given in section 3.2.4. For some cases, the 'long-time' evolution of the film was desired, so the convergence criteria was reduced to 10^{-10} so that behaviour beyond the pseudo stationary state could be observed.

In the remainder of this chapter, details of the thin film drainage on different chemical heterogeneity are given. First, results for heterogeneity in effective Hamaker constant are compared to results reported in Literature. The study of step changes in effective Hamaker constants in literature is limited since typically works have focused on periodic striping instead. The study of heterogeneity in effective Hamaker constant is extended by a detailed study of the times taken for drainage and the introduction of an inert upper surface. The influence of homogeneous electric fields on surfaces with a step change in effective Hamaker constant is explored to conclude the chapter

Table 5.1: Baseline parameter values and ranges of additional parameters employed in the simulation of heterogeneity in effective Hamaker constant.

Parameter	**Value**
Viscosity $(film, \mu)$	$1.00\ Pa \cdot s$
Interfacial Tension (γ)	$3.80 \times 10^{-2}\ N/m$
Effective Hamaker constant (A_1)	$1 \times 10^{-19}\ J$
Distance between surfaces (d)	50-400 nm
Effective Hamaker constant (A_2)	$1 \times 10^{-22} - 5 \times 10^{-19} J$
Domain Length (L)	$1.85 - 938\ \mu m$
Initial Film Thickness (h_0)	$20 - 80\ nm$

and represents an area not available in the literature.

5.1 Effective Hamaker Constant Patterning

Chemical patterning was created by systematically changing the effective Hamaker constant (A_L) of the Lifshitz van der Waals (LVDW) interactions. The effective Hamaker constant captures the interaction between the lower solid surface and the film-bounding fluid interface. The influence of a spatially isolated, abrupt change (step change) in Hamaker constant (A_L) is considered initially.

The physical system in Figure 5.1, shows the implementation of an abrupt spatial step change in effective Hamaker constant. Figure 5.1a shows the (x, y) plane view of the spatial step change. Figure 5.1b shows the (x, z) plane view of the step change. For reference, the initial film thickness (h_0) and distance between the upper and lower solid surfaces (d) have been included. The abrupt step change is created by bringing two semi infinite planes together and having them abut. The left half domain has an effective Hamaker constant (A_1) and dimensions (L_{x1}, L_y). The right half domain has an effective Hamaker constant (A_2) and dimensions (L_{x2}, L_y). The domain is modeled as square ($L = L_x = L_y$) and is equally divided between the two half domains. In the y direction the domain is modeled as periodic, while in the x direction, the domain is modeled as infinite. On the x boundaries, stationary fluid boundary conditions are applied to model the infinite nature of the domain. The length $L = 3\ \lambda_c$ is chosen to ensure that the boundary conditions do not influence the drainage (λ_c is the critical wave length as predicted by linear theory for a homogeneous substrate as given by

equation 3.59). The domain size used for abrupt spatial changes is found using the larger effective Hamaker constant. The larger effective Hamaker constant produces smaller structures ($\lambda_c \propto 1/A$), and was chosen to ensure that small features in the film drainage would be adequately captured.

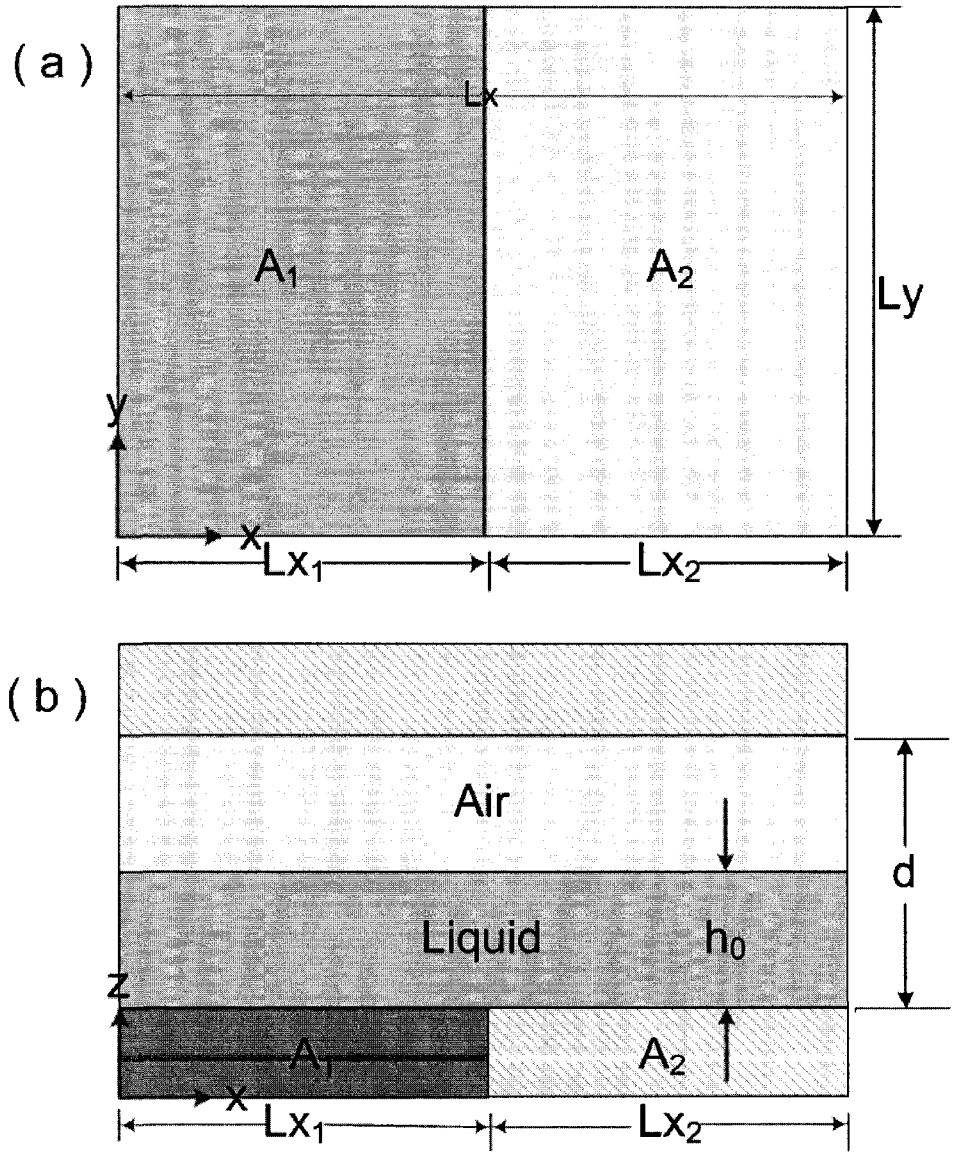

Figure 5.1: Schematic representation of the thin film system under the influence of an abrupt spatial step change in effective Hamaker constant.

Following the analysis of a spatial step in effective Hamaker constant, a periodic array of alternating stripes of different effective Hamaker constants is considered. Figure 5.2, schematically shows the physical system of alternating stripes of effective Hamaker constant. Figure 5.2a shows the (x, y) plane view and Figure 5.2b shows the (x, z) plane view of the system of alternating stripes of effective Hamaker constant. The stripes are modeled on a square domain of side length (L). The striped materials alternate between Hamaker constants of A_1 with stripe width w_1 and A_2 with stripe width w. Typically, $A_1 > A_2$ for the simulations performed. The stripe pattern can also be defined using the pitch or frequency in the x direction (L_p) of the stripes. The pitch or periodicity is defined as the center to center distance between two consecutive stripes of the same material. The periodicity is related to the stripe widths by $L_p = w + w_1$. The stripe patterns are defined using the periodicity L_p and the stripe width w. A square domain of side length $L = 2\lambda_c$ is used, where λ_c is the dominant wave length predicted from linear theory for a homogeneous surface. The value of λ_c is calculated using A_1, since the larger the effective Hamaker constant, the smaller the dominant wave length predicted by linear theory. Using the larger value of the effective Hamaker constant (A_1) results in smaller domain sizes and finer spatial resolution.

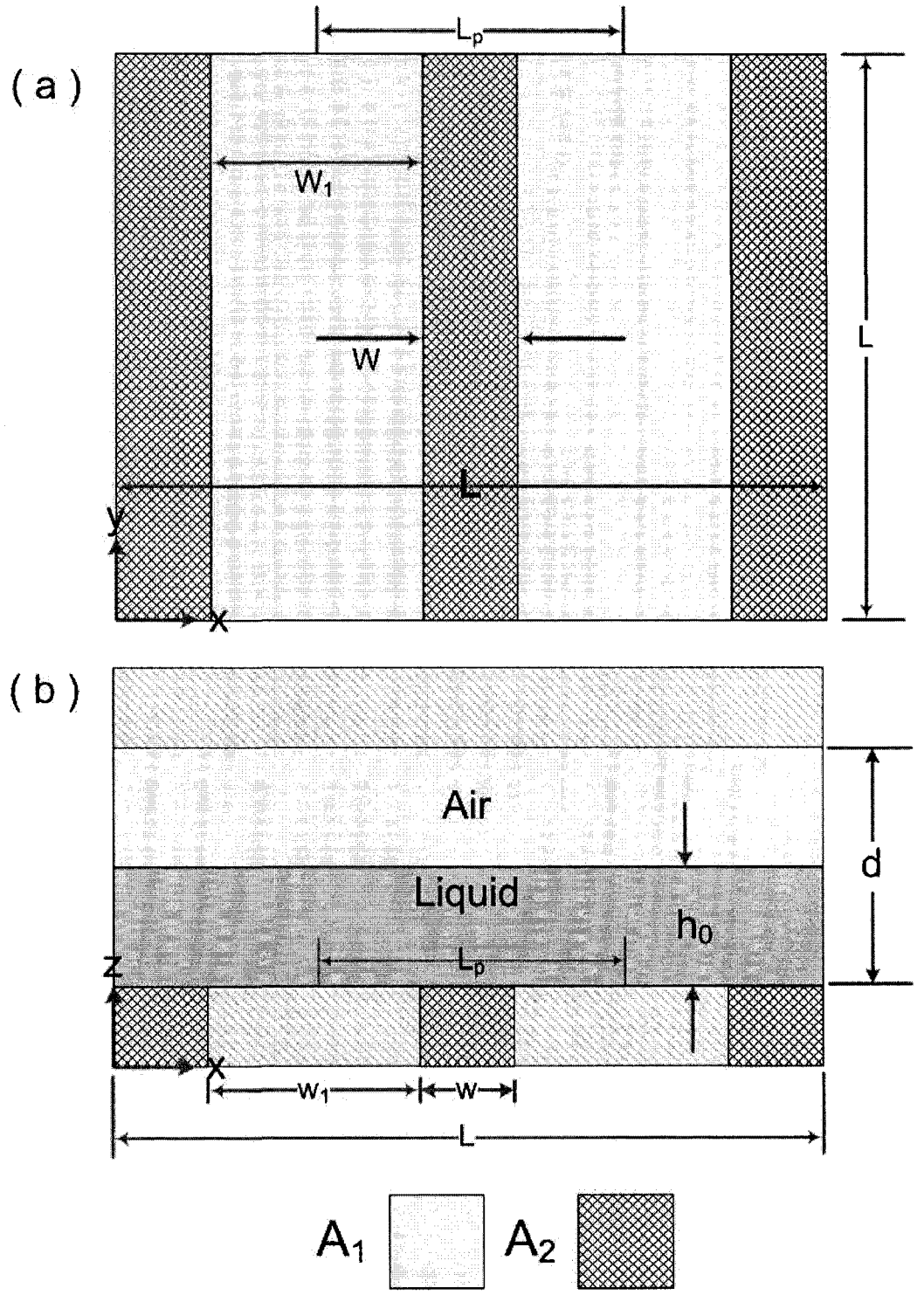

Figure 5.2: Schematic representation of the thin film system under the influence of periodic striping in effective Hamaker constant.

5.2 Step Change in Chemical (LVDW) Pattern

5.2.1 Drainage Patterns

The drainage of a thin film under the influence of spatially varying effective Hamaker constant leads to new and novel means of altering and shaping film drainage. The abrupt spatial step change in effective Hamaker constant acts as a base case for studying more elaborate patterns. When a periodic system of alternating stripes of effective Hamaker constant is considered, the resulting flow occurs due to many spatial heterogeneities interacting. Here the abrupt spatial step change in effective Hamaker constant provides useful insight and a basis for the study of periodic patterns in section 5.3.

The abrupt spatial step change in effective Hamaker constant is created by fixing the effective Hamaker constant in the left half domain at $A_1 = 1 \times 10^{-19}\ J$, while setting the effective Hamaker constant in the right half domain (A_2) to a value other then the left half domain ($A_1 \neq A_2$).

Figure 5.3 shows the temporal evolution of the film thickness for a 20 nm thick film subjected to a spatial step change in effective Hamaker constant ($A_1/A_2 = 100$), with a spacing between the upper and lower surfaces of $d = 400\ nm$. The figure shows a series of gray-scale snapshots (Figure 5.3b – Figure 5.3f) of the simulated film thickness (Z direction) over the (x, y) plane at different instances. The scale-bar represents the film thickness. Figure 5.3a schematically shows the effective Hamaker constant distribution of the lower surface over the (x, y) domain, and is independent

of the scale-bar. The film drains from an initial random perturbation (Figure 5.3b) to form a ridge and moat structure (Figures 5.3c – f) parallel to the step change in effective Hamaker constant. The drainage evolves with a rapid initial decrease in film height in the vicinity of the step change forming a narrow moat (Figure 5.3 c), offset slightly to the left of the location of the step change. As the moat forms there is an accompanying increase in height (a ridge) that forms on the two sides of the moat. These features intensify over time; the moat continues to grow in width, while the two adjacent ridges become higher. The simulation is run till equilibrium when equation (3.73) changes by less than 10^{-10} between adjacent time steps. At equilibrium, the ridge on the far left of Figure 5.3f reaches a height that is approximately twice as high as the ridge toward the right hand side of the moat. An interesting feature of the drainage behaviour is that the left-hand-side ridge initiates later (less prominent in Figure 5.3c), but eventually becomes more prominent as the film attains equilibrium (it is sharper and higher in Figure 5.3f). $3D$ renderings of Figures 5.3b, e and f are shown in Figure 5.4. The $3D$ renderings were produced by plotting all of the recorded film thicknesses in the domain using Matlab. The figure shows the changes in film thickness as the ridge and moat structures previously mentioned evolve.

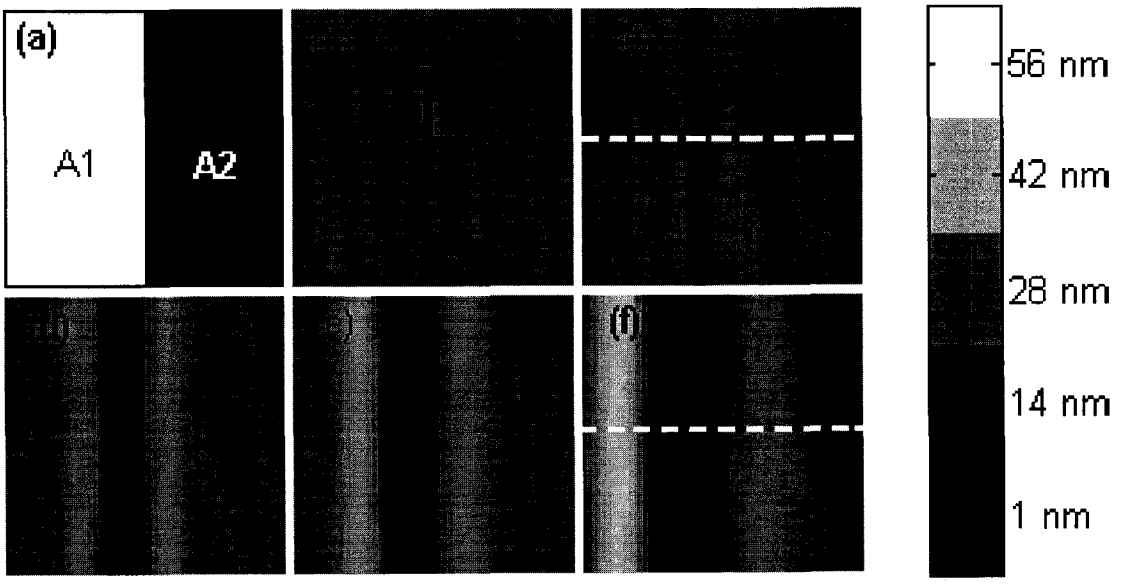

Figure 5.3: Evolution of a 20 nm film under the influence of a step change in effective Hamaker constant $A_1/A_2 = 100$. The scale-bar on the right does not apply to (a) but shows the distribution of effective Hamaker constant. Panels (b – f) show the film thickness at times $t = 0.0032,\ 6.5561,\ 6.9511,\ 7.3691,\ 8.5299\ s$. The simulation shown was performed on a domain of $L = 3\lambda_c = 11.64\ \mu m$, $\lambda_c = 3.88\ \mu m$ and the time is scaled with $t^* = 1.44\ s$. The initial film thickness of 20 nm can be seen in panel (b). All parameters not discussed were taken as baseline values.

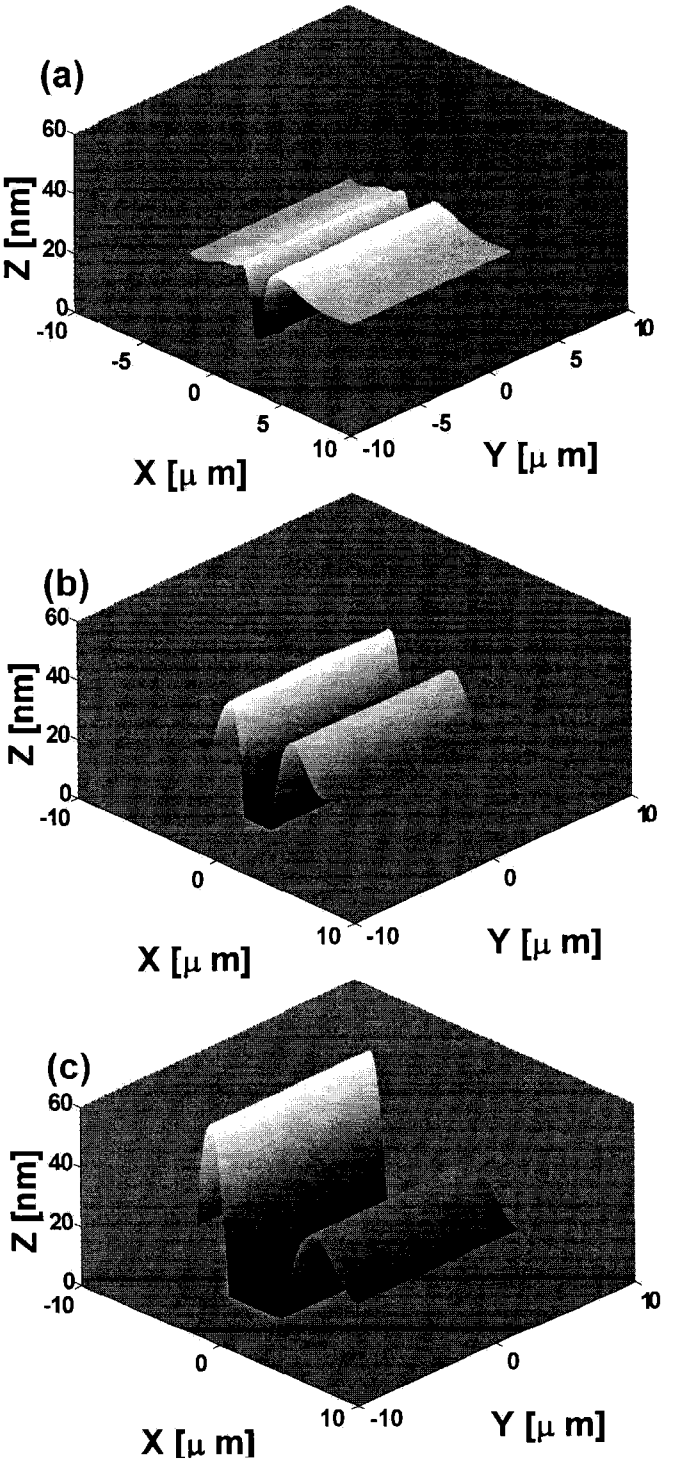

Figure 5.4: 3D film morphologies of the pseudo color plots shown previously in Figure 5.3c, e and f (a – c of current Figure).

Section views of non-dimensional film thickness profiles at scaled times $t/t^* = 4.55$ and 5.92, taken at the locations of the dashed lines in Figure 5.3c and 5.3f, are shown in Figure 5.5 and Figure 5.6. Films of initial thickness $h_0 = 20, 50, 80\ nm$ are pictured as snap shots of there evolution between surfaces separated by $d = 400\ nm$ and a ratio of effective Hamaker constants of $A_1/A_2 = 100$. Despite having different initial thicknesses, the three films have the same non-dimensional drainage behaviour when subjected to the same step-change in chemical heterogeneity. In dimensional quantities the film drainage changes significantly as the film thickness is varied since the domain size, scaling time and thickness scaling change as functions of the initial film thickness. For films of initial thickness $h_0 = 20, 50, 80\ nm$ the scaling times are $t^* = 1.44, 141, 1.47 \times 10^3\ s$ and domain sizes $L = 11.46,\ 73.00,\ 186.50\ \mu m$. For cases where the film does not interact with the upper surface and has an initial thickness $< 100\ nm$ the equilibrium film morphology on a substrate with a step change in effective Hamaker constant is a ridge and moat structure.

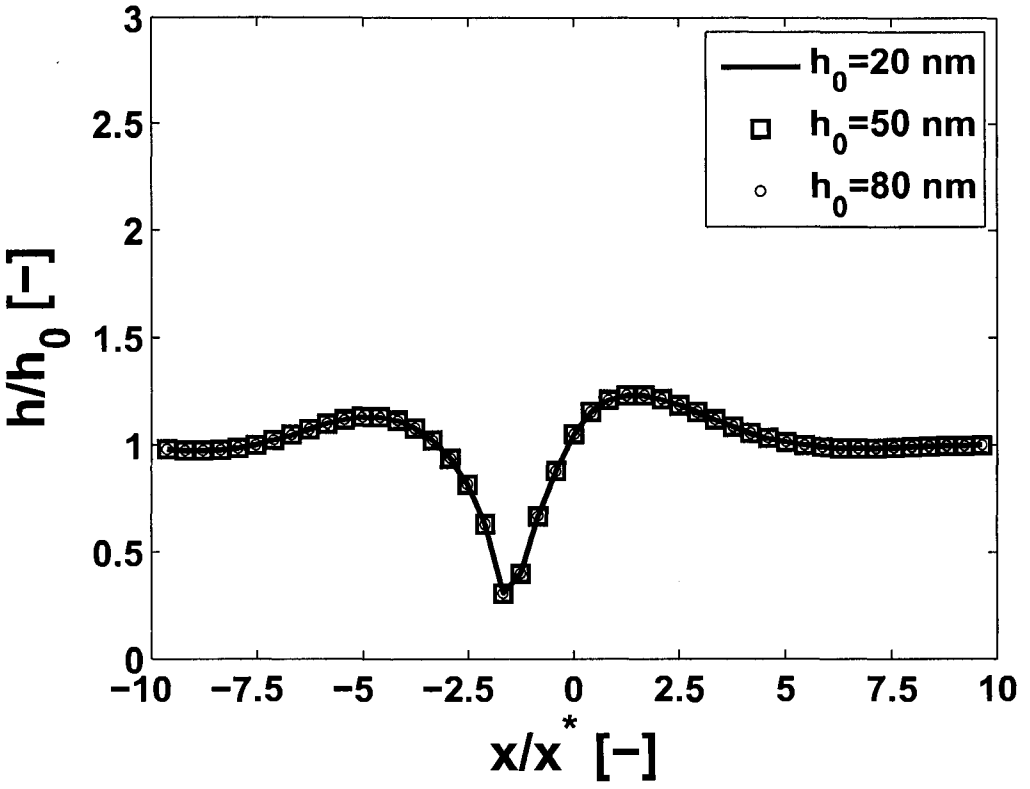

Figure 5.5: Section views of non-dimensional film thickness at ($Y = 0$) at scaled time $t/t^* = 4.55$. Sections taken at the dashed line shown in Figure 5.3c, with the same properties.

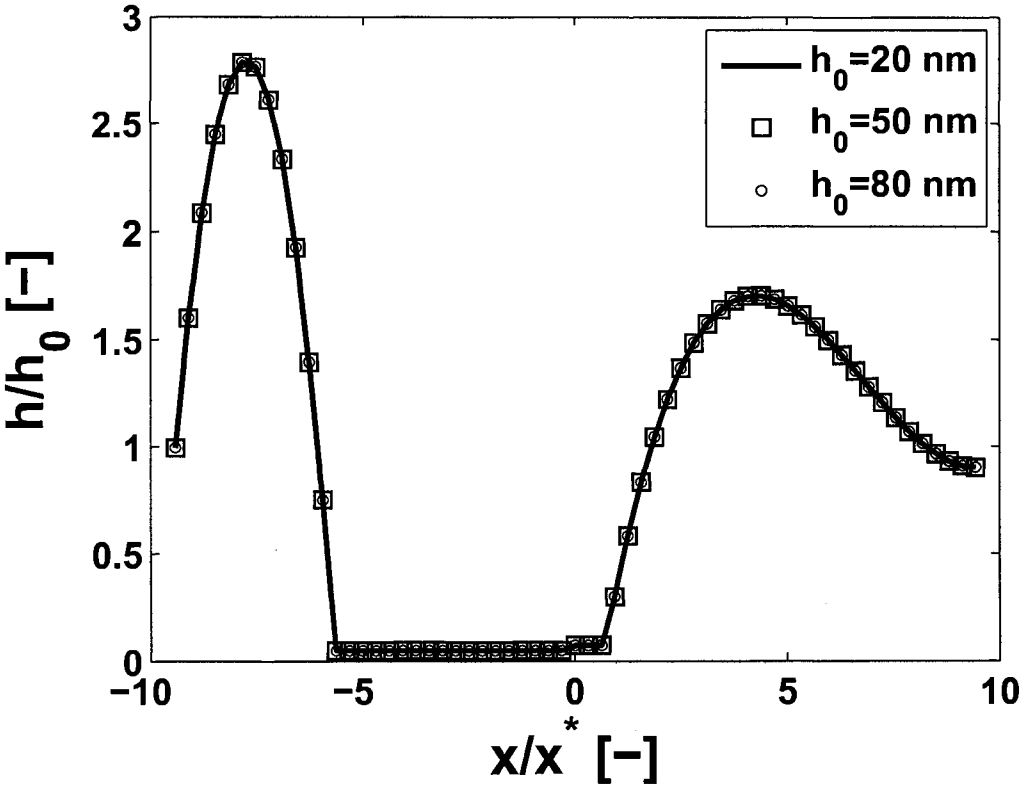

Figure 5.6: Section views of non-dimensional film thickness at $(Y = 0)$ at scaled time $t/t^* = 5.92$. Sections taken at the dashed line shown in Figure 5.3f, with properties as listed.

5.2.2 Influence of the Ratio of Effective Hamaker Constants

As shown in the previous section, a thin liquid film exposed to a step change in the effective Hamaker constant undergos drainage forming a ridge and moat structure. Here, the influence of the magnitude of the ratio of effective Hamaker constants on the drainage induced by a step change is considered. The effective Hamaker constant in the left half domain is fixed at ($A_1 = 1 \times 10^{-19}\ J$) and the value in the right half domain is varied to attain ratios of A_1/A_2 between $0.2 - 1000$. The scaling for all cases considered is calculated using the fixed effective Hamaker constant in the left half domain.

Figure 5.7 shows the maximum non-dimensional film thickness for an initially 20 nm thick film corresponding to different values of the effective Hamaker constant ratio. The film drainage is shown up to the point at which the liquid film first de-wets the lower surface or the first dry spot is formed. The maximum thickness was found by finding the thickest point (z direction) in the (x, y) domain and tracking its evolution. Initially the thickest point is located immediately adjacent to the step change as shown in Figure 5.5, but at later times occurs adjacent to the moat that forms (Figure 5.6). The same final non-dimensional film morphology as observed for the cases shown previously in Figure 5.3 are obtained for the different Hamaker constant ratios. As the ratio of the effective Hamaker constants (A_1/A_2) is increased (*i.e.*, A_2 is decreased), the time taken for the film to de-wet the lower surface and form its final equilibrium configuration decreases. The difference in drainage times for a ratio of $A_1/A_2 = 100$ and $A_1/A_2 = 1000$ is small. For these cases the step change

in effective Hamaker constant has a limiting ratio of 100, above which increasing the ratio will do little to influence film drainage. This is attributed to the fact that the absolute difference in effective Hamaker constant ($A_1 - A_2$) becomes virtually constant after the ratio has been increased above 100. Although the final film morphology is not changed by changing the ratio of effective Hamaker constants in a step change, the film drainage speed is altered.

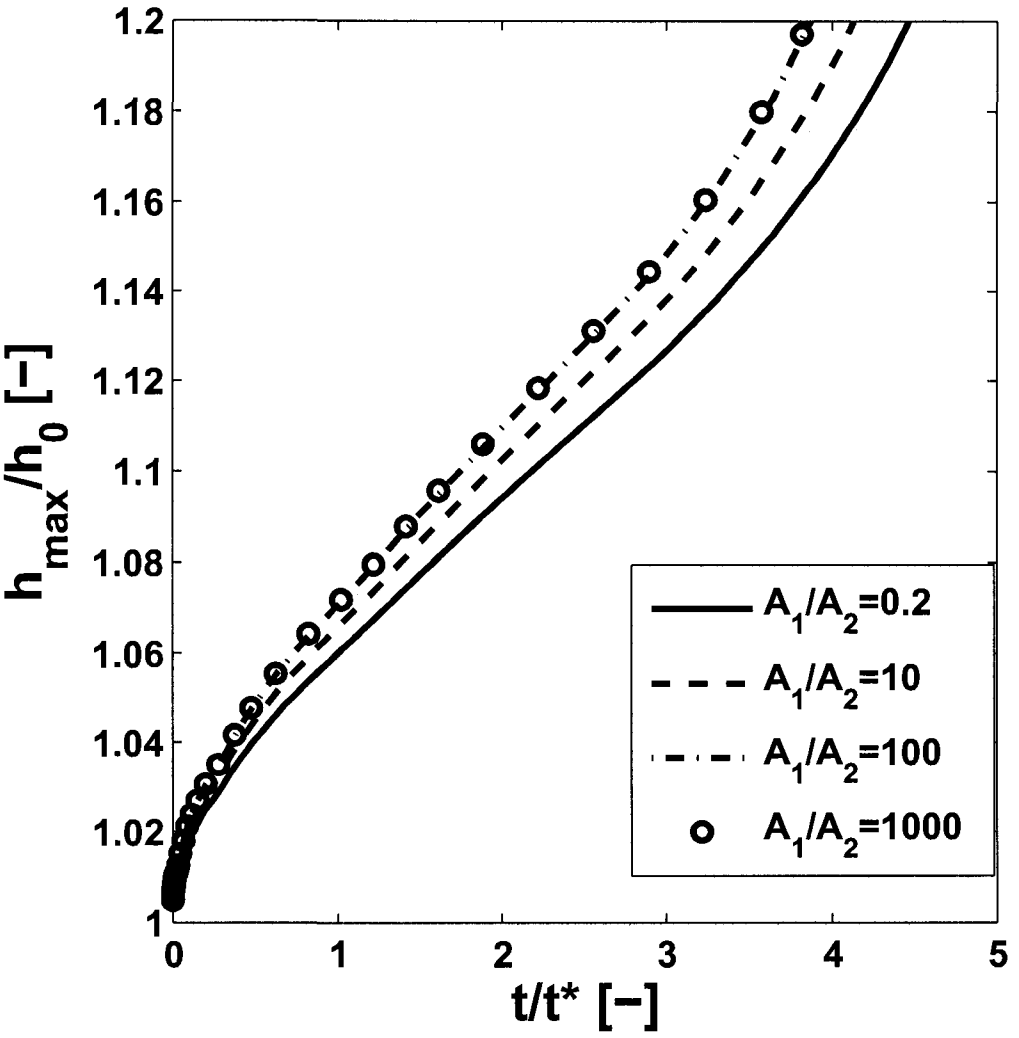

Figure 5.7: Maximum non-dimensional film thickness for a 20 nm thick film subjected to spatial step changes in effective Hamaker constant of different magnitudes. The spacing between upper and lower surface is $d = 100\ nm$, the domain is size $L = 11.46\ \mu m$ and the scaling time is $t^* = 1.44\ s$.

5.2.3 Influence of Film Thickness

In Figures 5.5 and 5.6, it is observed that different initial film thicknesses (h_0) did not yield any difference in the drainage pattern of the film. However, in that case, a fixed overall gap between the upper and lower surfaces (solid planes) bounding the film of $d = 400\ nm$ is used. In this section, the influence of different ratios of d/h_0 on the drainage behaviour is studied.

Figure 5.8 shows the variation of the maximum non-dimensional film thickness with scaled time for different combinations of the initial film thickness, h_0, and the overall gap, d, between the two solid surfaces bounding the film. The step change in chemical heterogeneity in this case is assigned by setting an effective Hamaker constant ratio of $A_1/A_2 = 100$. The maximum film thickness is found by locating the fastest growing location on the film (z direction) in the (x, y) domain and tracking its evolution. As the initial film thickness is varied the domain size and scaling time change. For films of thickness $h_0 = 10, 20, 40, 50, 80\ nm$ the domain sizes are $L =$ 2.92, 11.5, 46.6, 73.0, 187 μm with scaling times $t^* = 0.045,\ 1.44,\ 46.1,\ 141,\ 1.47 \times 10^3\ s$. For a fixed ratio of effective Hamaker constants, the non-dimensional drainage behaviour of a film is independent of the spacing between the upper and lower surfaces (d). The non-dimensional drainage is not influenced by changing the ratio of distance between upper and lower surfaces and initial film thickness up to a minimum of $d/h_0 = 1.25$. This invariance is attributed to the fact that the bounding fluid in the present simulations resembles an inert gas, which induces very little coupling between the fluid dynamics and the interaction between the upper solid surface and

the film-bounding fluid interface.

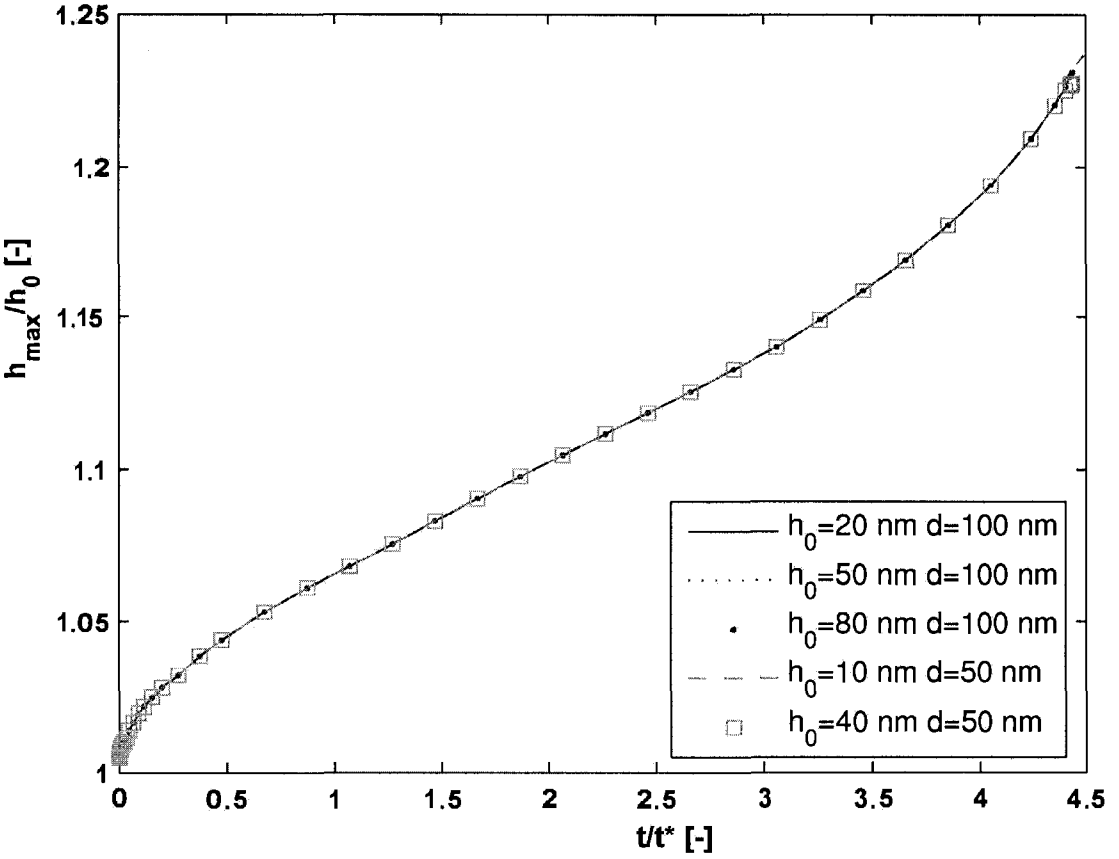

Figure 5.8: Maximum non-dimensional film thickness for films subjected to a spatial step change in effective Hamaker constant with ratio $A_1/A_2 = 100$ for various film thicknesses and spacing between the upper and lower surface. All pertinent parameters are listed in Table 5.1.

Figure 5.9 shows the maximum film thickness of an initially 45 nm thick film in a channel with spacing $d = 50$ nm between the upper and lower solid walls. The supporting (bottom) substrate has a chemical step change, and in the simulations, different effective Hamaker constant ratios are employed to incorporate the influence of different extents of heterogeneity. The maximum film thickness is determined by finding the fastest growing point on the film (z direction) and monitoring its temporal

evolution in the (x, y) domain. The figure shows the drainage behaviour of a film that is initially close to the upper electrode ($d/h_0 = 1.11$). The film evolution is influenced by the upper surface and does not follow the trend seen in films with a higher electrode spacing to thickness ratio ($d/h_0 > 1.25$) shown in Figure 5.8. The film drainage in this case is much slower and damped by the interactions with the upper surface. The slower dynamics are caused by the wetting of the upper surface, which also slows the moat formation and de-wetting of the lower surface.

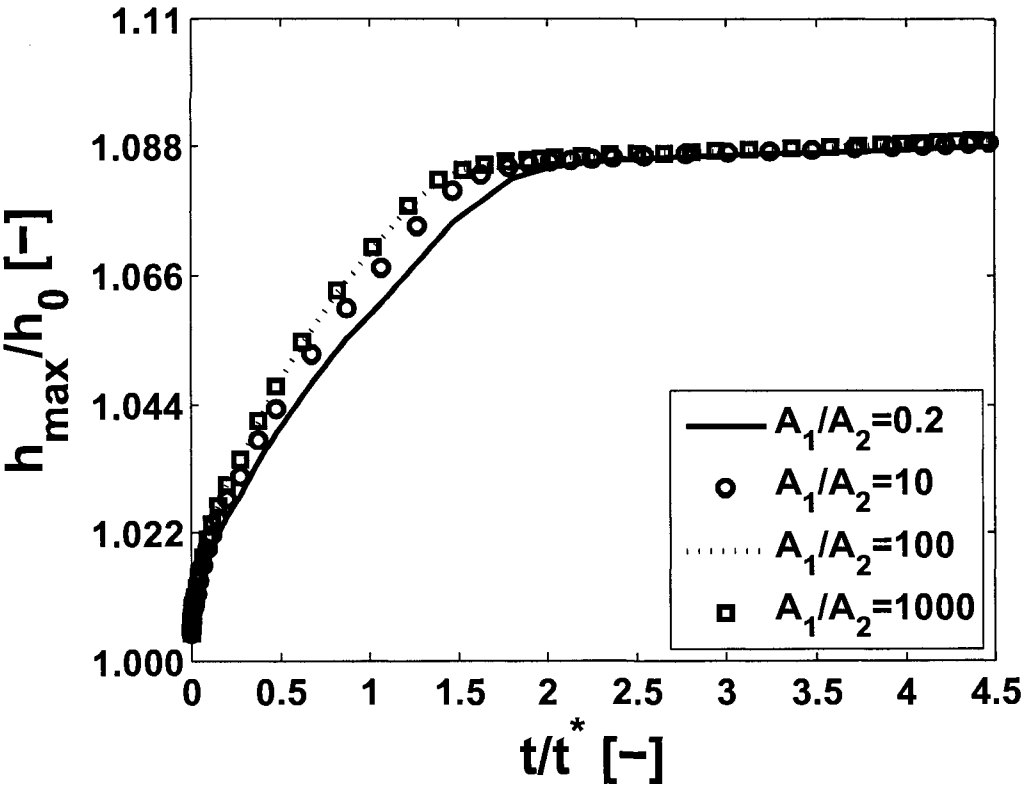

Figure 5.9: The maximum non-dimensional film thickness for an initially $h_0 = 45\ nm$ film in a channel with spacing $d = 50\ nm$ on a chemically stepped surface. The simulations are shown for different effective Hamaker constant ratios. All other pertinent parameters are listed in Table 5.1.

The evolution of a thin film in response to an abrupt step change in chemical

properties was considered by [Kargupta et al., 2000]. The drainage pattern observed for a 12.5 nm thick film was that of a ridge and moat structure which agrees well with the results found in this study. For the cases considered by [Kargupta et al., 2000] otherwise stable films had drainage induced by the application of a chemical step change. Despite this difference, the general drainage behaviour reported is in good agreement with this chapter. The cases presented in this study focus on the influence of step changes in effective Hamaker constant on films that are prone to drainage on homogeneous substrates. This study also includes the influence of an inert upper surface interacting with the films during drainage, while in previous works only free draining films have been observed. When an inert upper surface is considered, film drainage is altered only in cases where the ratio of film thickness to channel spacing is below a cut off value $d/h_0 = 1.25$. The film thickening typically seen on the surface with larger effective Hamaker constant is prevented by the fluid film wetting the upper surface. This interaction delays the film evolution. It would appear that wetting of the upper surface by the liquid film is slower then free deflection of the film interface and thus reduces the rate of film de-wetting by restricting volume conservation.

5.3 Chemically (LVDW) Striped Surfaces

5.3.1 Influence of Stripe Dimensions

In this section film drainage under the influence of periodic striped patterns of effective Hamaker constant will be examined. This is a more complex case then pressure driven thin film drainage on a surface with an abrupt step change in effective Hamaker constant as studied in the previous section. The study of a step change in effective Hamaker constant highlighted the influence of spatial change in the effective Hamaker constant. The step change induced flow patterns that ran parallel to the step change and penetrated deep into the domain. The study of periodic striped patterns of alternating magnitudes of effective Hamaker constant (shown previously in Figure 5.2) allows the study of film dynamics caused by more then one spatial change. By varying the stripe widths (w and w_1 in Figure 5.2) the distance between the spatial changes in effective Hamaker constant change, altering the level of interaction and the resulting flow. The geometry used in the formation of the heterogeneities was discussed previously in section 5.1. All simulations presented are performed on a 60×60 cartesian grid with a domain size of $L = 2\lambda_c$. For previous simulations of the step change in effective Hamaker constant the grid used was 90×90 for the larger domain of $L = 3\lambda_c$, so the same grid spacing of $\lambda_c/30$ was used for all heterogeneities considered.

Figure 5.10 shows the temporal evolution of an initially 20 nm thick film subjected to periodic striping in the effective Hamaker constant. The gray-scale images repre-

sent the film thickness at the noted times and the film thickness can be determined by comparing to the scale-bar on the right of the figure. Figure 5.10a shows the applied pattern and is defined by the periodicity ($L_p = 2\lambda_c$) (center to center distance of the less wettable stripes) and the stripe width ($w = \lambda_c$). Here, λ_c is the length scale predicted from linear theory for a homogeneous surface using $A_1 = 1 \times 10^{-19}$ J. The domain size used is $L = 7.77\ \mu m$ and the scaling time is $t^* = 1.44\ s$. The film drains from an initially small ($\sim$ 1%) random perturbation (not shown), and depressions form along the stripe edges (Figure 5.10b). As the film morphology evolves further (Figure 5.10c – e) the depressions grow along the stripe edges on the more wettable stripes. Figure 5.10f shows the steady state film morphology, with periodic ridges formed on the centers of the stripes with larger effective Hamaker constant.

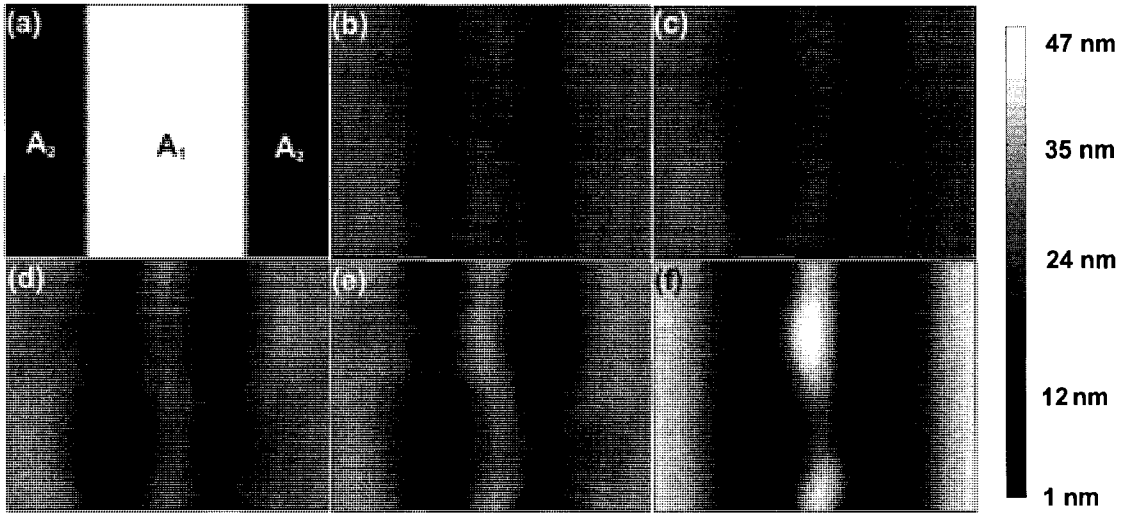

Figure 5.10: Evolution of a 20 nm thick film on a surface with periodically striped effective Hamaker constant. The pattern is defined by periodicity $L_p = 2\lambda_c$ and width $w = \lambda_c$. Panel (a) shows the applied pattern with $A_1 = 1 \times 10^{-19} J$ and $A_2 = 1 \times 10^{-21} J$. Panels (b – f) represent the film thickness using a uniform gray-scale indicated by the scale-bar. The times shown for panels (b – f) are: t = 7.735, 7.789, 8.023, 8.163 and 26.81 s.

Figure 5.11 shows $3D$ plots of the film interface of a 20 nm thick film evolving under the influence of a patterned effective Hamaker constant for the cases shown previously in Figures 5.10b, d and f. The irregularities that occur during the dewetting along stripe edges can be seen in Figure 5.11a. The underlying pattern of effective Hamaker constant is not exactly duplicated in the fluid film. The width (w) of the stripes is larger than the dominant feature length, thus more than one structure is formed per stripe. The individual stripe edges induce depressions in the film that are initially independent of one another. This results in some fluid being trapped in the center of the more wettable stripe, which eventually forms an irregular ridge.

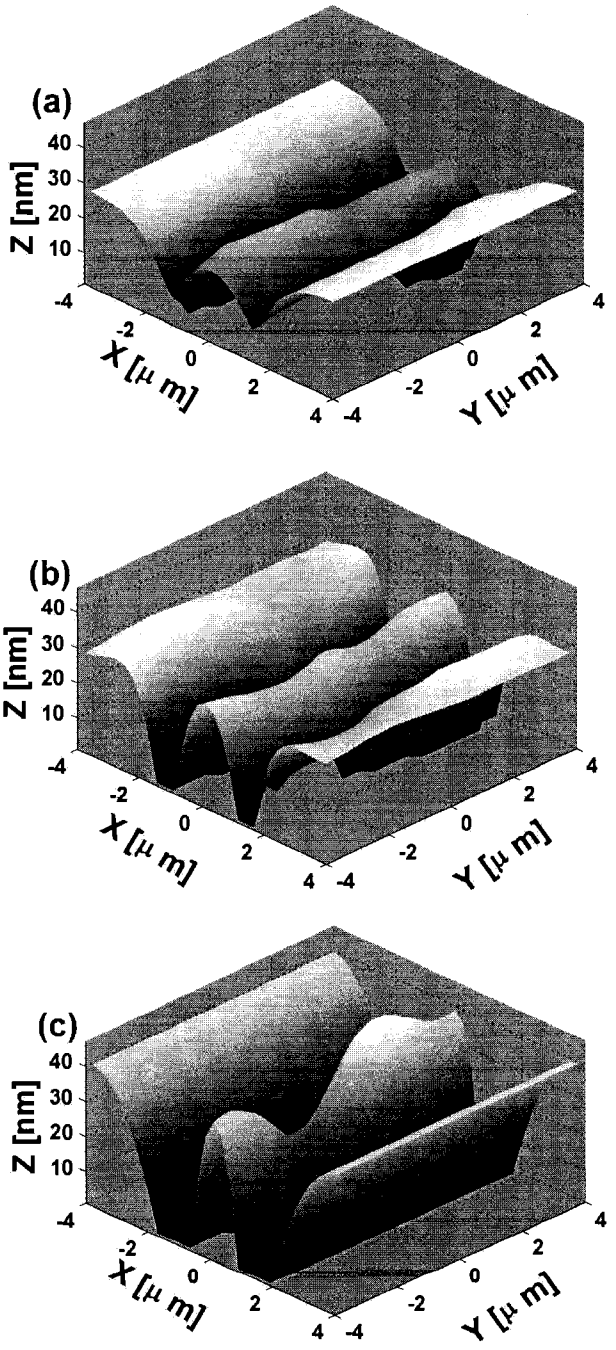

Figure 5.11: Evolution of a 20 nm thick film on a surface with periodically striped effective Hamaker constant. The cases shown were previously shown in Figure 5.10b, d and f (a – c of current figure).

Figure 5.12 shows the evolution of an initially 20 nm film exposed to periodic striping of the effective Hamaker constant, spatial x frequency of the periodicity being smaller than shown previously. Figure 5.12a shows the patterning of the effective Hamaker constant where $A_1 = 1 \times 10^{-19}$ J and $A_2 = 1 \times 10^{-21}$ J. The pattern is defined by a periodicity of $L_p = \lambda_c$ and stripe width $w = \lambda_c/2$. Figures 5.12b – f show gray-scale images indicating the film thickness as it evolves in time. The film drains from an initially small random perturbation (not shown) and forms depressions at the center of the stripes with higher effective Hamaker constant (Figure 5.12b). As the film drains, the depressions drain completely and expand over the stripes (Figure 5.12c – e). Figure 5.12f shows the steady state film morphology, where the applied pattern in effective Hamaker constant has been closely replicated by the fluid film. The steady state morphology of the film can also be seen in the $3D$ reproduction of Figure 5.12f in Figure 5.13.

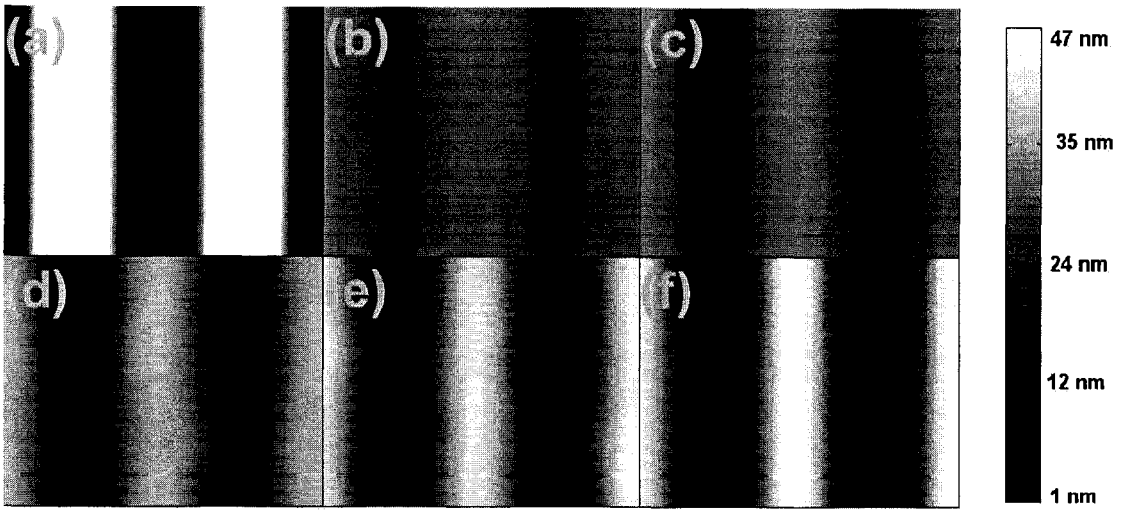

Figure 5.12: Evolution of a 20 nm thick film on a surface with periodically striped effective Hamaker constant. The pattern is defined by periodicity $L_p = \lambda_c$ and width $w = \lambda_c/2$. Panel (a) shows the applied pattern with $A_1 = 1 \times 10^{-19} J$ and $A_2 = 1 \times 10^{-21} J$. Panels (b – f) represent the film thickness using a uniform gray-scale indicated by the scale-bar. The times shown for panels (b – f) are: $t = 3.647, 3.842, 3.977, 4.284$ and 7.200 s.

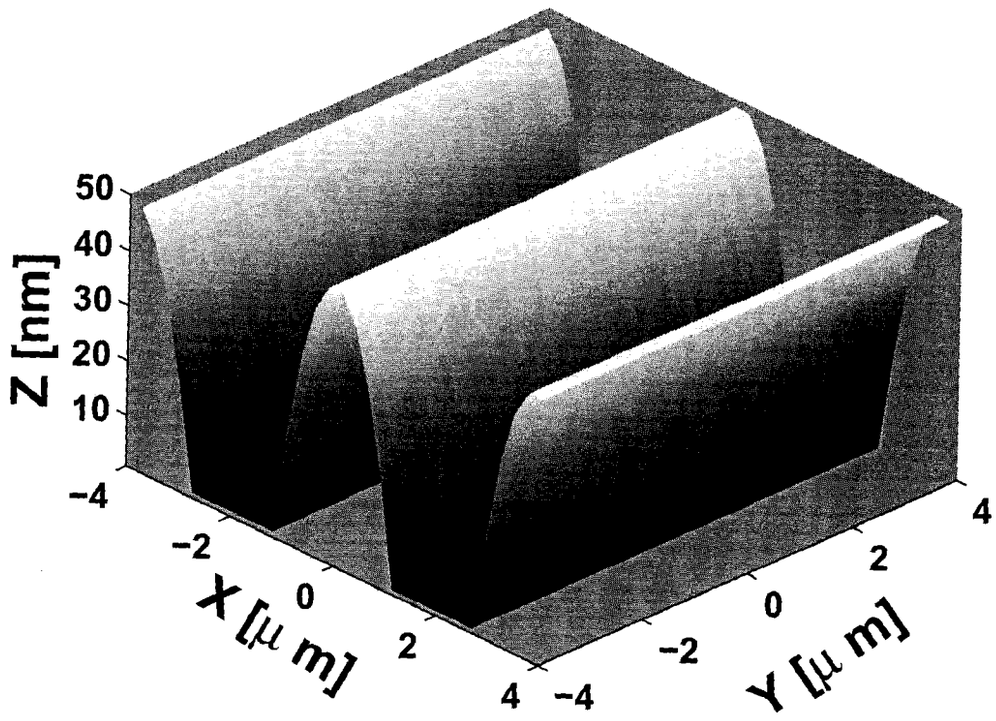

Figure 5.13: Steady state film morphology of a 20 nm thick film on a surface with periodically striped effective Hamaker constant. This case was previously shown in Figure 5.12f.

Figure 5.14 shows the evolution of an initially 20 nm film exposed to periodic striping of the effective Hamaker constant of a high spatial x frequency. Figure 5.14a shows the patterning of the effective Hamaker constant; a periodicity of $L_p = \lambda_c/2$ and stripe width $w = \lambda_c/4$ define the pattern. Figure 5.14a is independent of the scale-bar shown on the right of the figure. Figure 5.14b $-$ f show gray-scale images indicating the film thickness at the times noted. The film evolves from an initial random perturbation (not shown) to form depressions on two of the stripes with higher effective Hamaker constant (Figure 5.14b). The depressions grow and form holes (Figure 5.14c). The holes grow and combine to form trenches (Figure 5.14d and e). At steady state the trenches occupy the entire width of the stripes they are formed on and enclose a larger ridge (Figure 5.14f). The steady state film morphology shown in Figure 5.14f is reproduced in $3D$ in Figure 5.15. The $3D$ rendering shows that small dimples form along a smaller secondary ridge that forms between the two de-wet areas along the larger ridge. The large central ridge is very uniform but the smaller ridge has two small columnar structures on it. The features of the pattern have become too small for each stripe to act as a de-wetting site. Instead the film selectively de-wets at locations that are separated by a distance of approximately λ_c.

Comparing the drainage of a 20 nm thick film of the three previous cases for patterns with periodicity $L_p = 2\lambda_c, \lambda_c, \lambda_c/2$ and width $w = \lambda_c, \lambda_c/2, \lambda_c/4$, several observations can be made. The pattern defined by $L_p = \lambda_c, w = \lambda_c/2$ generated the best pattern replication by the drained film. The pattern replication desired is the uniform de-wetting of the liquid film from the stripes of higher effective Hamaker

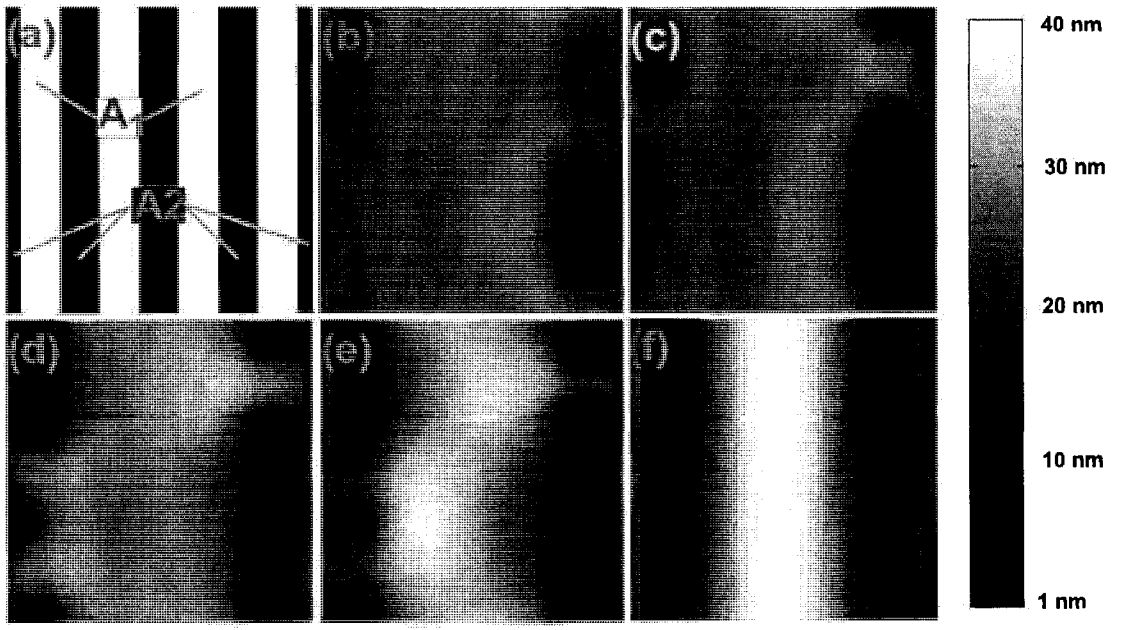

Figure 5.14: Film evolution of a 20 nm thick film on a chemically striped surface with stripe periodicity $L_p = \lambda_c/2$ and width $w = \lambda_c/4$. Panel (a) shows the applied pattern with $A_1 = 1 \times 10^{-19} J$ shown as white and $A_2 = 1 \times 10^{-21} J$ shown as black. Panels (b – f) represent the film thickness taken at times $t =$ 18.44, 19.40, 20.67, 21.96 and 54.60 s. The gray-scale that represents the film thickness can be seen in the scale-bar on the right of the figure.

constant. The other two cases failed to replicate the underlying chemical pattern. When $L_p = 2\lambda_c$, the stripes are too wide and intermediate structures occur at the center of the stripes with higher effective Hamaker constant. The stripe widths are too narrow when $L_p = \lambda_c/2$ and de-wetting only occurs randomly at some of the potential locations. The film drainage occurs fastest when good pattern replication is observed. The times to steady state were $t = 26.8,\ 7.20,\ 54.6\ s$ for periodicity $L_p = 2\lambda_c, \lambda_c, \lambda_c/2$. The film was considered in steady state when equation (3.73), reached a value that changed $< 10^{-10}$ between time steps. When the periodicity was $L_p = \lambda_c$, the final structure was attained more rapidly and showed more order then the other cases considered. The other two cases ($L_p = 2\lambda_c,\ \lambda_c/2$) took more time to

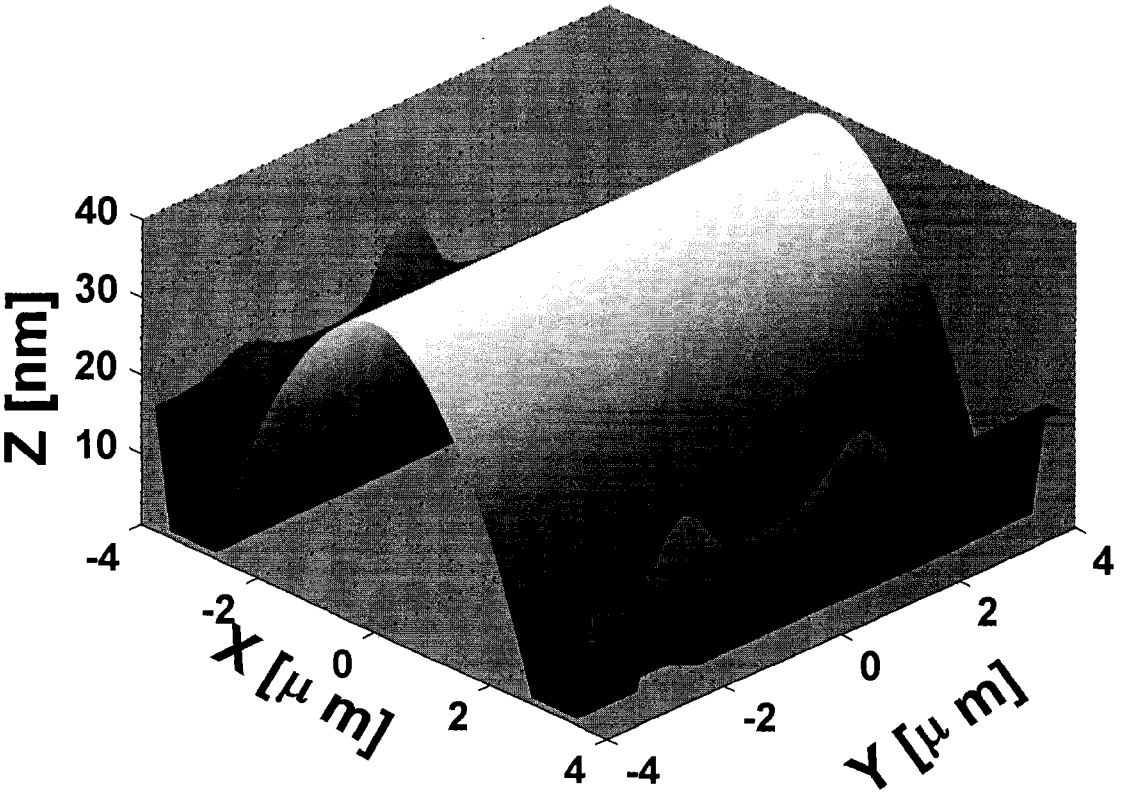

Figure 5.15: Steady state film morphology of a 20 nm thick film on a surface with periodically striped effective Hamaker constant. This case was previously shown in Figure 5.14f.

reach pseudo stationary states and had less ordered final interfacial configurations.

The three cases presented above are very similar to cases shown by [Kargupta and Sharma, 2001]. Despite a more sophisticated formulation of the conjoining/disjoining pressure in [Kargupta and Sharma, 2001] then the method used here, excellent agreement based on the pattern replication results shown in Figure 5.10 – 5.14 are obtained. They report that a film draining on a chemically patterned surface defined by $L_p = \lambda_c$, $w = \lambda_c/2$ will de-wet less wettable (higher effective Hamaker constant) stripes producing dry patches on the higher effective Hamaker constant stripes and ridges on the stripes of lower effective Hamaker constant, the results shown in Figure

5.10 are in good agreement with these. The case of stripes defined by $L_p = 2\lambda_c$ and $w = \lambda_c$ is also considered. Again the results are in good agreement with the current study, they predict that two distinct drainage locations will occur on stripes of higher effective Hamaker constant with ridges forming on lower effective Hamaker constant stripes. [Kargupta and Sharma, 2001] predict that a case of period $\lambda_c/2$, $w = \lambda_c/4$ will selectively de-wet at locations that are approximately λ_c apart. These results are replicated in the simulation shown in Figure 5.14. In the work of [Kargupta and Sharma, 2001], an interval for chemical patterning is described where the width of stripes must fall between $\lambda_{up} > w > \lambda_{low}$, where λ_{up}, λ_{low} provide upper and lower limits on stripe width that produces good pattern replication in the film. For the case of stripes of uniform width, the pattern limit is within the interval $\lambda_c > w > \lambda_c/3$.

The experimental works of [Rockford et al., 1999, Sehgal et al., 2002] show qualitative agreement with the results produced in the present study. In [Rockford et al., 1999] chemical striping is observed to reduce the size of structure formation as compared to drainage on a homogeneous substrate. This phenomena is evident in the induced drainage on patterns below λ_c witnessed in Figures 5.12 – 5.14. In these cases the film drainage occurs on length scales of a quarter of that predicted by linear theory. The experimental work of [Sehgal et al., 2002] the transitions that are observed in pattern replication are shown by comparing AFM results for a polymer blend subjected to striped patterns of varying width and frequency. As the frequency and width of the pattern is reduced the transition shown in Figure 5.12 to Figure 5.14 is observed. The general qualitative film behaviour is confirmed, although ex-

act confirmation could not be performed since the chemical properties of the films studied experimentally are not given. Next, the study of periodic stripes is extended by examining the time taken to reach pseudo steady state, the area of de-wet lower surface and other properties of drainage are considered.

Figure 5.16 shows the percent area of the de-wet lower substrate at steady state and the time taken for the initial film drainage as a function of the stripe width. The results are obtained for an initially 20 nm film subjected to a striping of effective Hamaker constant with period $L_p = 2\lambda_c$. The percent area de-wet is calculated by locating the area on the lower surface that was completely de-wet by the liquid film and dividing it by the total domain area in the (x, y) plane. The time taken for the first instance of the liquid film de-wetting the lower surface (initial drainage time) is found by tracking the film drainage until the first instance of complete de-wetting of the lower surface is observed. The initial drainage time is typically a good relative indicator of the time required to reach steady state. Figure 5.17 shows the maximum and minimum film thickness for the 20 nm film previously shown in Figure 5.12. Figure 5.17 shows typical initial drainage and steady state drainage times for a film draining on a patterned surface. The rippling of the curve for maximum film thickness is caused by the interaction of small structures that join to form larger structures creating minor thickness fluctuations. During the overshoot that occurs before steady state the final structures gain uniformity as the film interface becomes uniform as shown perviously in Figures 5.12 and 5.13. Based on the three cases discussed previously, the time to initial drainage takes at least half the total drainage

time. Thus the time to initial de-wetting of the lower surface by the liquid film is a good indicator of relative times taken to reach pseudo steady state configurations.

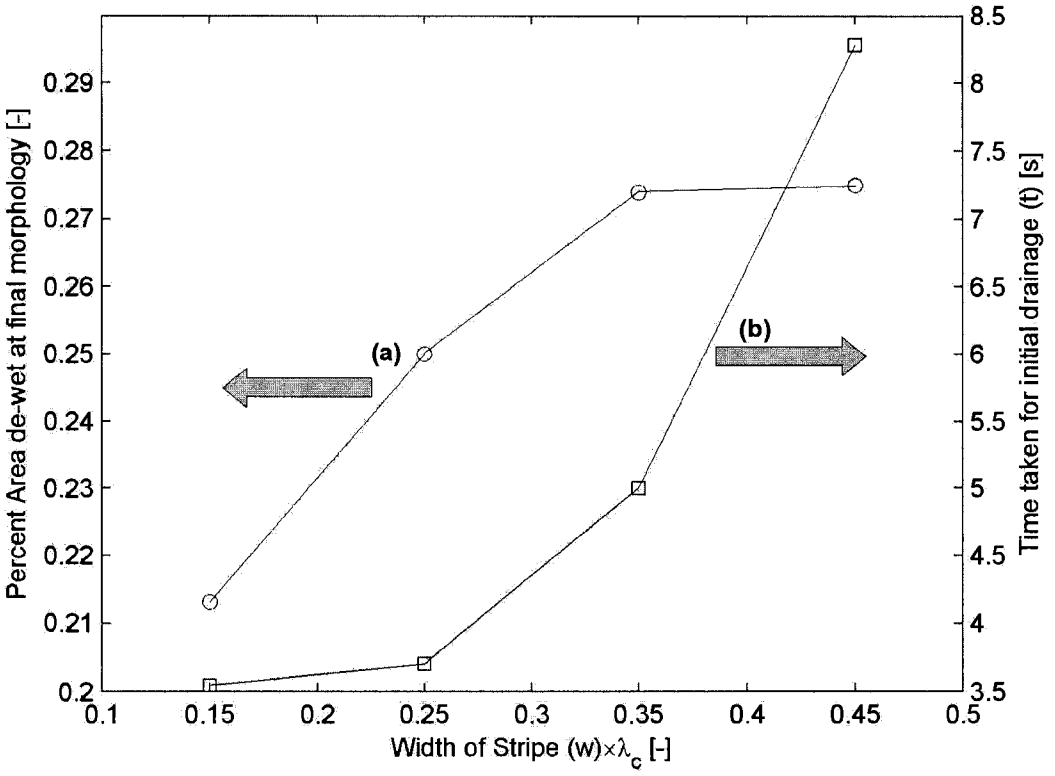

Figure 5.16: Percent area of the domain de-wet at final morphology and time taken for initial film drainage to occur for patterns of the effective Hamaker constant with periodicity $L_p = 2\lambda_c$. Line (a) with the circular markers, shows the percent area de-wet and references to the left axis. Line (b) with the square markers, shows the time taken for drainage and references to the right axis.

In Figure 5.16, as the stripe width is decreased from $0.5 - 0.15$, the time required for initial film drainage decreases. Decreasing the stripe width below $w = 0.15\lambda_c$ does not significantly change the time required for the initial drainage. A gradient in conjoining/disjoining pressure occurs over the edge of a stripe and as the stripe width is reduced, the influence of the two adjacent edges is combined to produce

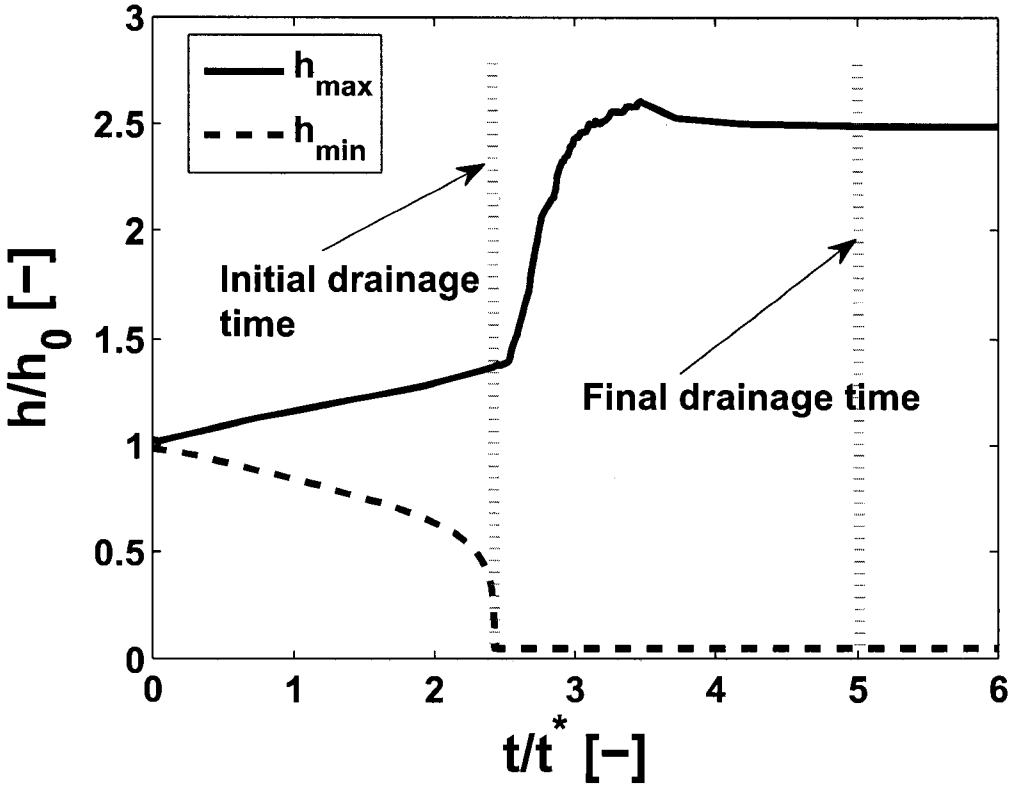

Figure 5.17: Temporal evolution of a 20 nm film influenced by a patterned effective Hamaker constant with periodicity $L_p = \lambda_c$ and width $w = \lambda_c/2$. This case was previously shown in Figure 5.12.

faster drainage. The area de-wet during drainage increases with increasing stripe width until it reaches a maximum at stripes of width $0.35\lambda_c$. If a striped pattern is considered optimum when the area of higher effective Hamaker constant complete de-wets at steady state, the optimum stripe width is $0.25\lambda_c$, which produces good pattern replication with 25% of the total area de-wetting.

Figure 5.18 shows $(x - z)$ section views (at mid plane $y = 0$) of an initially 20 nm thick film evolving in time for a ratio of effective Hamaker constants $A_1/A_2 = 100$. The darker line at the base of the plot indicates the location of the stripe with

larger effective Hamaker constant (A_1), and the lighter line at the base of the plot indicates the stripes of smaller effective Hamaker constant (A_2). The film drains from an initial random perturbation (not shown) and is immediately influenced by the high Hamaker constant (more wettable) region of the patterned substrate, which causes the formation of a depression in the film. The depression grows to completely drain the liquid film from the lower surface. The drained region expands until it occupies the entire area of the stripe with larger effective Hamaker constant. For a stripe periodicity of $L_p = 2\lambda_c$, and stripe width $w = 0.25\lambda_c$ the pattern replication is virtually perfect in terms of area de-wet.

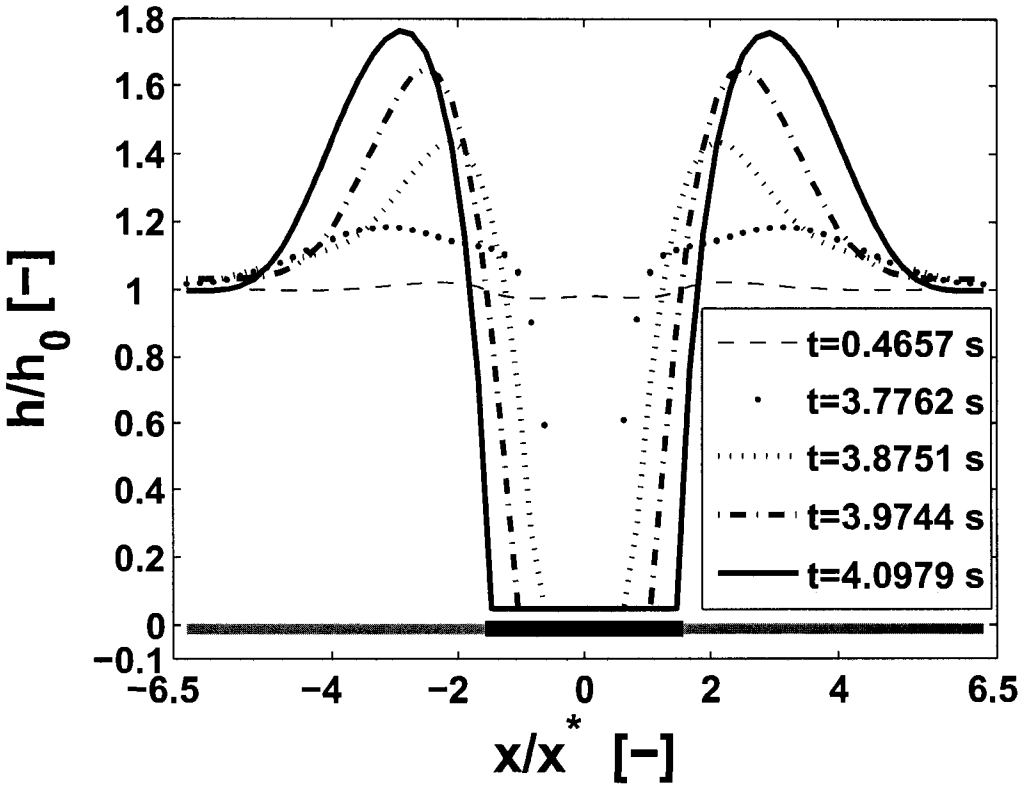

Figure 5.18: Section views (at $y = 0$) of the drainage of a 20 nm thick film on a surface with striping of the effective Hamaker constant with width $w = 0.25\lambda_c$ and periodicity $L_p = 2\lambda_c$. The ratio of effective Hamaker constants used is $A_1/A_2 = 100$, the spacing between upper and lower surfaces is $d = 100$ nm, the scaling time is $t^* = 1.44$ and the domain size is $L = 7.77$ μm. The black line at the bottom indicates the region of larger effective Hamaker constant (A_1) and the gray line indicates the region of lower effective Hamaker constant (A_2)

5.3.2 Influence of Film Thickness

Figure 5.19 shows the maximum non-dimensional film thickness evolving in time on a surface with striping of the effective Hamaker constant with period $L_p = 2\lambda_c$ and stripe width $w = \lambda_c/2$. The maximum film thickness is found by identifying the fastest thickening location of the film and tracking its evolution. Figure 5.19 shows that the initial film thickness does not significantly influence film drainage until the film interacts with the upper surface. When the film begins to wet the upper surface, drainage is slowed due to conservation of volume. For a film of thickness $h_0 = 90\ nm$, here the thin film is draining in a cavity with a spacing $d = 100\ nm$ and the film interacts with the upper surface at $t \simeq 2\ s$. As the film thickens, the upper bounding fluid de-wets the upper surface as the fluid wets it. The wetting of the upper surface, by the liquid film, slows the time to de-wet the liquid film from the lower surface. The wetting of the upper surface, by the liquid film, makes it more difficult for film to thicken enough for the film to completely de-wet the lower surface.

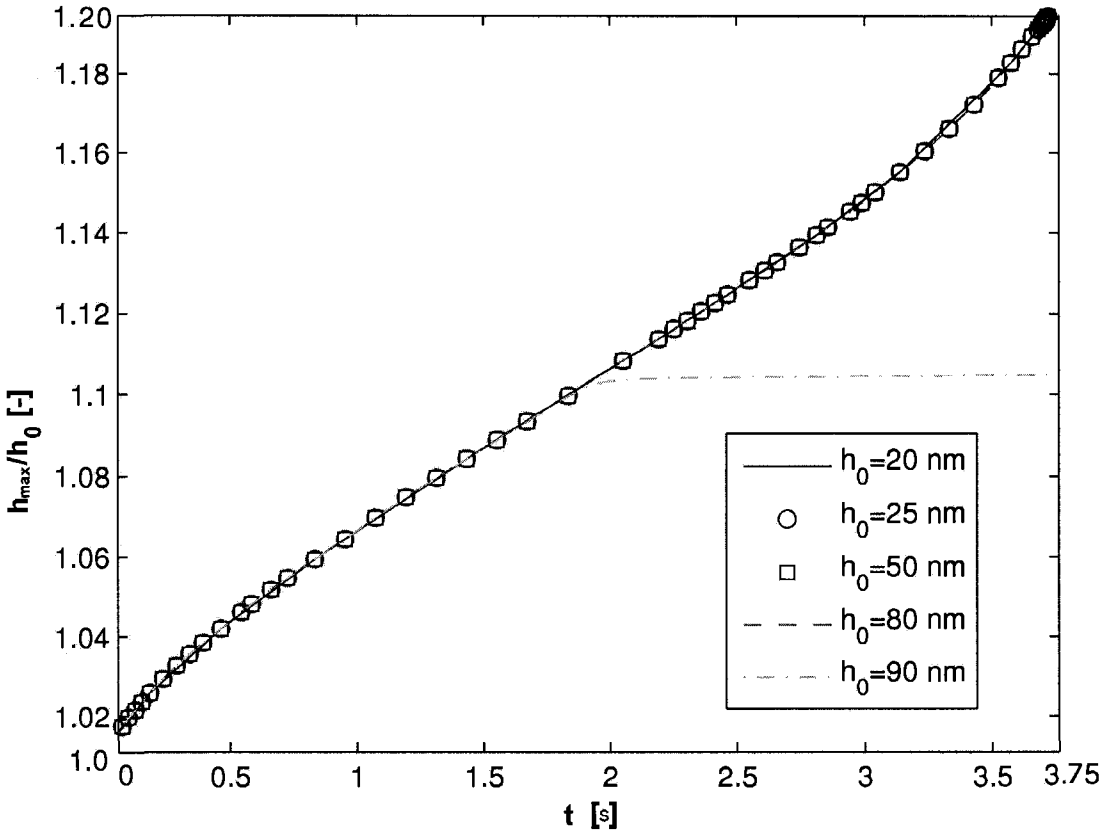

Figure 5.19: Maximum non-dimensional film thickness evolving in time on a patterned surface with a ratio of effective Hamaker constants $A_1/A_2 = 100$ with $L_p = 2\ \lambda_c$ and $w = \lambda_c/2$. The spacing between upper and lower surfaces is $d = 100\ nm$.

5.4 Chemical (LVDW) Patterning with Homogeneous Electric Field

The spontaneous (pressure driven) drainage of a thin liquid film on a surface that has an abrupt spatial step change in effective Hamaker constant was discussed previously in section 5.2. The film is influenced by the gradient of conjoining/disjoining pressure that exists across the step change and drains to form a ridge and moat structure. This is different from the equilibrium drained structures (dry spots or holes) formed on a homogeneous substrate under pressure based drainage, as shown in Chapter 4. However, in Chapter 4, it was also observed that application of a uniform electric field induces different types of drainage patterns on homogeneous substrates. In this section, the combination of a homogeneous electric field and a surface with a step change in effective Hamaker constant on the film drainage is considered.

Figure 5.20 shows the steady state film morphologies for an initially 20 nm thick film draining under the influence of an abrupt spatial step change in effective Hamaker constant ($A_1/A_2 = 10$) and a homogeneously applied electric field. The simulations are carried out on a 90×90 cartesian grid with $L = 3\lambda_c$. The dominant wave length is found from linear theory for film drainage due to a uniform Hamaker constant of $A_1 = 1 \times 10^{-19}\ J$ and results in a domain of side length $L = 11.46\ \mu m$. The applied electric field is increased moving from Figure 5.20a – Figure 5.20d by the application of increasing applied potentials $\psi_{low} = 1,\ 2.5,\ 5,\ 10\ V$ (the resulting electric fields are $E_p = 4.546,\ 11.36,\ 27.72, 45.46\ MV/m$), while the upper solid surface was grounded. As the applied electric field is increased, the time required for drainage decreases. The morphology also changes. When a low electric field is applied, a single depression

forms, but as the magnitude of the applied field is increased the ridges that form at the edge of the depression grow and induce secondary depressions along their periphery.

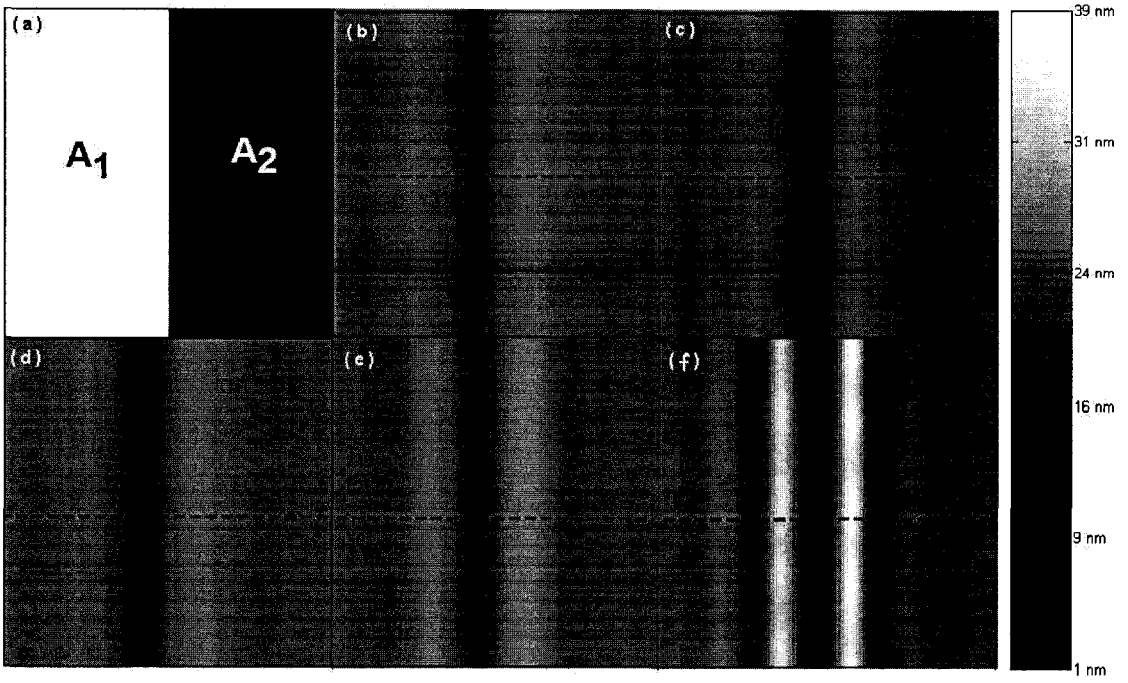

Figure 5.20: Comparison of film drainage for a 20 nm thick film under the influence of a step change in effective Hamaker constants ($A_1/A_2 = 10$) and homogeneous electric fields. Panel (a) shows the effective Hamaker constant distribution in the domain. The applied fields starting in the panel (b) and moving to panel (f): $E_p = 0, 4.546,\ 11.36,\ 27.72,\ 45.46\ MV/m$. The times shown in panels (b − f) are: $t = 4834,\ 4834,\ 3977,\ 2251,\ 711.0\ s$. The domain size for all cases is $L = 11.64\ \mu m$. All other relevant parameters are listed in Table 5.1.

Figure 5.21 shows section views of an initially 20 nm thick film draining on a surface with an abrupt spatial step change in effective Hamaker constant in the presence of a homogeneous applied electric field. The sections were obtained by taking the film thickness along the dashed lines shown in Figure 5.20. The changing scale of the structures forming in the film can be seen by comparing the films as different magnitudes of applied fields are applied. As the field is increased, the decreasing size

of the dominant features is evident, and the size of the individual features decreases. In the case of the largest applied field, the lowest point is beginning to separate into two different features. Thus, a kink in the film is formed near its lowest point. As the features become smaller in cross section (x, y) directions they grow in the z direction conserving volume, this can be seen by the increasing maximum thickness of structures that occurs as the applied field magnitude is increased.

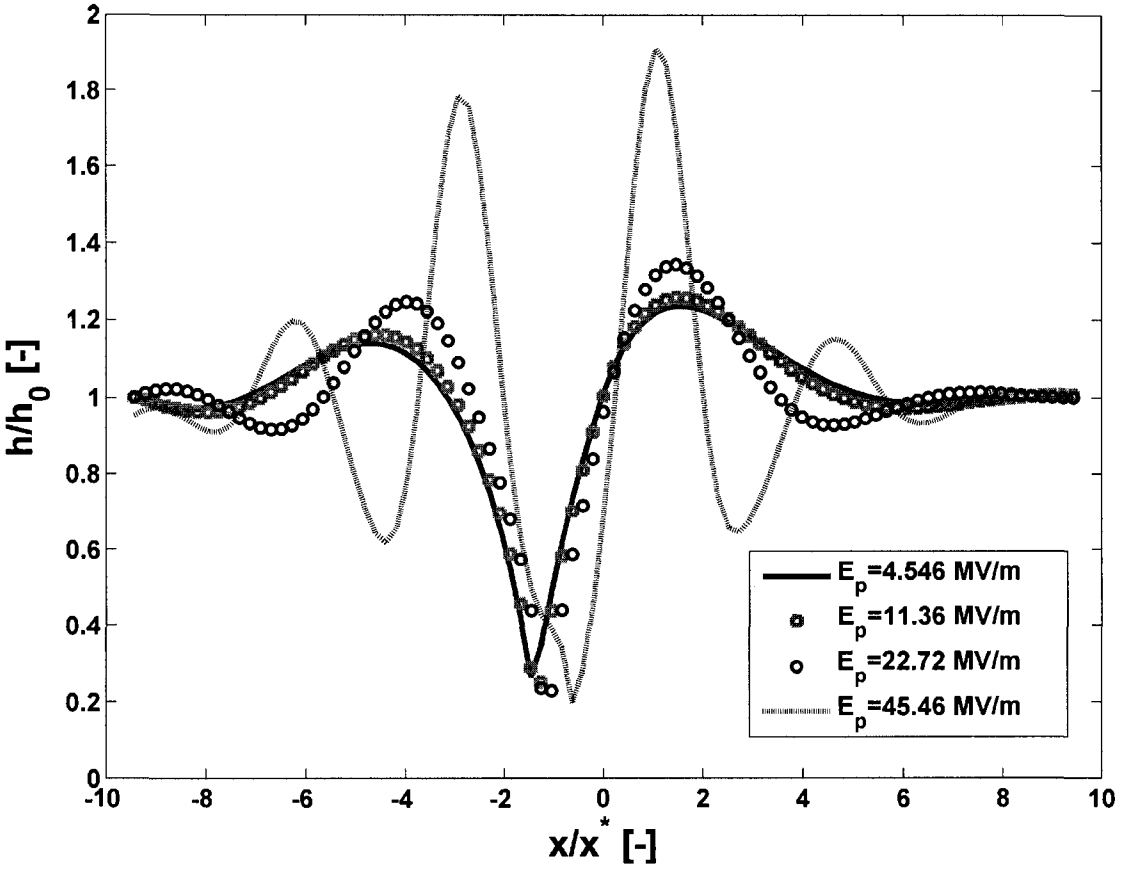

Figure 5.21: Comparison of mid-plane ($y = 0$) cross sections of film thickness for a step change in effective Hamaker constants ($A_1/A_2 = 10$) and various magnitudes of applied uniform electric field. These cases were previously shown in Figure 5.20, and the location of the sections are indicated by the dashed lines.

5.5 Concluding Remarks

The influence of chemical patterning through spatially varying effective Hamaker constant is investigated. Step changes in effective Hamaker constant are considered first. The film drainage results show good agreement with the drainage reported by [Kargupta et al., 2000] for numerical simulation of a similar film. The inert upper surface included in the model is an extension of the published work. When the film drainage results in the liquid film interacting with the upper surface the speed of drainage is slowed. The ratio of effective Hamaker constants does not alter the final film configuration but does influence film drainage speed. After the ratios of effective Hamaker constant reach $A_1/A_2 > 100$ no significant differences in drainage speed are observed.

The case of periodic striping in effective Hamaker constant is considered. The model is qualitatively validated using the experimental work of [Rockford et al., 1999] and [Sehgal et al., 2002]. The results show excellent agreement with the numerical results of [Kargupta and Sharma, 2001], providing quantitative validation. The current study examines how the time to drainage and area of the lower surface de-wet by the liquid films are influenced by changing stripe properties. For striped patterns with a constant period of $2\lambda_c$, the amount of de-wetting reaches a of peak around 33% of the surface for a 20 nm thick film. The drainage time decreases as width increases but is essentially constant once the width of the stripe with smaller effective Hamaker constant falls below $\sim 0.2\lambda_c$.

The influence of a homogeneous applied electric field on the drainage induced by a

step change in effective Hamaker constant is examined. A homogeneous electric field applied at sufficient strength $E_p > 12\ MV/m$, alters the film drainage. The resulting size of structures formed is reduced and the maximum final thickness is increased. The time taken for drainage is reduced as the magnitude of the applied electric field is increased. This case demonstrates the utility of combining chemical patterning with an electric field and provides a justification for the final chapter, where electric and chemical patterning are used concurrently.

Chapter 6

Thin Film Drainage under Electrical Heterogeneity

The drainage of thin liquid films between two electrically and chemically homogeneous substrates was examined in Chapter 4. In this chapter, the drainage of a thin liquid film under the influence of a heterogeneously applied electric field is studied. Drainage on a heterogeneous surface occurs due to spatial gradients in the conjoining/disjoining pressure created by the heterogeneity. Heterogeneities in applied electric field are presented in this chapter, heterogeneities of effective Hamaker constant (chemical heterogeneity) were previously discussed in Chapter 5, and a combination of these are considered in Chapter 7.

The film drainage induced by heterogeneity in the applied electric field is studied by numerically solving the thin film equation (3.35) with spatially variable electrode spacing, $d = d(x, y)$. Similar to the treatment of chemical heterogeneity, the influence of spatially varying electric fields on film drainage is studied for two situations, namely, when the field changes in a stepwise manner, and when the field changes periodically.

As stated earlier, the electrode spacing is varied in a periodic manner by using a comb-like surface of the upper plate bounding the film. The simulations are performed on a 90×90 cartesian grid for step changes (due to the larger domains considered) and 60×60 cartesian grids for more complex patterns with scaling based on linear theory for homogeneous electrostatic drainage (equations 3.60).

6.1 Electric Field Heterogeneity

The study of thin film drainage under the influence of electrostatic patterning, first considers a spatial step change in the applied electric field. The electric field (E_p) at the film interface, previously written as equation (3.55), is varied spatially by either changing the applied electric potential or electrode spacing. The changes in electric field are created using spatially varying electrode spacing $d = d(x, y)$, with constant applied electric potential difference between the upper and lower solid surfaces (electrodes). The applied potential could also be spatially varied to create changes in the electric field (with uniform electrode spacing), but in this study, variable electrode spacing is used predominantly to produce electric field patterning. The study of electrical heterogeneity will be performed with uniform LVDW interactions over the domain.

Figure 6.1 schematically depicts the thin film system under the influence of an abrupt spatial step change in the applied electric field. The step change in electric field is created by having different electrode spacings in the two half domains while uniform potentials are applied on the upper and lower surfaces. The (x, y) plane view

of the electrode patterning can be seen in Figure 6.1a. The (x, z) plane view, Figure 6.1b, shows the electrode spacing, $d = d(x)$, relative to the initial film thickness (h_0). The left half domain has a length L_{x1} and electrode spacing d_1 and the right half domain has a length L_{x2} and an electrode spacing of d_2. The left half domain has a larger applied field then the right half domain due to the smaller spacing between the electrodes $(d_1 < d_2)$. A square domain of length $L = 6\lambda_c$ is used in the simulations presented. The scaling length was found using the smaller electrode spacing (d_1) in equation (3.61), since the larger applied field will produce smaller structures during film drainage. The domain size was selected to ensure that the applied boundary conditions do not artificially influence the film drainage.

Figure 6.2 schematically shows the thin film system under the influence of spatially periodic striping of an applied electric field. The stripes of larger electrode spacing (d_2) will have smaller electric fields, while the stripes with smaller electrode spacing (d_1) will create larger electric fields. The (x, y) plane view of the electrode patterning can be seen in Figure 6.2a. The (x, z) plane view, Figure 6.2b, shows the electrode spacing relative to the initial film thickness (h_0). The stripes with the smaller electrode spacing have width w_1 and the stripes of larger electrode spacing have width w. The stripes have a periodicity or center to center distance of L_p, which is related to the stripe widths by $L_p = w + w_1$. The striped patterns are defined by the periodicity (L_p) and width of the stripe with smaller applied field (w). The stripes are modeled on a square domain of side length $L = 2\lambda_c$. The scaling length (λ_c), is taken from equation (3.61) and uses the smaller electrode spacing to define

the dominant wave length.

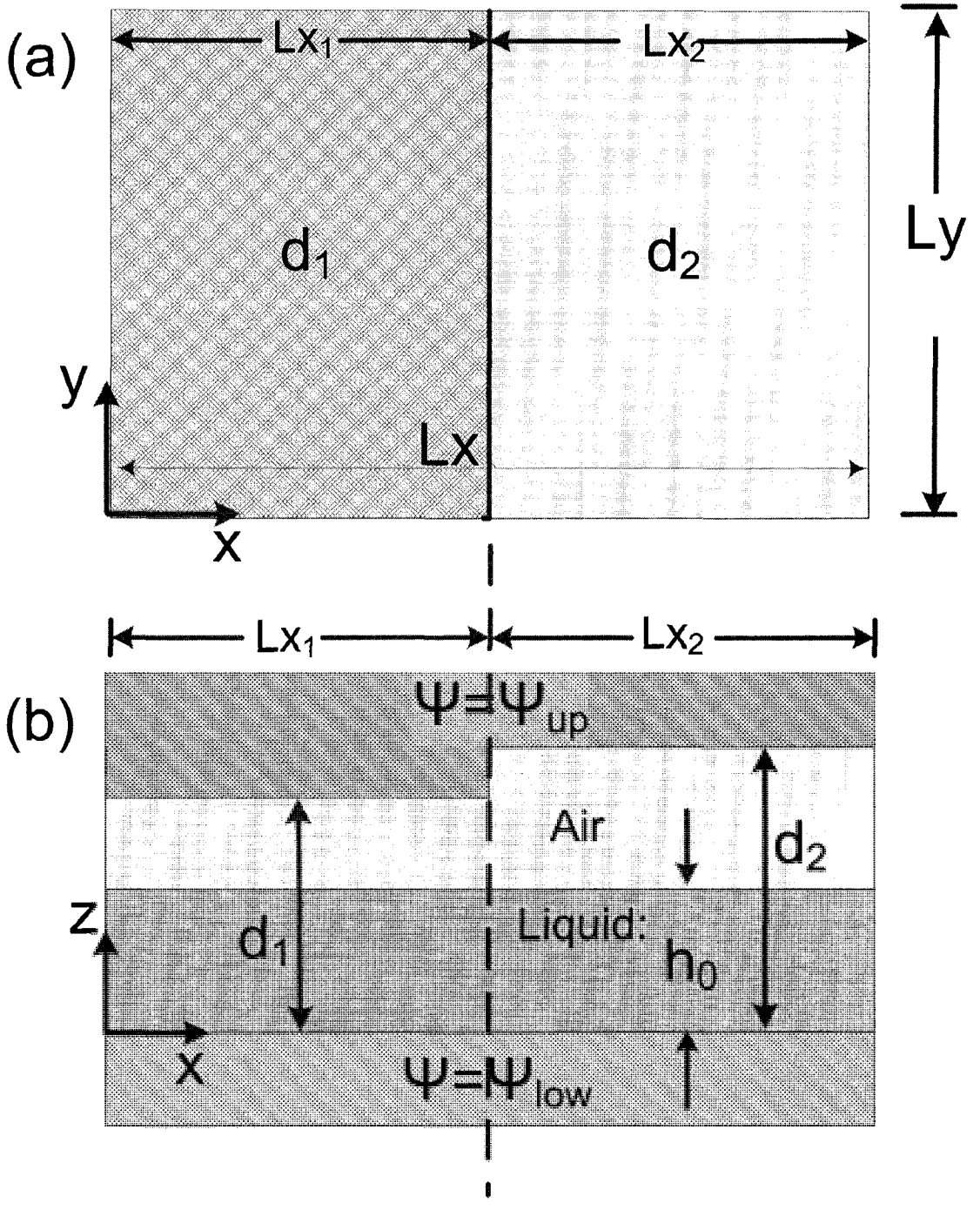

Figure 6.1: Schematic representation of the thin film system under the influence of an abrupt spatial step change in applied electric field.

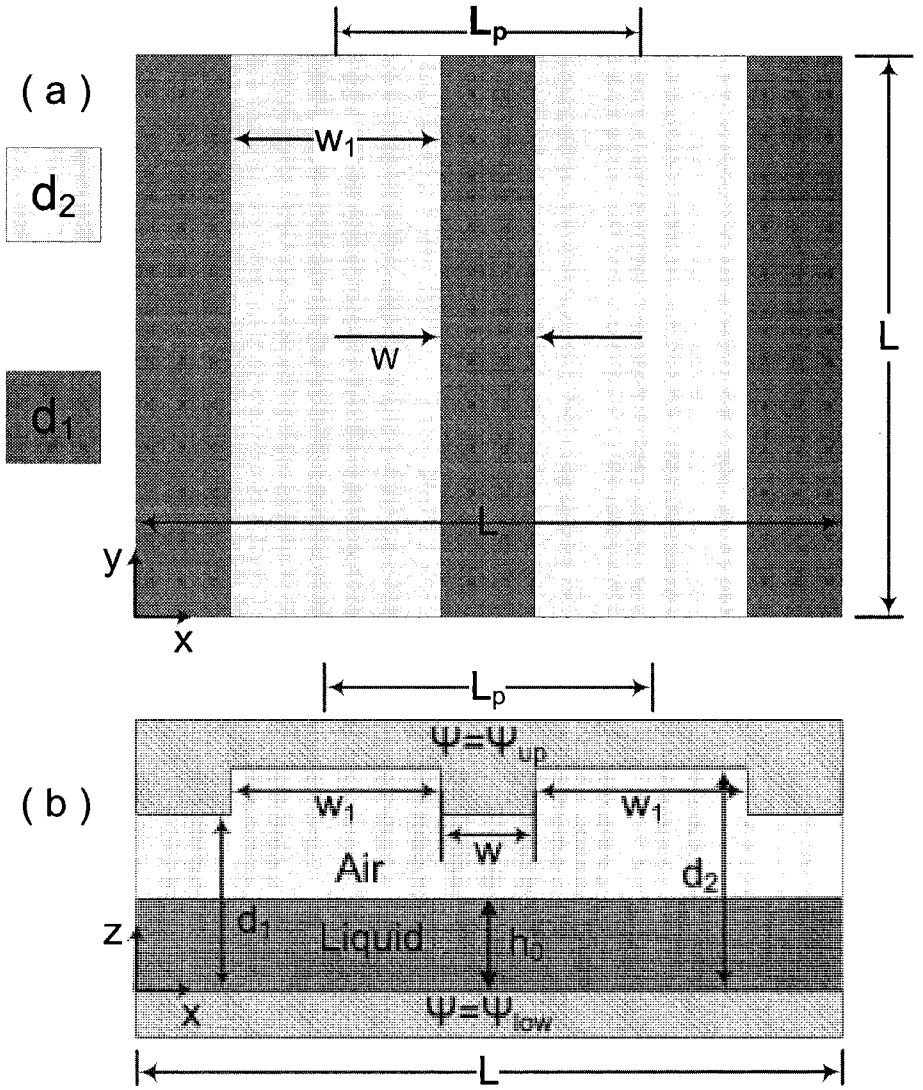

Figure 6.2: Schematic representation of the thin film system under the influence of periodic striping in the applied electric field.

6.2 Step Change in Electric Field

The application of a spatial step change in electric field strength creates a spatial gradient in conjoining/disjoining pressure. The spatial step change in electric field is created by varying the electrode spacing, $d = d(x)$, in the two half domains. Uniform electric potentials are applied to the upper and lower electrodes. For a complete description of the problem geometry, the reader is referred to section 6.1 and Figure 6.1.

For the majority of the cases considered, heterogeneity in the applied electric field is created by patterning the upper electrode. The electrode patterning is used in this study since it is easier to experimentally implement [Verma et al., 2005]. The experimental work of [Schaffer et al., 2000, Schaffer et al., 2001, Lin et al., 2001] have reported electrode spacings between $50 - 1000$ nm and a variety of patterns. To the author's knowledge no experimental work for spatially varied electric potential are available. The use of variable potential is only needed to demonstrate concepts that are difficult to produce by varying the electrode spacing.

The influence of a step change in electric field is solved on a square domain with side length $L = 6\ \lambda_c$, where λ_c is the length scale predicted by linear theory. The simulation baseline parameters and ranges of other values are shown in Table 6.1.

6.2.1 Drainage Patterns

Figure 6.3 shows the temporal evolution of an initially 75 nm thick film subjected to a spatial step change in applied electric field ($E_{p1}/E_{p2} = 10$). The step change

Table 6.1: Baseline parameters and parameter ranges employed in the simulation of electrical heterogeneity

Parameter	**Symbol**	**Value(s)**	**Units**
Relative Permittivity	ϵ_p	2.50	[-]
Viscosity	μ	1.0	[Pa s]
Interfacial Tension	γ	3.80×10^{-2}	[N/m]
Effective Hamaker constant	A_L	1×10^{-19}	[J]
Applied voltage (range)	ψ_b	$1 - 35$	[V]
Initial film thickness (range)	h_0	$10 - 80$	[nm]
Electrode spacing one (range)	d_1	$12.5 - 240$	[nm]
Electrode spacing two (range)	d_2	$60 - 595$	[nm]
Scaling Time (range)	t^*	$0.0414 - 21.12$	$[\mu s]$
Dominant Wave Length (range)	λ_c	$1.15 - 11.0$	$[\mu m]$
Stripe Width (range)	w	$0.115 - 20.9$	$[\mu m]$
Stripe Periodicity (range)	L_p	$0.575 - 41.8$	$[\mu m]$

is created by having an electrode spacing in the right half domain of $d_1 = 100\ nm$ and a spacing of $d_2 = 595\ nm$ in the left half domain. This means that a difference in electrode spacing of $\Delta d = 495\ nm$ exists in the configuration shown. The figure shows a series of gray-scale images (Figure 6.3b - Figure 6.3f) representing snap shots of the film at different instances following the application of the field to a film that has experienced a small random perturbation. Note that Figure 6.3a shows the electric field distribution in the domain with $E_{p1} = 72.7\ MV/m$ and $E_{p1}/E_{p2} = 10$. The film drains from an initial random perturbation to form a ridge and moat structure parallel to the step change in applied field (Figure 6.3b). The ridge forms on the left half domain with the larger applied field, with the accompanying moat on the right half domain. After the initial ridge and moat formation, a secondary ridge begins to grow in the left half domain (Figure 6.3c). Figure 6.3d and Figure 6.3e show the continuing evolution of the film as a third ridge develops behind the first two and less

ordered random structures are beginning to form farther into the domain. At steady state, Figure 6.3f, the first two ridges have begun to join and the random structures behind them in the left half domain have combined to form disordered structures.

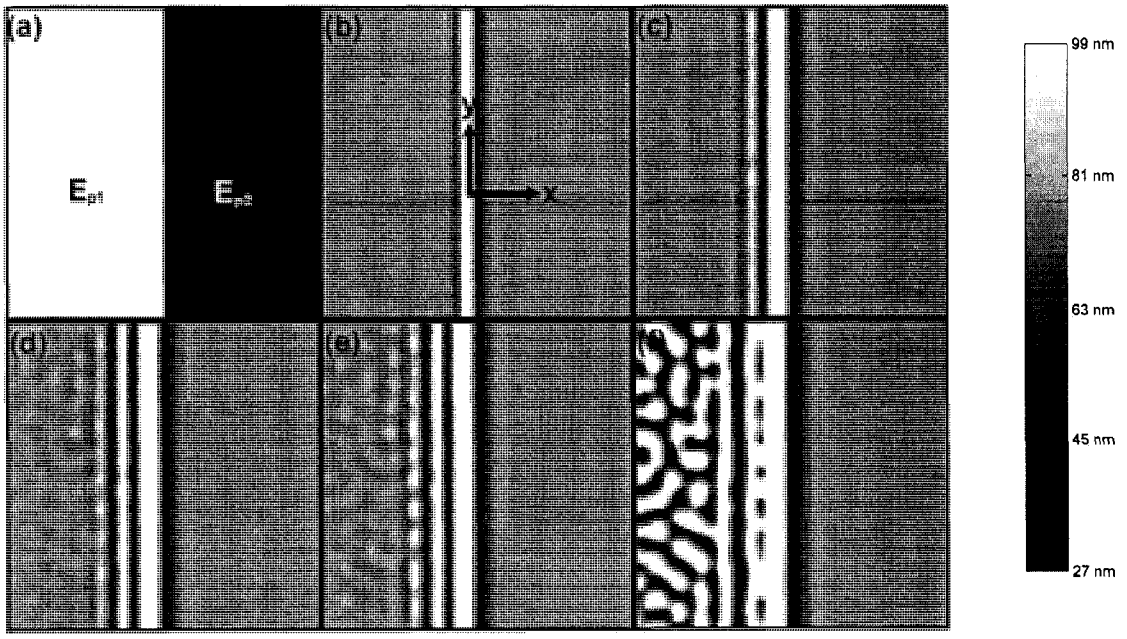

Figure 6.3: Evolution of a 75 nm thick film under the influence of an abrupt spatial step change in electric field $E_{p1}/E_{p2} = 10$. Panel (a) shows the applied electric field over the domain where a field of $E_{p1} = 72.7\ MV/m$ was applied in the left half domain. The scale-bar shown on the right does not apply to panel (a). Panels (b – f) show the film thickness at times $t = 0.3286,\ 0.7779,\ 1.091,\ 1.207,\ 2.213\ s$. All other parameters were taken as baseline values. The coordinate axis is shown in panel (b) and applies for all other panels. The domain runs from $x = [-3\lambda_c, 3\lambda_c], y = [-3\lambda_c, 3\lambda_c]$.

The results shown in Figure 6.3 are in good agreement with similar cases considered numerically by [Verma et al., 2005]. In the work of [Verma et al., 2005], inherently stable films were subjected to step changes in the applied electric field (induced by a topographically patterned upper surface). They observed that the film drainage formed three rows of ordered patterns parallel to the step change before deteriorating into less ordered structures through out the remainder of the domain.

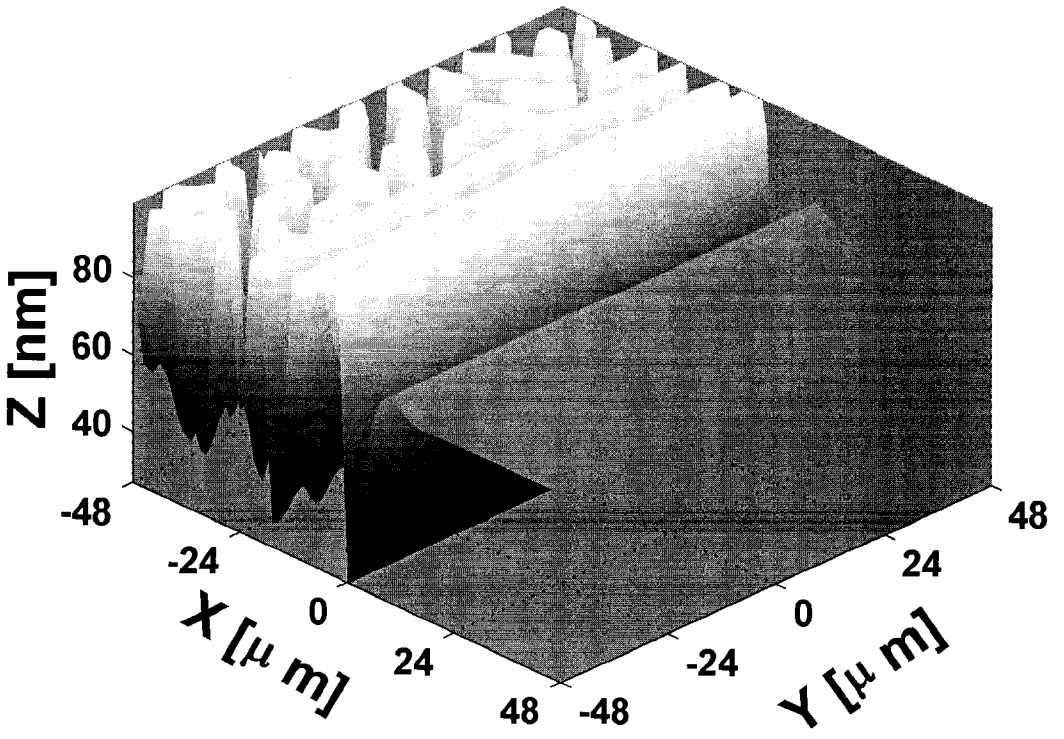

Figure 6.4: Steady state $3D$ rendering of the interface of 75 nm thick film deforming under a step change in applied electric field. This case was previously shown in Figure 6.3f.

In Figure 6.3f, there are three distinct ridges that have formed, the first two are interacting, but can still be observed. This demonstrates agreement with the published results of [Verma et al., 2005]. The additional interaction between the first two ridges is likely due to the differences in the magnitude of applied electric field and effective Hamaker constant. In [Verma et al., 2005], electric fields seven times larger are applied and the effective Hamaker constant has a negative value. The work of [Verma et al., 2005] only briefly touched on step changes in electric fields and did not discuss the timing of the reported phenomena. This work considers thin films that are prone

to pressure based drainage under the influence of a spatial step in electric field. The drainage times are also considered.

Figure 6.5 shows the maximum non-dimensional film thickness in an initially 10 nm thick film as it evolves in time under the influence of different applied electric field ratios. A thinner film then previously used will be considered to make varying the electric field more straight forward. The electric field ratios are varied by fixing the applied field in the right half domain at $E_{p2} = 42.55\ MV/m$ ($d_2 = 100\ nm$) and varying the electric field (electrode spacing) in the left half domain $d_1 = 12.5,\ 25.0,\ 50.0\ nm$ which produce fields of $E_{p1} = 615,\ 211,\ 90.9\ MV/m$ (a uniform potential of $\psi_{low} = 10\ V$ is applied to the lower electrode with the upper electrode grounded). The maximum film thickness was found by locating and tracking the fastest growing film structure. As the ratio of the applied electric fields increased, the film drainage becomes faster. Other structural aspects of the film drainage remain unaffected by the electric field ratio. As seen in Figure 6.5, the initial film drainage due to a step change in applied electric field is very fast compared to drainage induced by chemical patterning of the effective Hamaker constant which for a 10 nm thick film and a ratio of effective Hamaker constants of $A_1/A_2 = 1000$ would take 0.1876 s. The electrostatic drainage is thus orders of magnitudes faster, even for the smallest ratio of applied fields.

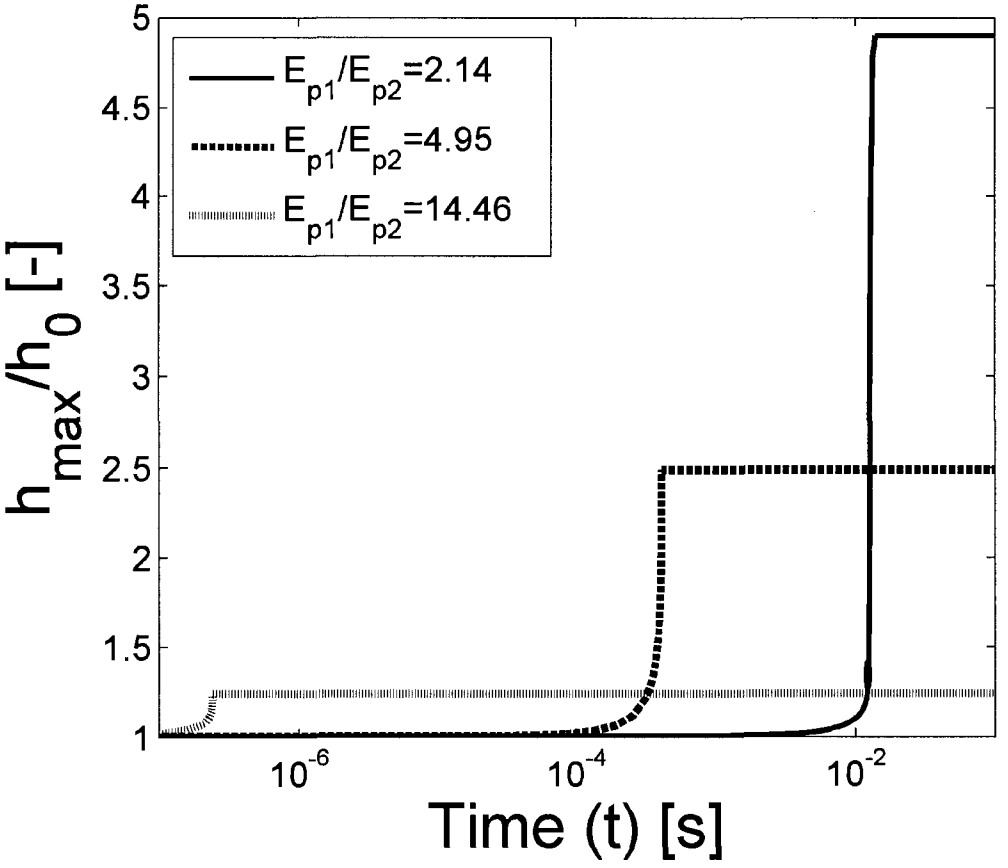

Figure 6.5: Comparison of the maximum non-dimensional film thickness for a 10 nm thick film with time for different ratios of applied electric field. All other parameters are shown in Table 6.1.

6.2.2 Influence of Initial Thickness

When the film thickness and electrode spacing are changed, the electric field at the interface of the film changes. Since the electric field at the interface between the film and surrounding fluid dictates the drainage of the film. It was difficult in the previous simulations to isolate the influence of the applied field and the film thickness, since the field is a function of the electrode spacing. To isolate only electrical effects on the drainage speed, initial film thickness, and applied field, simulations are performed employing a physically smooth upper electrode. In this case, the step change in electric field was created by applying a spatially varying electric potential. The applied potentials are fixed at 10 V in the left half domain and 1 V in the right half domain.

Figure 6.6 shows the minimum non-dimensional film thickness for films experiencing a step change in applied electric field with a fixed ratio of the electrode spacing to film thickness $d/h_0 = 4/3$. The minimum film thickness is determined by finding the fastest draining point on the film and tracking its time evolution. The different geometries and electric field combinations studied are shown in Table 6.2. The film drainage gains speed as the film thickness is decreased. For a fixed d/h_0 ratio and applied voltage, the electric field experienced by the film is different on the left and right hand side half-domains. With a fixed ratio of d/h_0 and applied voltages, the applied field changes by the same absolute amount for each change in film thickness as shown in Table 6.2.

When a thin film is subjected to a spatially stepped electric field a ridge and moat structure is formed parallel to the step change. The step change creates ordered

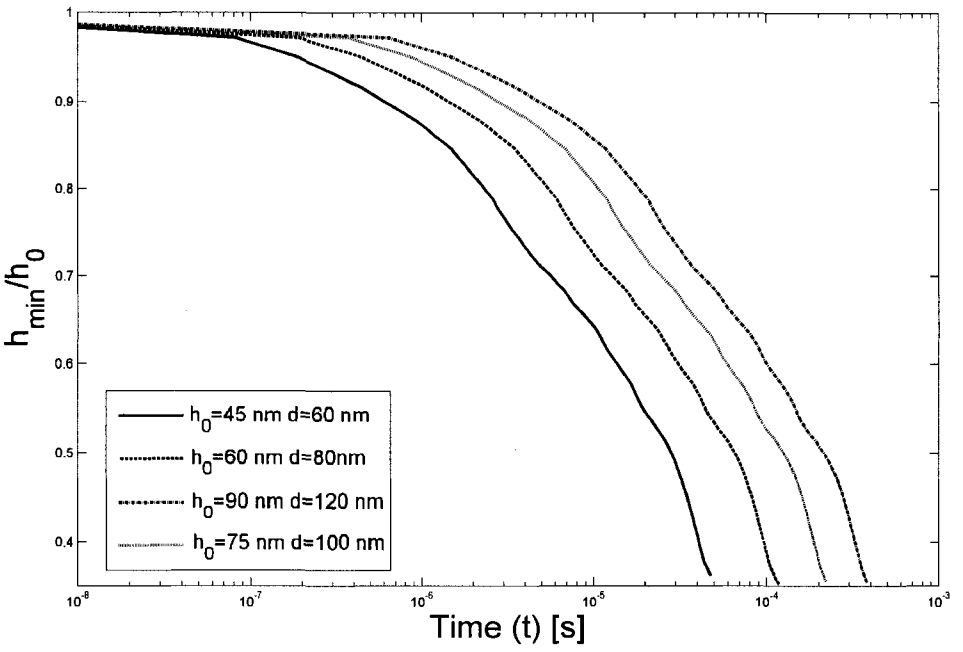

Figure 6.6: Comparison of the minimum non-dimensional film thickness for a variety of film thickness with a constant ratio of film thickness and electrode spacing $d/h_0 = 4/3$. The applied electric fields are listed in Table 6.2 and all other pertinent values are listed in Table 6.1.

features that extend into the domain on the side of higher applied field, this patterning was noted by [Verma et al., 2005]. The growth of features in the film during drainage is explosive. The film first undergoes a linear growth stage that transitions to rapid growth until the upper electrode is wet. When the ratio of film thickness to electrode spacing is fixed, the resulting film drainage is very similar. As the magnitude of the

Table 6.2: Applied electric fields for constant ratio of film thickness to electrode spacing.

h_0 $[nm]$	d_1 $[nm]$	d_2 $[nm]$	$E_{p1}[MV/m]$	$E_{p2}[MV/m]$
45.0	60.0	60.0	121.1	7.471
60.0	80.0	80.0	90.90	5.405
75.0	100	100	72.72	4.255
90.0	120	120	60.60	3.509

applied field is increased the drainage time decreases. Figure 6.7 show $3D$ renderings of the film morphology as it evolves in time. The film evolution favours the formation of elevated structures and their growth in time is very smooth, as seen previously in Figure 6.5. The minimum film thickness under goes transitions during drainage as features interact, creating kinks in its temporal evolution. As the upper electrode is wet by the liquid film, dimples in the film are forced progressively lower as more fluid is drawn to the rising structures. If a configuration of short lived highly ordered columns that then transition into a random distribution was desired, step changes in electric fields could be used to produce these structures.

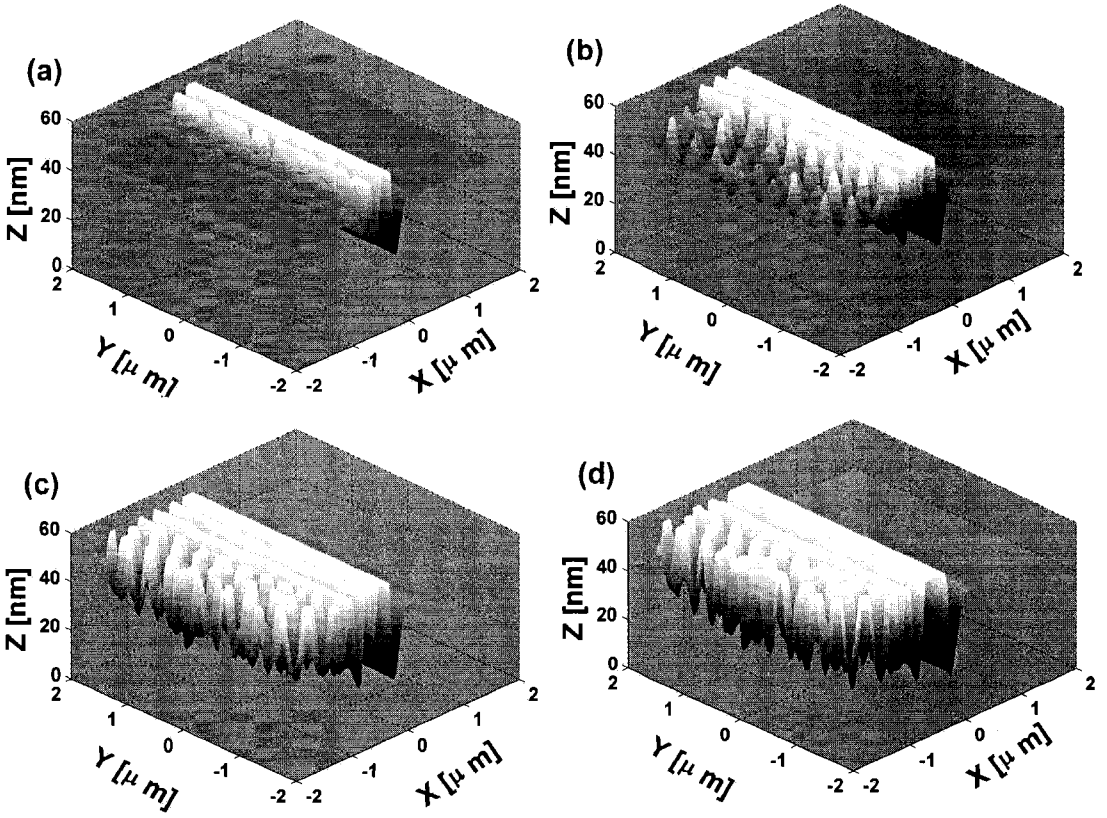

Figure 6.7: Evolution of 45 nm thick film under the influence of a spatial step change in applied electric field. The electric field step change is created by electrode spacing of $d_1 = d_2 = 60\ nm$ and $\psi_1 = 10\ V$ and $\psi_2 = 1\ V$. Panels a – d are show $t/t^* = 5.26,\ 8.03,\ 10.6,\ 12.4$. The scaling time is $t^* = 3.77\ \mu s$ and the domain size is $L = 3.49\ \mu m$. All other pertinent values are listed in Table 6.1.

6.3 Electric Field Striping

6.3.1 Electrical Pattern Variation

Thin film drainage under the influence of an abrupt step change in applied electric field is described in the previous section. The drainage under the influence of periodic striped patterns of applied electric field is examined in this section. The geometry used in the formation of the heterogeneities was discussed previously in section 6.1 a detailed schematic is shown in Figure 6.2. All simulations presented are performed on a 60×60 cartesian grid with a domain size of $L = 2\lambda_c$. The baseline parameters and ranges of other values are listed in Table 6.1.

Figure 6.8 shows the evolution of an initially 20 nm film under the influence of a spatially periodic applied electric field with periodicity $L_p = 2\lambda_c$ and width $w = \lambda_c$. Figure 6.8a shows a schematic representation of the applied electric field and is independent of the scale-bar shown to the right of the figure. Figure 6.8b – Figure 6.8e show gray-scale representations of the film thickness at the indicated times. The film drains from a small perturbation with a mean initial thickness of $h_0 = 20$ nm shown in Figure 6.8b. Depressions form at the edges of the stripes and evolve into ridge and moat structures at the heterogeneity boundaries (Figure 6.8c). The depressions (moats) form on the stripes with lower applied field and the ridges form on the stripes of higher applied field. As the ridges develop (Figure 6.8d and Figure 6.8e), they become unstable and split into a series of circular columns. The equilibrium film morphology can be see in Figure 6.8f. A remarkably ordered structure evolves at

equilibrium, which essentially consists of two parallel rows of circular columns. The columns actually connect the top and bottom electrodes. The spacing between the consecutive columns is uniform in the y direction, the spacing being approximately $\sim 0.6\lambda_c$ (center to center distance). The two rows of columns also have the same approximate spacing in the x direction, *i.e.*, $0.6\lambda_c$. The columns cross sectional area is uniform and is approximately $0.05\lambda_c^2$ with a diameter of approximately $\lambda_c/4$. The two rows of columns that form do not align in the (x, y) plane. Instead there is a slight offset, where the columns in one row appear slightly higher or lower in the adjacent row. This is due to the interactions between the columns and the random way in which they initially form.

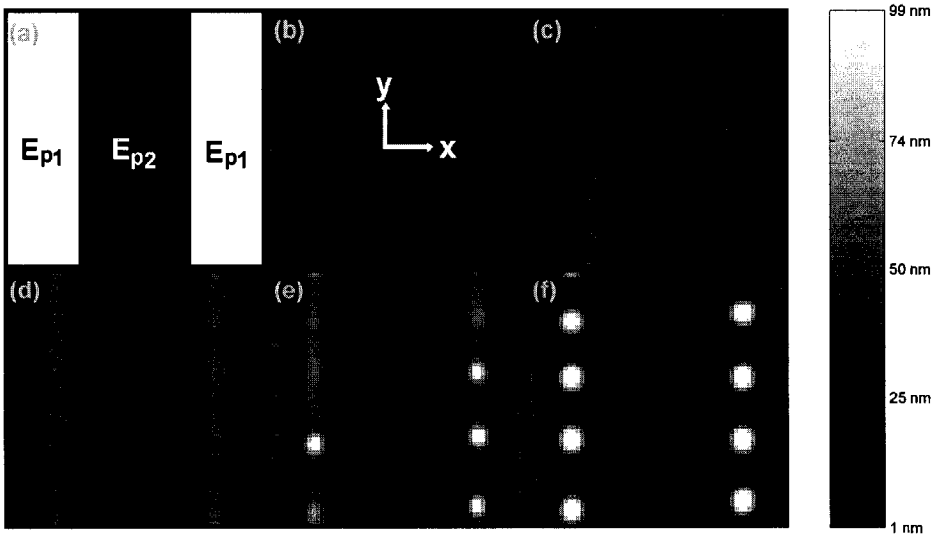

Figure 6.8: Evolution of a 20 nm thick film exposed to an electrical heterogeneity taken as a series of gray-scale images of film thickness. The applied electric field pattern can be seen in panel (a), where a stripe width of $w = \lambda_c$ and periodicity $L_p = 2\lambda_c$ define the pattern. Electric fields of $E_{p1} = 45.45\ MV$ and $E_{p2} = 9.09\ MV$ have been applied. Panels (b − f) represent the film thickness at $t = 3.000,\ 39.20,\ 181.0,\ 376.6,\ 462.9\ ms$ Note panel (a) is independent of the scale-bar on the right of the image.

The steady state film morphology is shown in Figure 6.9 which is a $3D$ representation of Figure 6.8f. The columns that form in the film taper from thicker bases to slimmer portions which wet the upper surface. The sharp gradients at the edges of the stripes result in complete drainage at these locations but in the remainder of the lower field stripes the film maintains an equilibrium thickness around 18 nm. The final film morphology and thickness variation within the film can be appreciated by examining its configuration in $3D$.

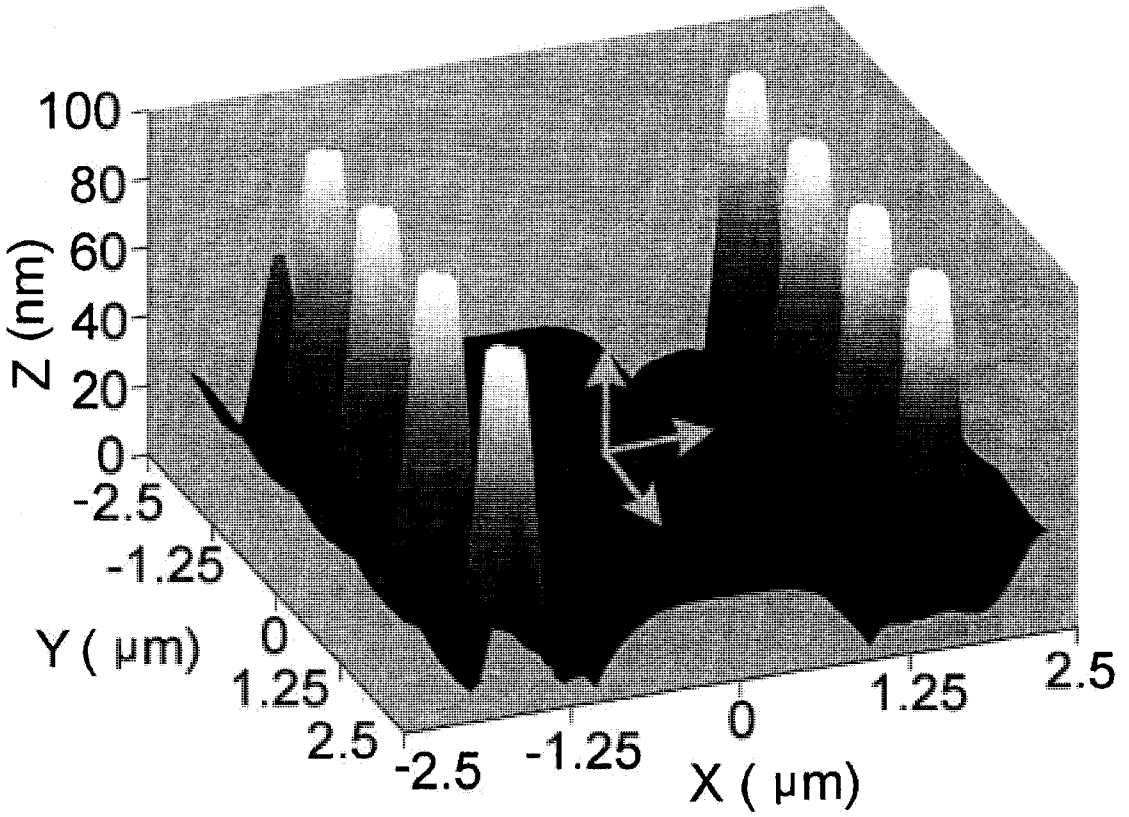

Figure 6.9: Equilibrium film configuration of an initially 20 nm thick film subjected to a periodic spatially varying electric field. The image shown is a $3D$ version of Figure 6.8f.

Figure 6.10 shows the equilibrium film morphology of a 20 nm film draining under the influence of different heterogeneously applied electric fields. Figure 6.10d – Figure

6.10f show gray-scale images of the steady state film morphology for different striped patterns with equilibrium times of $t = 462.9,\ 296.9,\ 277.9,\ ms$ respectively. Figure 6.10a – Figure 6.10c show the applied electric field schematically for the three cases shown in Figure 6.10d – Figure 6.10f where the applied fields are $E_{p1} = 45.45\ MV/m$ and $E_{p2} = 9.90\ MV/m$. The widths of each consecutive stripe are equal in every pattern. Figure 6.10d – Figure 6.10f show the changing drainage that results as the periodicity and width are successively halved. In Figure 6.10d, an electric field with a striped pattern of $L_p = 2\ \lambda_c$ and $w = \lambda_c$ (pattern shown in Figure 6.10a) drains to form two adjacent rows of columns on the stripes with the larger applied electric field. This is the case previously discussed and shown in Figure 6.8 and Figure 6.9. When the stripes are narrowed to $L_p = \lambda_c$ and $w = \lambda_c/2$ (Figure 6.10e), the two rows of columns that formed for wider stripes is reduced to a single row. This case is also shown as a $3D$ rendering in Figure 6.11. The transition from two rows of columns to a single row is a result of the increased proximity of stripe edges. The spacing and size of the columns are not influenced by the change in pattern width and periodicity. The columns have a radius of $r \sim \lambda_c/8$ and are evenly spaced with a center to center distance of approximately $\sim 0.6\lambda_c$. When the width and period of the stripes are decreased further to $L_p = \lambda_c/2$ and $w = \lambda_c/4$ (Figure 6.10f), a single row of columns forms on each stripe of larger applied field. The columns now occupy almost the entire stripe width and still demonstrate the minor lateral offsets noted previously. The drainage occurring in the film is not significantly influenced by pattern changes, as long as stripes are larger than the size of structures that form. For an initially

20 nm thick film, the difference between the width and period should be maintained in the interval $3\lambda_c/5 > L - w > \lambda_c/4$ if complete film drainage is desired.

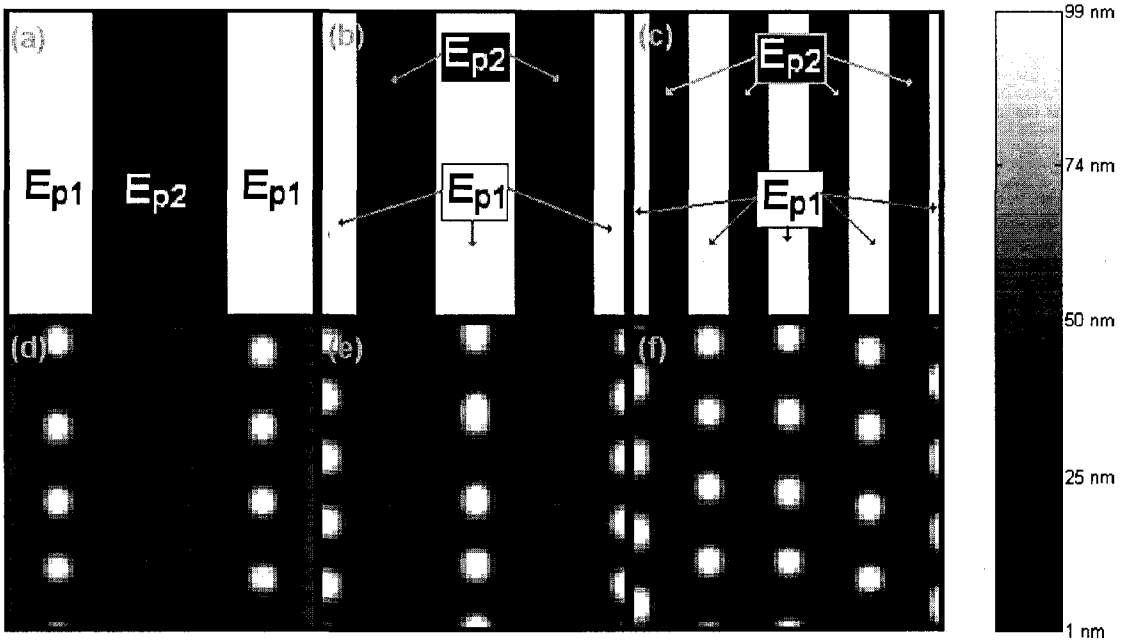

Figure 6.10: Final film morphologies of a 20 nm film for different periods and widths of the electrical heterogeneity. Panels (d – f) are gray-scale images of the films thickness. Panels (a – c) show the applied electrical field pattern and are independent of the scale-bar. The periods of the patterns shown in panels (d – f) are are $L_p = 2\lambda_c$, λ_c and $\lambda_c/2$ and widths $w = \lambda_c$, $\lambda_c/2$ and $\lambda_c/4$. The electric fields applied are $E_{p1} = 45.45\ MV/m$ and $E_{p2} = 9.09\ MV/m$.

The periodic patterns presented are very similar to those presented in the numeric simulations of [Verma et al., 2005] providing an external validation of the results. In their simulations a sinusoidal pattern is used to create ridge patterns and ordered sets of columns. Their results for a 50 nm thick film deforming under an upper patterned electrode with a sinusoidal pattern ($d = d_{avg} + \Delta \sin 2\pi x/L_p$) and average thickness of $d_{avf} = 100\ nm$ and pitch of $L_p = 0.5\lambda_c$ are very similar to those shown in Figure 6.10. In both simulations columnar structures are formed on the stripes

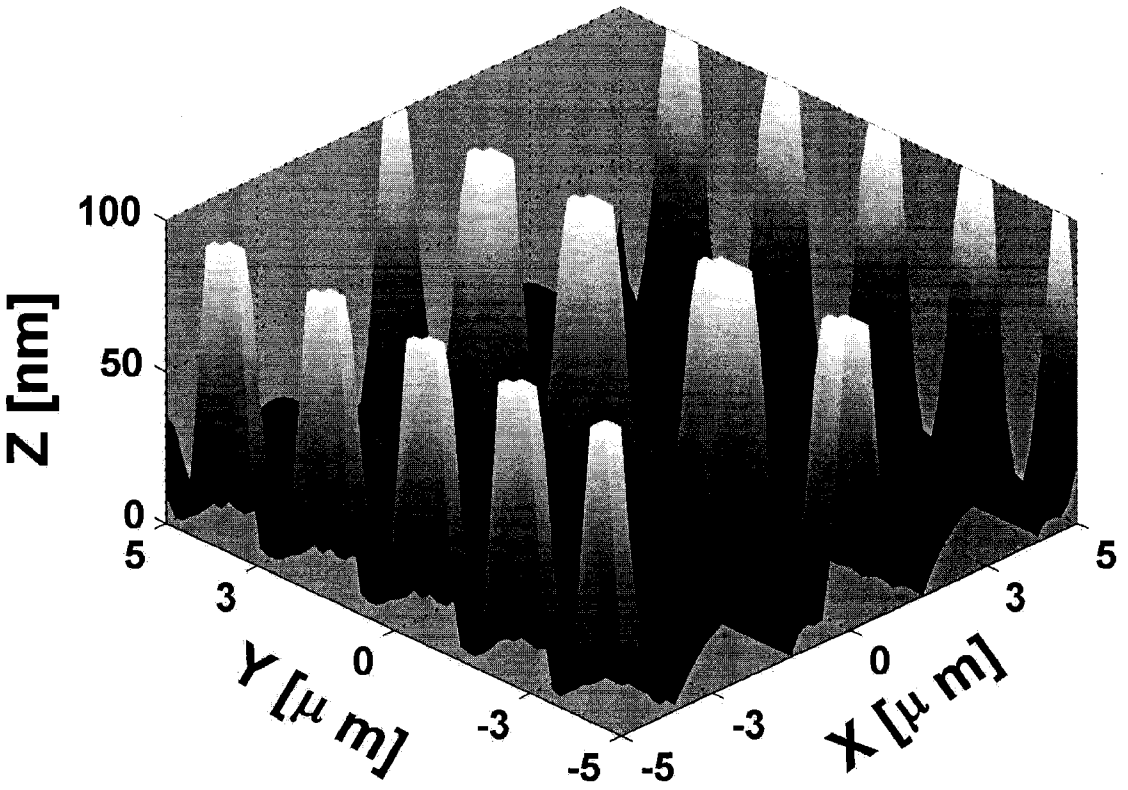

Figure 6.11: Equilibrium film morphology of a 20 nm thick film under the influence of a periodically varying electric field with periodicity λ_c and stripe width $\lambda_c/2$. This is the case previously shown as Figure 6.10e.

of higher applied electric field (lower d). The experimental results of [Voicu et al., 2006] are also very similar to the case presented in the current study. In the study of [Voicu et al., 2006], striping with a ratio of initial film thickness to electrode spacing $h_0/d_{min} \sim 0.25$ is considered. This ratio is very close to the $h_0/d = 0.2$ used in Figure 6.10. The experimental results are in excellent agreement with the numeric results shown, providing a qualitative experimental validation of the numeric results presented here. A highly ordered set of columns are formed on the stripes of higher electric field (lower d). This study extends previous work on periodic striping of electric fields since it also considers the time scales needed for drainage. The influence

of stripe width and period are also presented.

Figure 6.12 shows the equilibrium film morphology for an initially 20 nm thick film under the influence of striped applied electric fields with constant periodicity $L_p = 2\ \lambda_c$. Figure 6.12d – Figure 6.12f show gray-scale images representing the equilibrium film morphologies for different applied field distributions (scale-bar on right of plot indicates the thickness of the films shown). Figure 6.12a – Figure 6.12c show schematic representations of the applied electric field for the drainage shown in the panel immediately below (e.g. Figure 6.12a is the pattern for Figure 6.12d). In the cases shown in Figure 6.12d – Figure 6.12f, the width of the low field stripe is reduced while maintaining constant periodicity, which increases the width of the stripes with the larger applied field E_{p1}. In the cases shown, two rows of columns form along the edges of the stripes with larger applied field. Figure 6.12a shows the film drainage for a stripe width of $w = 9\lambda_c/10$, the film forms two ordered rows of columns of uniform cross section. The stripe width is reduced to $w = \lambda_c/2$ in Figure 6.12b, but the pattern produced is almost identical. Again, two ordered rows of uniform cross section columns are formed. When the width of the stripe is reduced to $w = \lambda_c/15$ (Figure 6.12c), the edges of the larger applied field stripes begin to interact with each other. These interactions cause irregularities in the columns that form along the stripe edges. When the width is larger then $w > \lambda_c/15$, as shown in Figure 6.12a and Figure 6.12b, the rows of columns are uniformly spaced. As the width w of stripes with lower applied electric field, E_{p2}, is decreased (Figure 6.12a – Figure 6.12c), the resulting drainage is not influenced until $w < \lambda_c/2$.

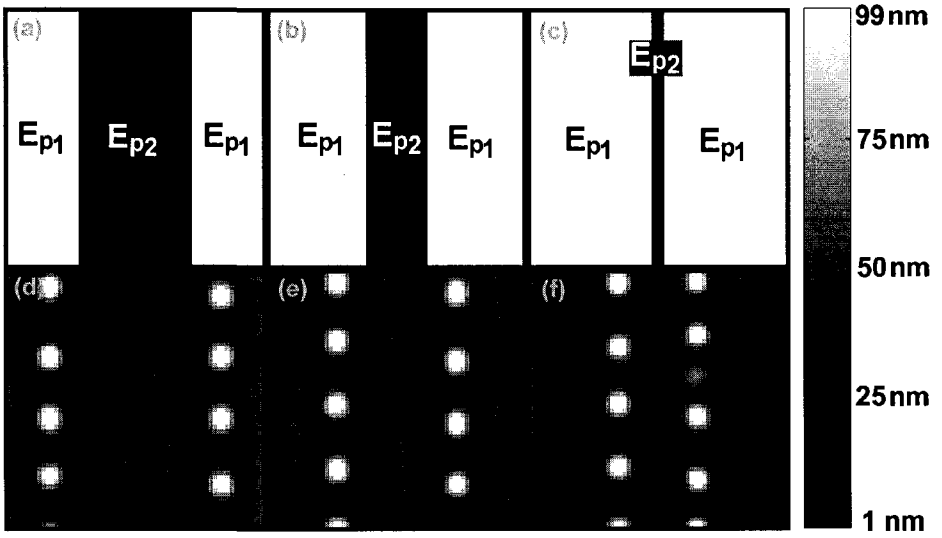

Figure 6.12: Equilibrium morphology of a 20 nm thick film under the influence of patterns in the electric field with period $2\lambda_c$. Panels (a – c) represent the electric field distribution and are independent of the scale-bar to the right of the figure. Panels (e – f) are gray-scale images of the films thickness. The periods of the patterns shown in panels (a – c) are $L_p = 2\lambda_c$ and widths $w = 0.9\lambda_c,\ 0.5\lambda_c,\ 0.066\lambda_c$

6.3.2 Influence of Initial Film Thickness

Figure 6.13 shows the equilibrium film morphology for films under the influence of an electrical pattern with period $L_p = 2\ \lambda_c$ and width $w = \lambda_c$. Figure 6.13a – Figure 6.13c show gray-scale images of the equilibrium film thickness for films of initial thickness $h_0 = 20,\ 50,\ 80\ nm$. The images use a linear gray-scale as indicated by the scale-bar. As the initial film thickness increases, the distance between the upper electrode and film interface is reduced. The increased proximity to the upper surface results in wetting of the upper surface which alters the drainage. As the film thickness is increased (moving from Figure 6.13a – Figure 6.13c), the dominant structure that forms shifts from columns ($h_0 = 20\ nm$) to two ridges ($h_0 = 50\ nm$), to a single ridge ($h_0 = 80\ nm$). The pattern replication in the film is much better for the 80 nm film as compared to the 20 and 50 nm films. It is typically considered desirable to have the film wet the upper surface on stripes with higher applied electric field. In the 80 nm thick film case, the film wets the upper electrode completely for the higher field stripes.

Figure 6.14 shows section views of the non-dimensional film thickness under the influence of a patterned electric field with period $L_p = 2\lambda_c$ and width $w = \lambda_c$. The sections shown correspond to the dashed lines in Figure 6.13 taken at $Y = 0.37\lambda_c$, this location corresponds with one of the columnar structures the forms in the 20 nm thick film. As the film thickness is increased from $20 - 80\ nm$, the drainage becomes more uniform as columns turn to a single ridge which uniformly wets the upper surface.

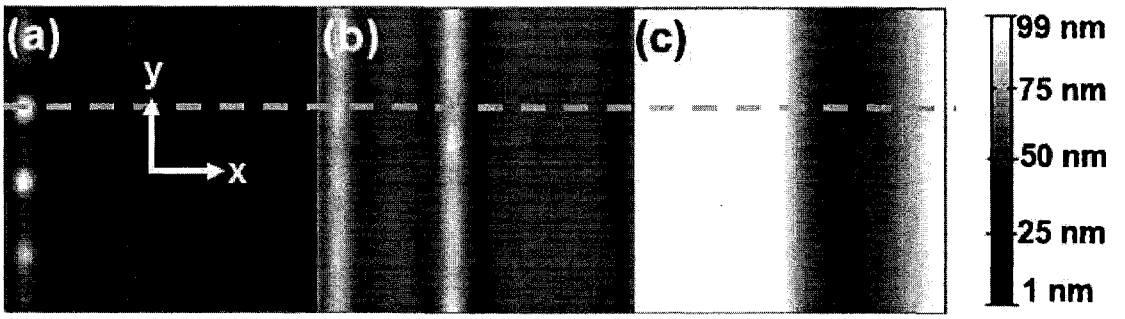

Figure 6.13: Equilibrium film morphology for a striped pattern with $L_p = 2\lambda_c$ and $w = \lambda_c$. The domain is split equally between higher and lower applied fields. Panels (a – c) are films of thicknesses $h_0 = 20,\ 50,\ 80\ nm$ with applied fields of $E_{p1} = 45.45\ MV/m$, $E_{p2} = 9.09\ MV/m$, $E_{p1} = 57.14\ MV/m$, $E_{p2} = 11.43\ MV/m$ and $E_{p1} = 76.90\ MV/m$, $E_{p2} = 15.39\ MV/m$. The electrode spacing in the right half domain is fixed at $d_1 = 100\ nm$ while the electrode spacing in the right half domain is $d_2 = 450,\ 375,\ 300\ nm$.

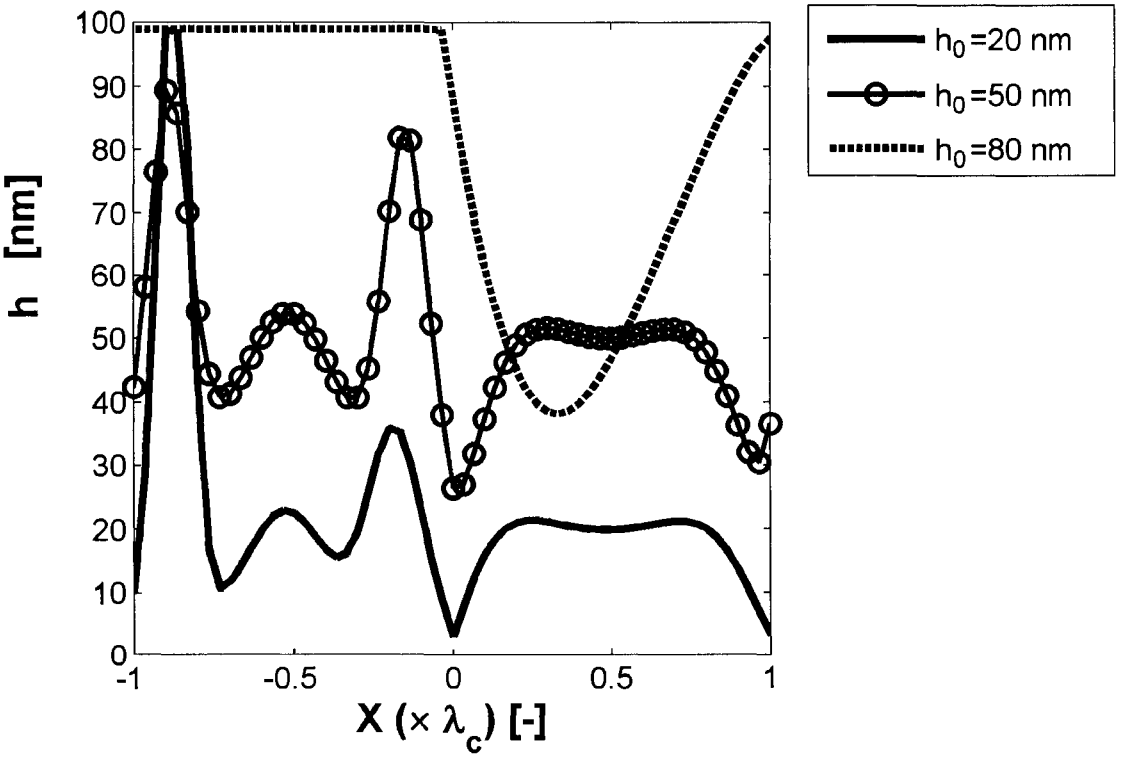

Figure 6.14: Section views (x, z) of film thickness at steady state for a striped pattern with period $L_p = 2\lambda_c$ and $w = \lambda_c$. The section views correspond to the dashed lines shown in Figure 6.13.

6.3.3 Influence of Stripe Dimensions

Figure 6.15 shows the maximum non-dimensional film thickness for an initial film thickness of 20 nm under the influence of a patterned electric field with fixed period $L_p = 2\lambda_c$. The maximum film thickness is found by finding the highest point in the domain and tracking its evolution in time. The fastest wetting of the upper surface occurs for a stripe width of $w = 1.70\lambda_c$. As the stripe width increases from $w = 0.1\lambda_c$ to $w = 1.70\lambda_c$ the time taken to wet the upper surface decreases. However, when the width is increased to $w = 1.9\lambda_c$, the time taken to wet the upper surface increases. This increase is likely due to the fact that the width of the higher field stripes has been reduced to $w_1 = 0.1\lambda_c$, which is less then the diameter of the columns that are typically formed. This reduced width of the higher field stripes retards the column growth and slows the drainage. The dynamics exhibited by the maximum film thickness has the same form for widths of $w = 0.1 - 0.9\lambda_c$. For these cases, the maximum film thickness increases rapidly during the initial stages of drainage, and then transitions to a linearly increasing regime which eventually transitions to a rapid final growth phase. The time taken to wet the upper surface increases as the stripe width is reduced. This deceleration of drainage is caused by the increased proximity of stripe edges which results in increased competition between adjacent structural features in the film.

Figure 6.16 shows the minimum non-dimensional film thickness for an initially 20 nm thick film draining under the influence of patterned electric fields with different stripe widths and a fixed period of $L_p = 2\lambda_c$. The minimum film thickness is found

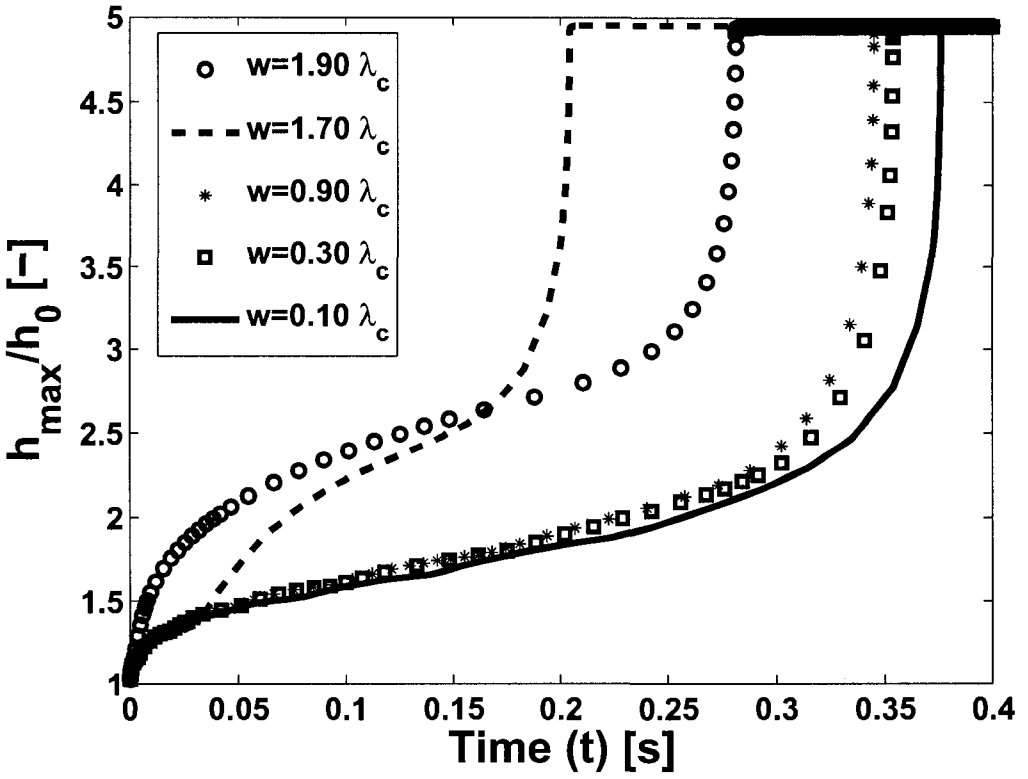

Figure 6.15: Maximum non-dimensional film thickness for a 20 nm thick film draining under the application of a spatially patterned electric field with period $L_p = 2\lambda_c$.

by finding the thinnest point in the domain and tracking its evolution. The fastest de-wetting of the lower electrode occurs for a stripe width of $w = 0.1\lambda_c$. The liquid film only drains completely to form dry spots on the lower surface when the stripe width is $w \geq 1.70\lambda_c$ or $w \leq 0.1\lambda_c$. For other cases, no de-wetting is observed and an equilibrium thickness is attained. Complete drainage occurs only in cases where one of the stripes is thin, since when the width of the lower field stripe (w) is large for a fixed period the other stripe is proportionally slimmer. For the cases shown, the width of the higher field stripe is more influential on the de-wetting of the film than the lower field stripe. As the width of the higher field stripe is reduced, the structures formed are not significantly changed but now occupy a larger portion of the stripe. This results in more fluid being drawn from the lower field stripes and more abrupt transitions which induce de-wetting.

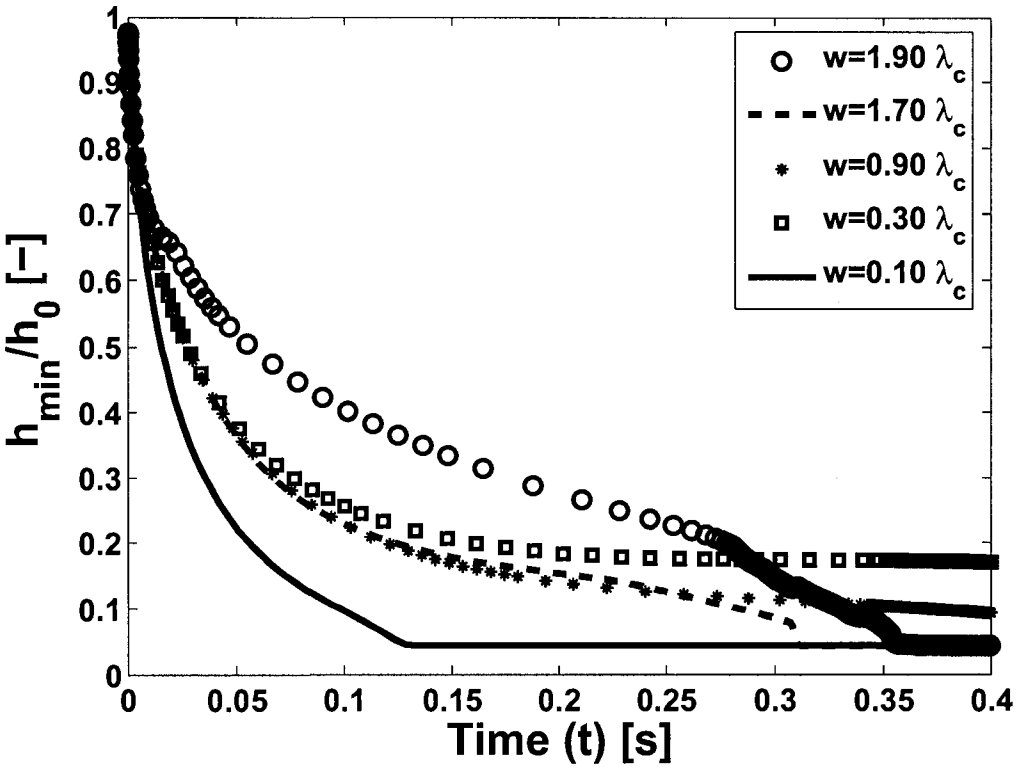

Figure 6.16: Minimum non-dimensional film thickness for a 20 nm thick film draining under the application of a spatially patterned electric field with period $L_p = 2\lambda_c$.

6.4 Concluding Remarks

A heterogeneously applied electric field is used to study its influence on film drainage. A step change in the applied field is induced by having two half domains of different electrode thickness. The final film morphology in the domain of higher applied field shows ordering of structures parallel to the step change for three separate distinct layers after which a random distribution of structures formed. These results were in good agreement with the numerical work of [Verma et al., 2005]. The ratio of initial film thickness to electrode spacing, when fixed, resulted in identical drainage behaviour. If the applied electric field was increased, the speed of film drainage increases proportionally. During the film drainage, the formation of dry spots on the lower surface is the result of interactions of separate distinct structures and creates a wavy change in minimum film thickness.

Periodic striping of the applied electric field is studied. The striped field creates patterns of columnar structures or ridges on the stripes of higher applied field. These structures are in good agreement with the numeric study of [Verma et al., 2005] and shows similarities to the experimental results of [Voicu et al., 2006]. The film drainage due to striping of the applied field creates single rows or dual rows of structures parallel to the stripe edges. As the width of lower field stripes is reduced the quality of ordering along the edges of higher field stripes degenerated. These effects are replicated for stripes of higher field were reduced below $0.3\lambda_c$. Larger variations in drainage behaviour that is observed as the stripes properties were changed. The fluid film is only prone to completely de-wet the lower surface when either stripe is reduced

by $0.3\lambda_c$. When complete de-wetting does not occur a variable equilibrium thickness is observed. The changing film drainage occurred due to changes in the amount of interaction between adjacent structures that form. When either stripe is reduced below a certain threshold the structures are forced to compete resulting in less order and complete de-wetting.

Chapter 7

Thin Film Drainage under Combined Electrical and Chemical Heterogeneity

The influence of chemical and electrical heterogeneity individually on the film drainage have been discussed in Chapters 5 and 6, respectively. In this section, the influence of combined chemical and electrical patterning will be examined. The creation of the chemically striped lower substrate and a combed upper substrate to induce electrical field heterogeneity will be discussed in detail in section 7.1. The striped patterns considered here use the same properties as defined in previous chapters, where L_p defines the pitch (frequency) of the periodic pattern (center to center distance of stripes of the same material) and w defines the width of the stipes with the higher applied electric field. The baseline parameters and ranges of other values are listed in Table 7.1.

The influence of simultaneous spatial heterogeneity in the effective Hamaker constant and applied electric field is considered by comparing the drainage patterns that result with different applied electric fields. The upper electrode patterning is fixed for

Table 7.1: Baseline parameters and parameter ranges employed in the simulation of combined electrical and chemical heterogeneity

Parameter	Symbol	Value(s)	Units
Relative Permittivity	ϵ_p	2.50	[-]
Viscosity	μ	1.0	[Pa s]
Interfacial Tension	γ	3.80×10^{-2}	[N/m]
Effective Hamaker constant	A_L	1×10^{-19}	[J]
Applied voltage (range)	ψ_b	$1 - 35$	[V]
Initial film thickness (range)	h_0	$20 - 50$	[nm]
Electrode spacing (range)	d	$75 - 100$	[nm]
Scaling Time (range)	t^*	$1.4402 - 140.6$	$[\mu s]$
Dominant Wave Length (range)	λ_c	$7.77 - 24.27$	$[\mu m]$
Stripe Width (range)	w	$1.94 - 14.76$	$[\mu m]$
Stripe Periodicity (range)	L_p	$7.77 - 15.54$	$[\mu m]$

all cases presented with a maximum spacing of $d_2 = 100\ nm$ and minimum spacing of $d_1 = 75\ nm$. The upper electrode is maintained as ground with a uniform voltage applied at the lower electrode to induce the spatially varying electric field.

7.1 Combined Patterning Geometry

The thin film system under the influence of spatially periodic striping of the applied electric field and effective Hamaker constant is depicted schematically in Figure 7.1. The (x, y) plane view, seen in Figure 7.1a, shows the extent of the chemical and electrical patterning employed. The (x, z) plane view, Figure 7.1b, shows the patterning with reference to the initial film thickness (h_0). The stripes with the smaller electrode spacing have width w and the stripes of larger electrode spacing have width w_1. The stripes have a periodicity or center to center distance of L_p, which is related to the stripe widths $L_p = w + w_1$. The striped patterns are defined by the periodicity (L_p) and the width of the stripe with larger applied field (w). The stripes are modeled

on a square domain of side length $L = 2\lambda_c$. The scaling length (λ_c), is taken from equation (3.59) and uses the larger effective Hamaker constant to define the dominant wave length. For the striped patterns considered all stripes have equal width ($w = w_1$). When the larger applied electric field (lower electrode spacing) and larger effective Hamaker constant occur on the same stripes the pattern will be referred to as *concurrent.* If the larger applied electric field and smaller effective Hamaker constant occur on the same stripe then the pattern will be referred to as *staggered.*

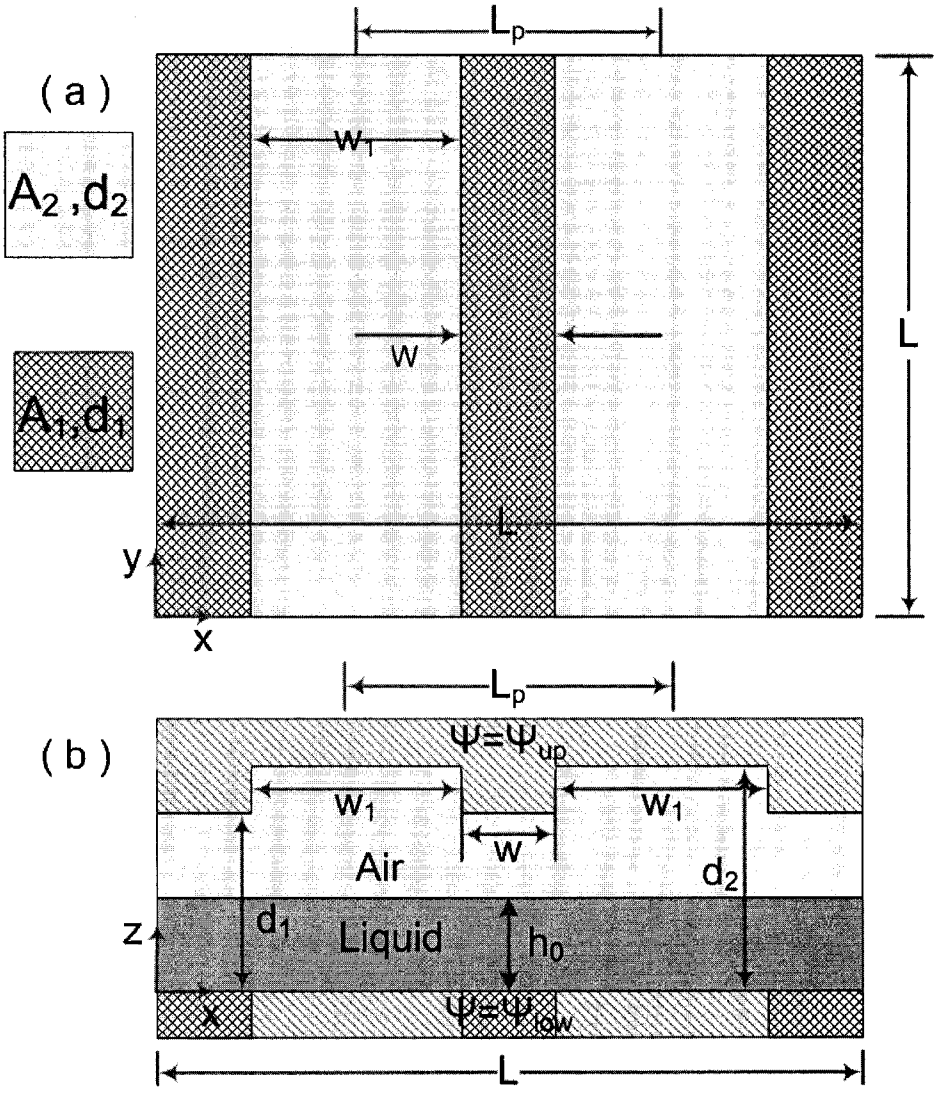

Figure 7.1: Schematic representation of the thin film system under the influence of periodic striping in both the applied electric field and effective Hamaker constant.

7.2 Comparison of Combined Patterning to Isolated Patterning

The effects of concurrent chemical and electrical heterogeneity is first compared to cases of isolated chemical and electrical heterogeneity. Figure 7.2 shows a series of gray-scale images that represent the final film morphology of an initially 20 nm thick film for isolated chemical patterning (Figure 7.2b), combined concurrent chemical and electrical patterning (Figure 7.2c) and isolated electrostatic patterning (Figure 7.2d). The pattern shown in Figure 7.2a, has periodicity $L_p = \lambda_c$ and stripe width $w = \lambda_c/2$. The simulations are performed on a domain of side length $L = 7.77\ \mu m$ and a 60×60 cartesian grid. The domain size is found by considering pressure based drainage on a homogeneous surface with the larger effective Hamaker constant ($A_1 = 1 \times 10^{-19}\ J$). The film drainage that occurs for isolated chemical patterning results in the formation of a ridge and moat structure (Figure 7.2b) and was previously discussed and shown in Figure 5.10 and Figure 5.11. In Figure 7.2c the 20 nm thick film, a 10 V electric potential is applied, creating initial electrical field strengths of $E_{p2} = 45.45\ MV/m$ and $E_{p1} = 63.5\ V/m$, the resulting film drainage forms a series of columnar structures. This case is similar to cases previously considered for purely electrical striping, but since an LVDW based scaling is used, is quite different. The structures on the higher field stripes are formed initially, with the secondary columns forming later once the initial structures have stabilized. The drainage induced by a chemically uniform substrate under the influence of the same electrical patterning as Figure 7.2c is shown in Figure 7.2d. The combination of electrical and chemical patterning (Figure 7.2c) creates a unique film morphology that shows some similarity

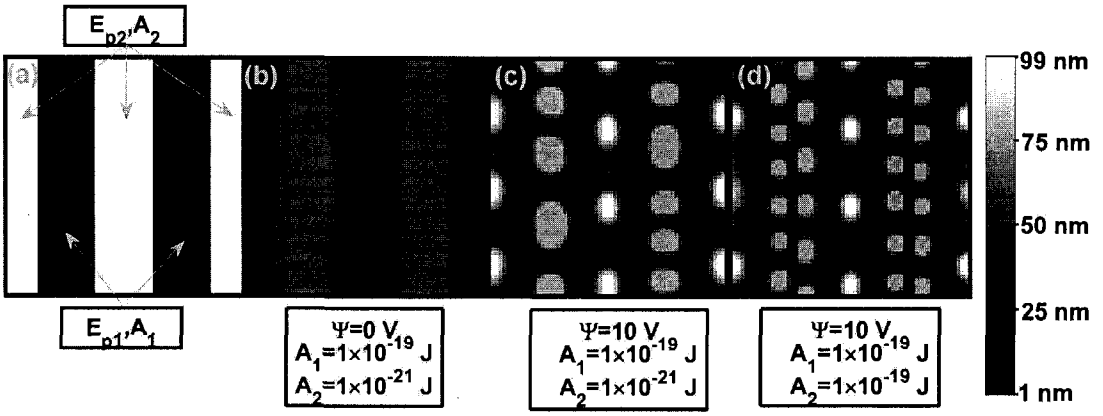

Figure 7.2: Comparison of the final drainage morphologies for an initial 20 nm thick film under the influence of different types of heterogeneity. The effective Hamaker constants and applied voltages are as indicated. The scale-bar only applies for panels (b – d), with panel a indicating the patterning that was used.

to both isolated patterning cases. The small columnar structures that form under the influence of isolated electrical patterning (Figure 7.2d) merge together to form larger structures in the case of combined chemical and electrical patterning.

Figure 7.3 shows the equilibrium film morphologies of a 20 *nm* thick film under the influence of different heterogeneities. The $3D$ morphologies in Figure 7.3a – Figure 7.3c correspond to the gray-scale images previously shown in Figure 7.2b – Figure 7.2d respectively. Figure 7.3a shows the ridge and moat structure that results under isolated patterning of the effective Hamaker constant. The influence of combined patterning of the applied electric field and effective Hamaker constant is shown in Figure 7.3b. The drainage that occurs on a chemically homogeneous substrate under the influence of electrostatic patterning is shown in Figure 7.3c. When the substrate is chemically uniform, Figure 7.3c, the small columnar structures form on the stripes with larger applied electric field. If the electrical and chemical patterning occur

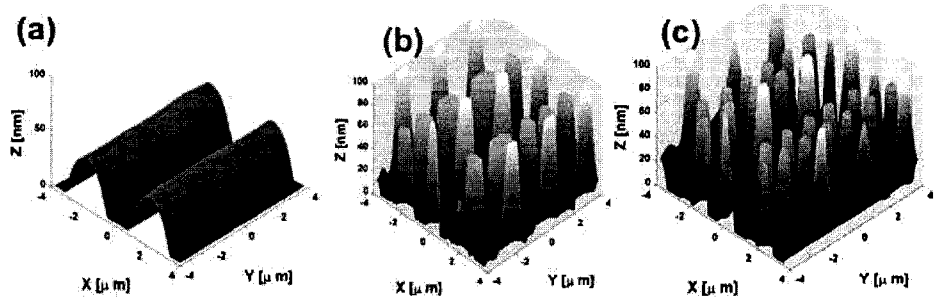

Figure 7.3: Equilibrium film morphologies for an initial 20 nm thick film under the influence of different types of heterogeneity. The film morphologies shown in panels (a – c) were shown previously in Figure 7.2b – Figure 7.2d respectively.

concurrently (Figure 7.3b) then larger columnar structures form on the stripes of larger applied electric field (and effective Hamaker constant). These larger columnar structures began as smaller structures similar to those that form in Figure 7.3c, but they have joined to form larger and less ordered structures.

Figure 7.4 shows the evolution of the minimum non-dimensional film thickness with time. The minimum thickness was found by locating the fastest growing hole and tracking its drainage. The figure compares the time evolution of the minimum film thickness for cases of combined electrical and chemical patterning (Figure 7.2c) with those of an isolated electrical pattern (Figure 7.2d). The time to complete drainage for a combined pattern occurs faster than when only an electrical pattern exists, however, the difference between the two rates of drainage is relatively small. When the time to steady state is compared for Figure 7.2b – Figure 7.2d the respective final scaled times are $t/t^* = 2.539,\ 0.03956,\ 0.00661$, where the scaling time is $t^* = 1.44\ s$. The purely electrical based drainage occurs most rapidly, followed by the concurrent patterning and finally by the purely chemical patterning. The time taken to steady state again shows that the influence of both types of patterning is important in film

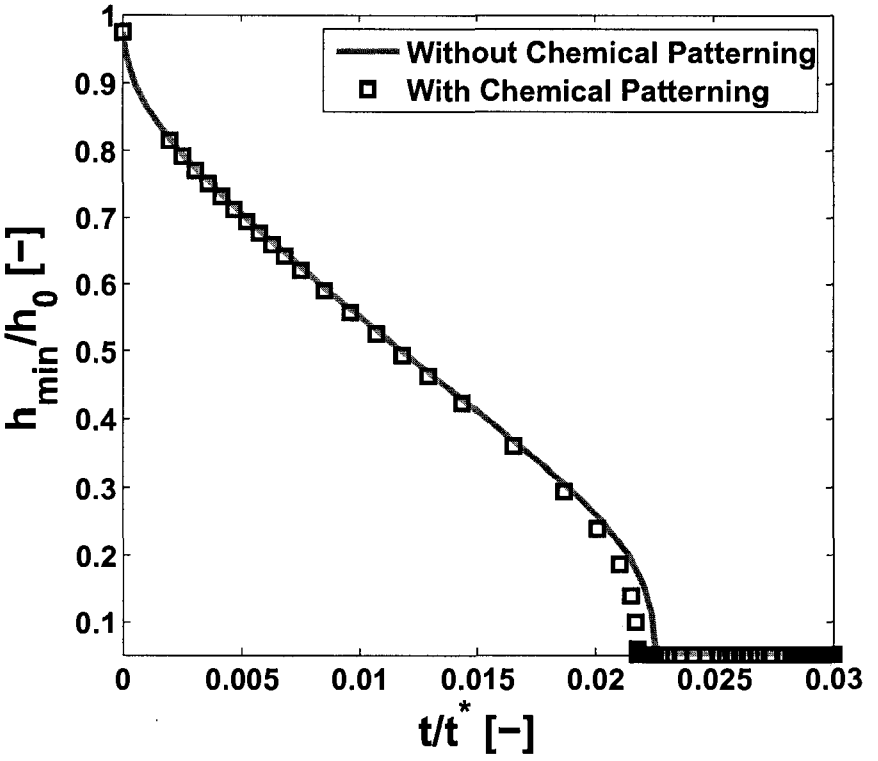

Figure 7.4: Comparison of the minimum non-dimensional film thickness evolution for a 20 nm thick film under the influence of combined patterning and purely electrical patterning. These results were shown previously in Figure 7.2c and Figure 7.2d.

drainage. The time taken to reach a maximum film thickness is also altered for the combined patterning case as compared to isolated patterns.

7.3 Influence of Changing Magnitudes of Heterogeneity

Figure 7.5 shows a series of gray-scale images that represent the final film morphology of an initially 20 nm thick film for combined chemical and electrical patterning under the influence of different magnitudes of electrical heterogeneity. The pattern used, shown in Figure 7.5a, has periodicity $L_p = \lambda_c$ and stripe width $w = \lambda_c/2$. The simulations are performed on a domain of side length $L = 7.77\ \mu m$ and a 60×60 cartesian grid. The electrical heterogeneity is induced by a comb like pattern on the upper electrode. The upper electrode is maintained as the ground ($\psi_{up} = 0\ V$), while different uniform potentials are applied on the lower electrode ($\psi_{low} \neq 0$). The steady state film morphology is shown in $3D$ in Figure 7.6a – Figure 7.6c correspond to images shown previously in Figure 7.5b – Figure 7.5d respectively. The film drainage due to only chemical patterning results in the formation of a structure of hills and valleys in the film surface (Figure 7.5b), and was previously shown in Figure 7.2b and Figures 5.10 and 5.11. In Figure 7.5c, a 2.5 V electric potential is applied on the lower electrode, creating initial electrical field strengths of $E_{p2} = 11.36\ MV/m$ and $E_{p1} = 15.87\ MV/m$. The resulting film drainage forms a series of cylindrical ovals. As the magnitude of the applied fields is increased, the high curvature of the ridges that initially form on the stripes with higher applied field cause them to break down into the oval structures observed. As the magnitude of the field is increased to $E_{p2} = 45.45\ MV/m$ and $E_{p1} = 63.5\ MV/m$ (Figure 7.5d), the film drainage forms a series of columnar structures. As the magnitude of the electrical heterogeneity is increased, Figure 7.5b – Figure 7.5d, the time required for film drainage decreases.

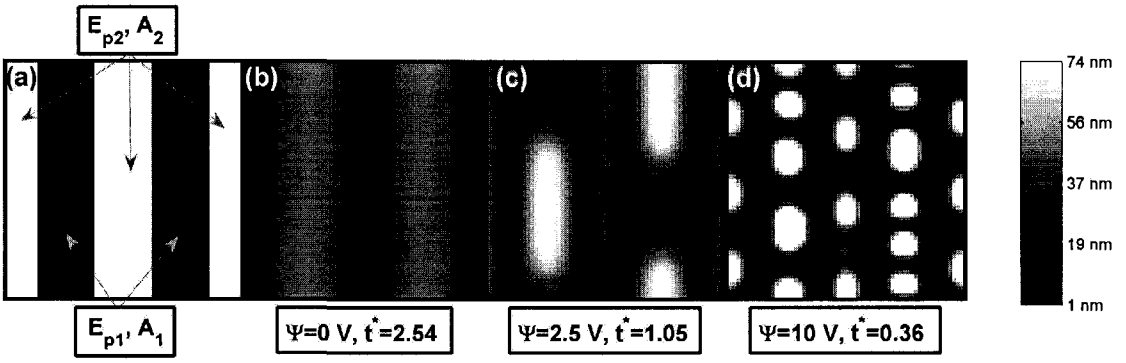

Figure 7.5: Comparison of the final morphologies for an initially 20 nm thick film under the influence of different applied electrical heterogeneity. Panel (a) shows the chemical and electrical pattern where black indicates the smaller applied field or effective Hamaker constant. In all panels the effective Hamaker constants are $A_1 = 1 \times 10^{-19}\ J$ and $A_2 = 1 \times 10^{-21}\ J$ and the electrode spacing is $d_1 = 75\ nm$ and $d_2 = 100\ nm$. The upper electrode is grounded and voltages are applied on the lower electrode. The voltages in panels (b – d) are: (b) $\Psi = 0\ V$, (c) $\Psi = 2.5\ V$ and (d) $\Psi = 10.0\ V$.

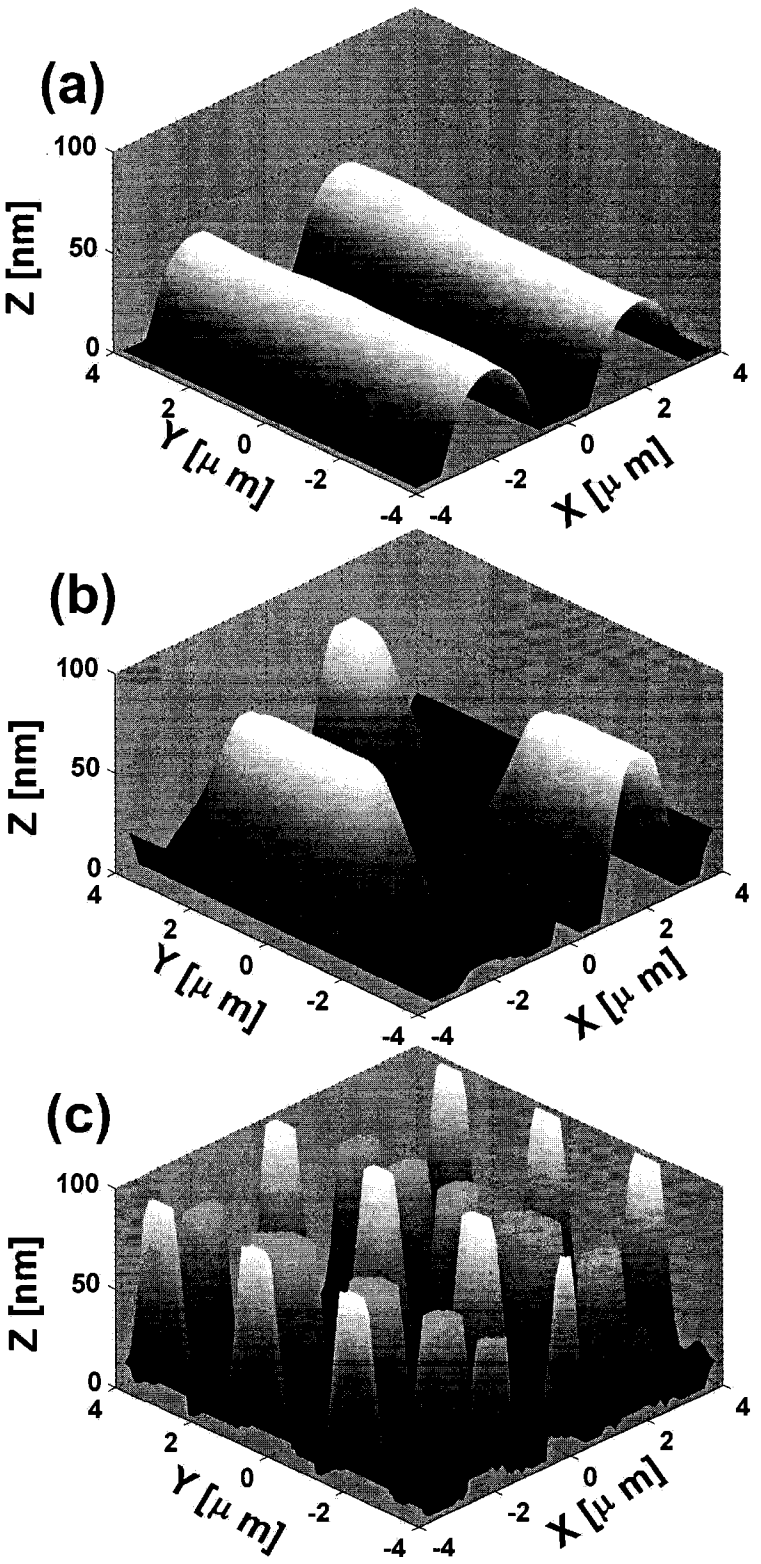

Figure 7.6: $3D$ renderings of the final morphologies for an initially 20 nm thick film under the influence of different applied electrical heterogeneity. The cases shown were previously shown in Figure 7.6b – Figure 7.6d respectively.

Figure 7.7 shows the evolution of the maximum non-dimensional film thickness with time. The maximum film thickness is found by locating the fastest growing columnar structure and tracking its growth. The drainage time decreases as the magnitude of the applied voltage on the lower electrode, ψ_{low}, and therefore, the initial electric field at the interface, *cf.* Eq. 3.55, is increased. Note that the electric field changes with time as the film morphology evolves in each simulation, although the applied potential, ψ_{low} remains fixed. The temporal evolution of the maximum film thickness with an applied voltages of 10 V demonstrates that the formation of secondary structures occurs. The formation of columns that reach the upper surface ($h/h_0 = 3.74$) occurs first on the stripes with lower electrode spacing (higher applied initial field). The second abrupt increases in film thickness in Figure 7.7 signifies the formation of secondary structures on the stripes of lower applied field.

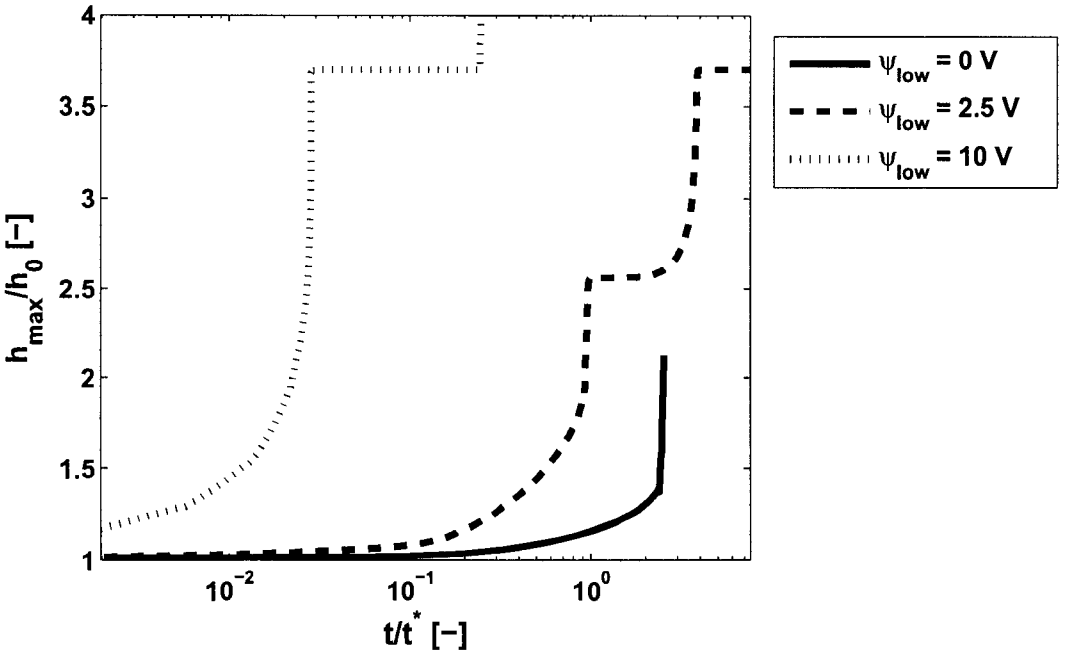

Figure 7.7: Comparison of the maximum non-dimensional film thickness for a 20 nm thick film evolving with different applied electric fields.

7.4 Influence of Changing Heterogeneity Spatial Properties

Figure 7.8 shows a series of gray-scale images that represent the final film morphology of an initially 20 nm thick film for combined concurrent chemical and electrical patterning with different spatial properties. The patterns used for each of the cases shown in Figure 7.8d – Figure 7.8f are shown above them in Figure 7.8a – Figure 7.8c. In Figure 7.8a – Figure 7.8c, the dark stripes represent the larger effective Hamaker constant ($A_1 = 1 \times 10^{-19}\ J$) and larger applied electric field ($d_1 = 75\ nm$, $E_{p1} = 63.5\ MV/m$). The light stripes have the smaller effective Hamaker constant ($A_2 = 1 \times 10^{-21}\ J$) and lower applied electric field ($d_2 = 100\ nm$, $E_{p2} = 45.45\ MV/m$). The simulations are performed on a domain of side length $L = 7.77\ \mu m$ and a 60×60 cartesian grid.

As the width of the pattern is decreased, the final film morphology changes. When the applied heterogeneity has a width of λ_c (Figure 7.8d), three rows of columns are formed. As the pattern width decreased to $\lambda_c/2$ (Figure 7.8e) a case previously shown in Figure 7.6, the smaller columns seen in Figure 7.8d and Figure 7.8f merge to form larger columns that have a diameter taking up most the stripe width they occupy. A pattern width of $\lambda_c/3$ creates a series of isolated columns with uniform spacing on the stripes of larger applied values.

Figure 7.10 shows the evolution of the maximum non-dimensional film thickness with time. The maximum thickness was found by locating the fastest growing columnar structure and tracking its growth. The drainage time decreases as the stripe width is reduced. The fastest growing structure for stripe widths of λ_c and $\lambda_c/2$ demonstrate

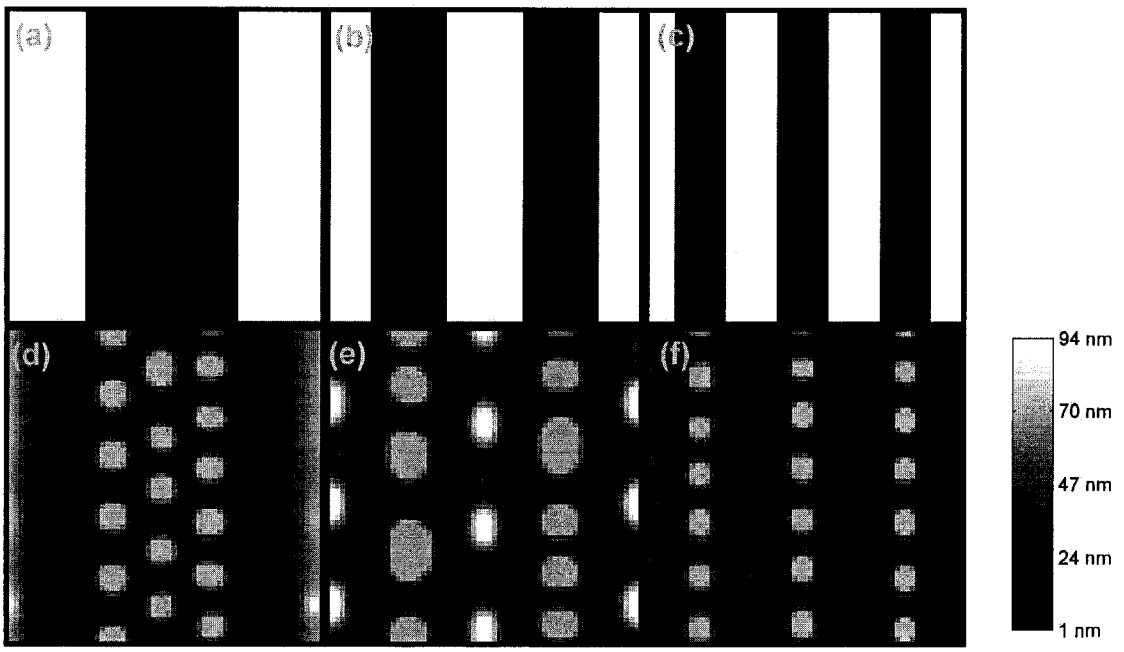

Figure 7.8: Comparison of the final drainage configurations for different combined patterning cases with patterns of pitch $L_p = 2\lambda_c$. Panels (a − c) represent the patterns that influence the films shown as gray-scale images below them. The lighter stripes represent the stripes with lower effective Hamaker constant ($A_2 = 1 \times 10^{-21}$ J) and applied field ($d_2 = 100$ nm, $E_{p2} = 45.45$ MV/m). The darker stripes have effective Hamaker constant $A_1 = 1 \times 10^{-19}$ J and applied field $E_{p1} = 63.5$ MV/m ($d_1 = 75$ nm). The electric fields are created by grounding the patterned upper electrode and applying a $\psi = 10$ V potential on the lower electrode. The pitch of all panels is $2\lambda_c$ and stripes widths vary from panels (d − f) $w = \lambda_c$, $\lambda_c/2$, $\lambda_c/3$.

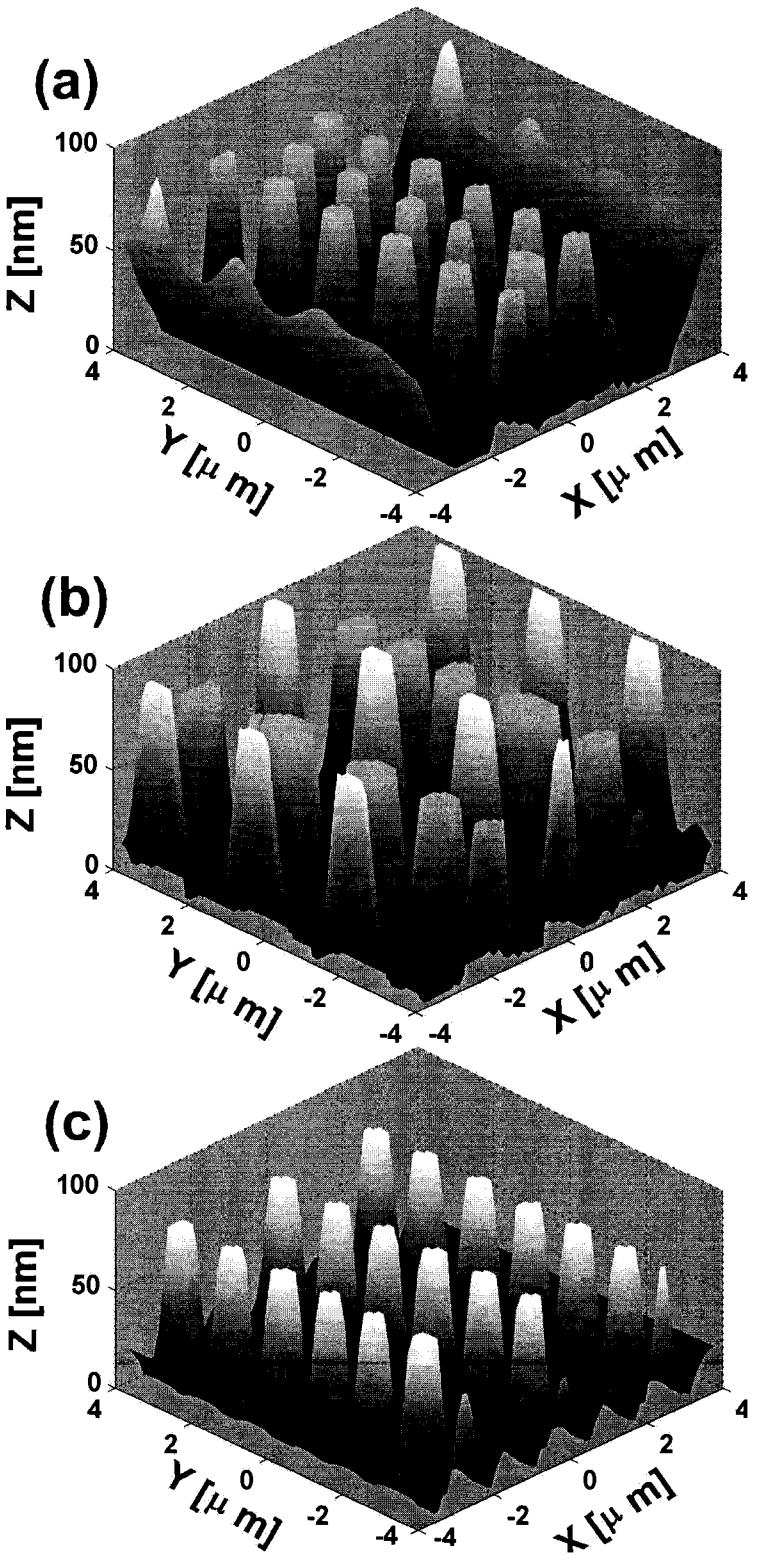

Figure 7.9: Comparison of the final drainage configurations for different combined patterning cases with patterns of pitch $L_p = 2\lambda_c$. The cases shown were previously shown in Figure 7.8d – Figure 7.8f respectively.

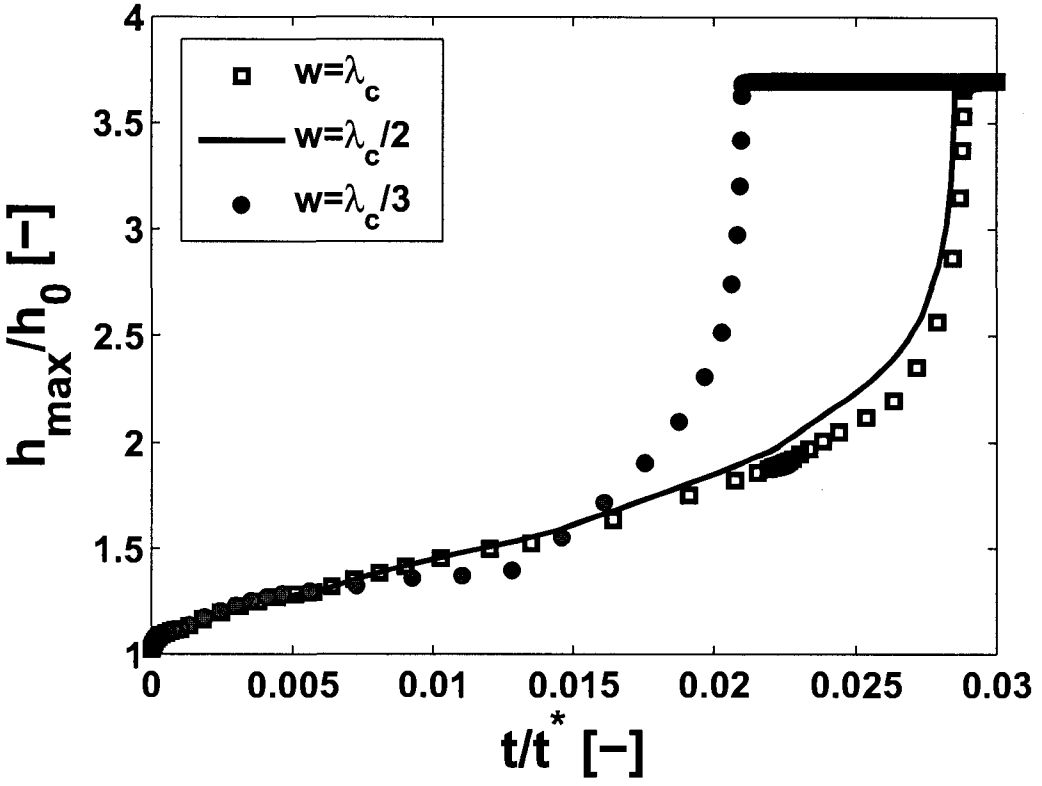

Figure 7.10: Comparison of the maximum non-dimensional film thickness evolution for different combined patterning with pitch $2\lambda_c$. The cases displayed were previously shown in Figure 7.8d – Figure 7.8f.

similar growth behaviour, with the smaller stripe width growing slightly faster. When the stripe width is reduced to $\lambda_c/3$, the drainage behaviour is significantly different then the larger stripe widths. The growth begins in a similar manner to previous cases until it reaches an inflection point, after which it grows rapidly until it reaches the maximum height (wets the upper surface). The growth of individual columns is not completely smooth as strong interactions occur between adjacent structures. These interaction leads to small ripples in the evolution of the maximum height as structures join and gain width instead of height.

7.5 Comparison of Heterogeneities with Electrical and Chemical Maximums on Opposite Stripes

The film drainage that results due to combined patterns where the maximum effective Hamaker constant and maximum applied electric field occur on opposite stripes (a staggered pattern) is examined in this section. Figure 7.11 shows a series of gray-scale images that represent the final film structures formed by drainage of an initially 20 nm thick film subjected to concurrent and staggered patterns of combined heterogeneity. The effective Hamaker constants are fixed at values of $A = 1 \times 10^{-19},\ 1 \times 10^{-21}\ J$ and the applied fields are created by the upper electrode having a comb like pattern alternating between spacing of $d = 75\ nm,\ 100\ nm$. Simulations are performed on a uniform domain size of $L = 7.77\ \mu m$.

Concurrent patterning of the electrical and chemical stripes is shown in Figure 7.11a and applies for morphologies shown in Figure 7.11b and Figure 7.11c. The concurrent pattern morphologies are also reproduced in $3D$ in Figures 7.12a and 7.13a. The staggered pattern used, Figure 7.11 d, has staggered the higher intensity electrical and chemical stripes so that the maximum electric field occurs on stripes with the minimum effective Hamaker constant. This pattern generated the morphologies seen in Figure 7.11e and Figure 7.11f, these morphologies are reproduced in $3D$ in Figure 7.12b and Figure 7.13b .

The film morphology seen for a concurrent pattern with an applied voltage of 2.5 V ($E_{p1} = 15.87\ MV/m,\ E_{p2} = 11.36\ MV/m$) can be seen in Figure 7.11b. The film forms slugs of fluid on the stripes of larger applied electric field, with small ridges

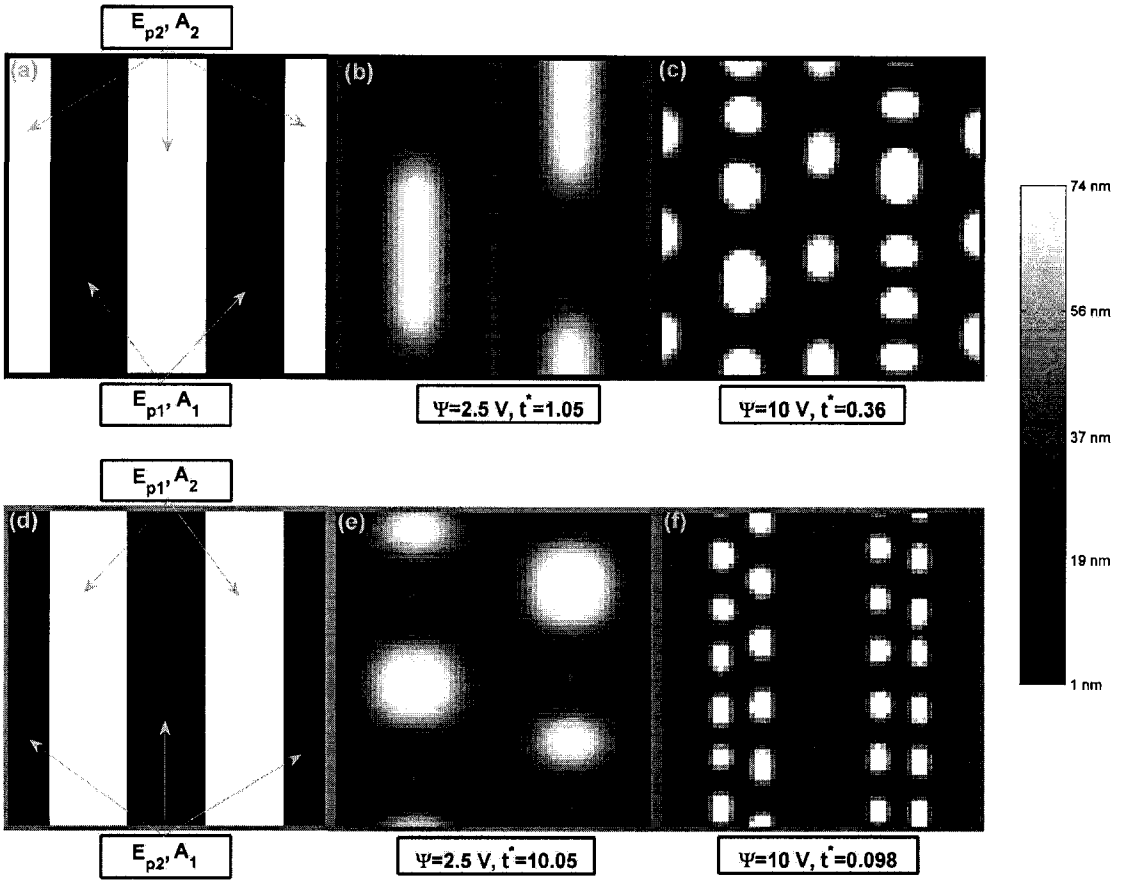

Figure 7.11: Comparison of the final drainage configurations for different heterogeneities. Panel (a) shows the patterning for panels (b) and (c), while panel (d) shows the patterning for panels (e) and (f). In panel (a) the larger effective Hamaker constant (A_1) occurs concurrently with the larger applied field (E_{p1}) on the black stripes. In panel (d) the larger electric field (E_{p1}) occurs on the white stripes along with the smaller effective Hamaker constant (A_2). In all images the effective Hamaker constants are $A_1 = 1 \times 10^{-19}\ J$ and $A_2 = 1 \times 10^{-21}\ J$. The electrical patterning is created by a combed upper electrode with spacing of $d_1 = 75\ nm$ and $d_2 = 100\ nm$. The applied voltage in panels (b) and (e) is $\Psi = 2.5\ V$ and in panels (c) and (f) is $\Psi = 10\ V$. The scale-bar on the right does not apply for panels (a) and (d).

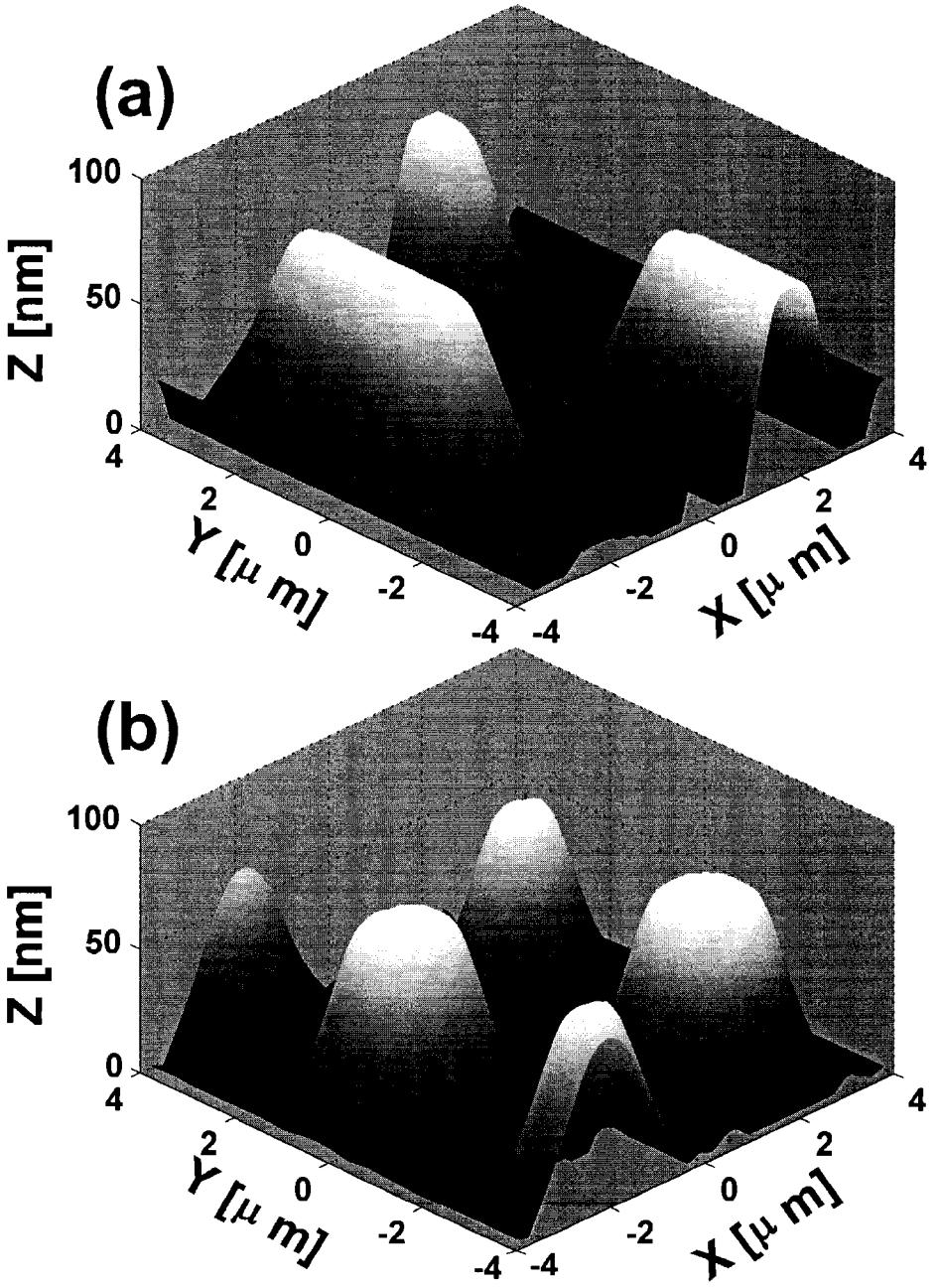

Figure 7.12: Comparison of the final drainage configurations for different heterogeneities. Panels (a – b) correspond to cases previously shown in Figure 7.11b (concurrent pattern) and Figure 7.11e (staggered pattern) respectively.

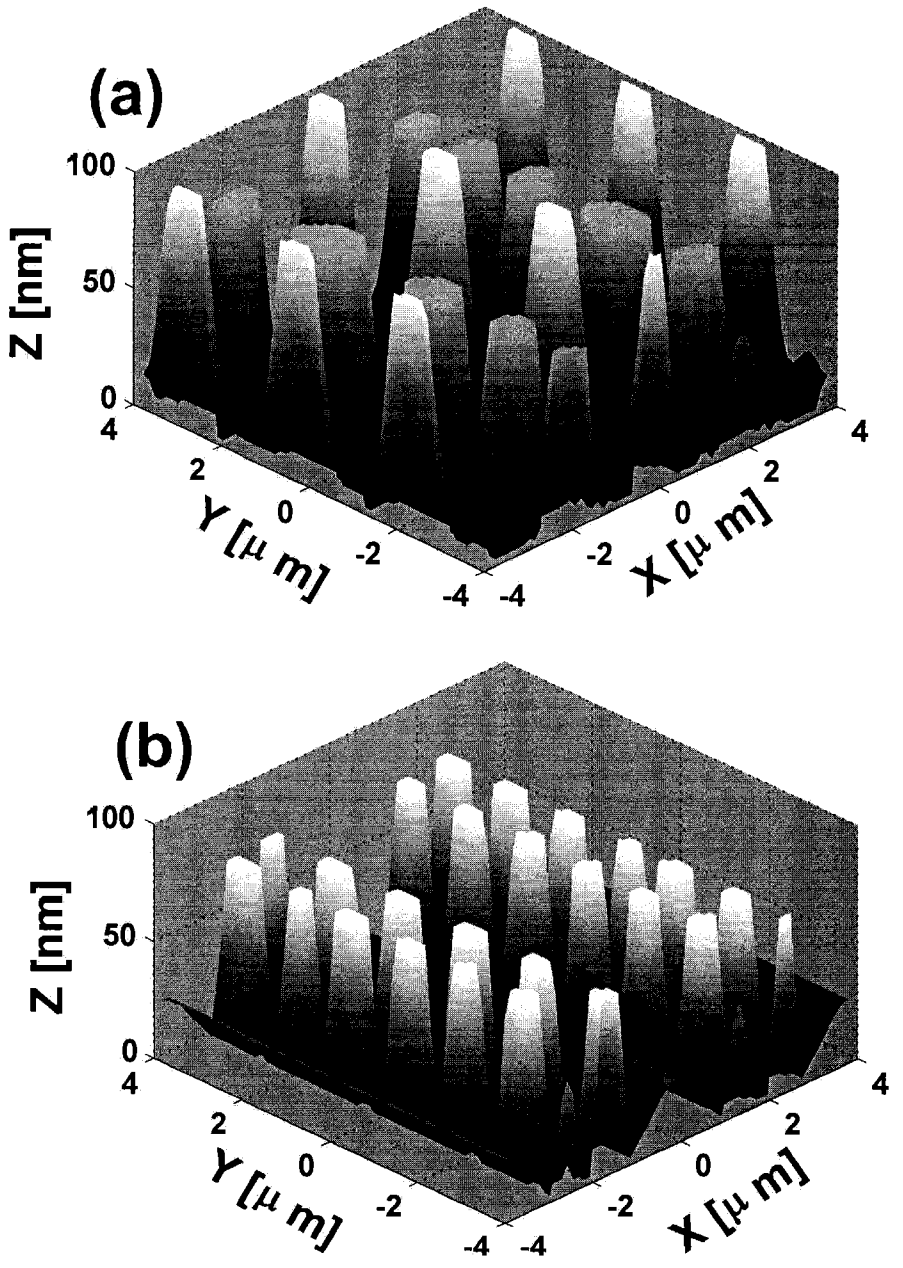

Figure 7.13: Comparison of the final drainage configurations for different heterogeneities. Panels (a – b) correspond to cases previously shown in Figure 7.11c (concurrent pattern) and Figure 7.11f (staggered pattern) respectively.

forming on the lower magnitude stripes. The fluid slugs are columnar structures that have an oval cross section. When a staggered pattern with the same stripe magnitudes is considered, the film morphology shifts to alternating larger and smaller columns (Figure 7.11e) that form on the stripes with the larger applied field. These columns spill over the edges of the stripes with larger applied field into adjacent stripes. When a larger magnitude of electric heterogeneity is applied for a concurrent pattern, Figure 7.11c, irregular columns are formed on both lower and higher field stripes. When the pattern used for Figure 7.11c, is changed from concurrent to staggered (Figure 7.11f) the film morphology is altered. In Figure 7.11f, the film forms a series of small columns on the stripes of larger electric field. A similar pattern is observed at early stages of drainage for the film in Figure 7.11c under the influence of a concurrent pattern, but when the pattern is concurrent the small structures join together and form larger structures. For this case, the staggered pattern helps stabilize structures and prevent the coalescence that happens for concurrent patterns. Staggered patterns help stabilize structures by reducing the influence of the stripe edges.

Figure 7.14 shows the evolution of the maximum non-dimensional film thickness with time for 20 nm thick films under the influence of combined electrical and chemical patterning. The maximum thickness was found by locating the fastest growing column and tracking its evolution. In Figure 7.14, pattern 1 is the concurrent pattern shown previously in Figure 7.11a and pattern 2 is the staggered pattern previously shown in Figure 7.11d. The time scales of drainage for the two patterns is similar. As the magnitude of the electric fields is increased, the difference in time scales are harder

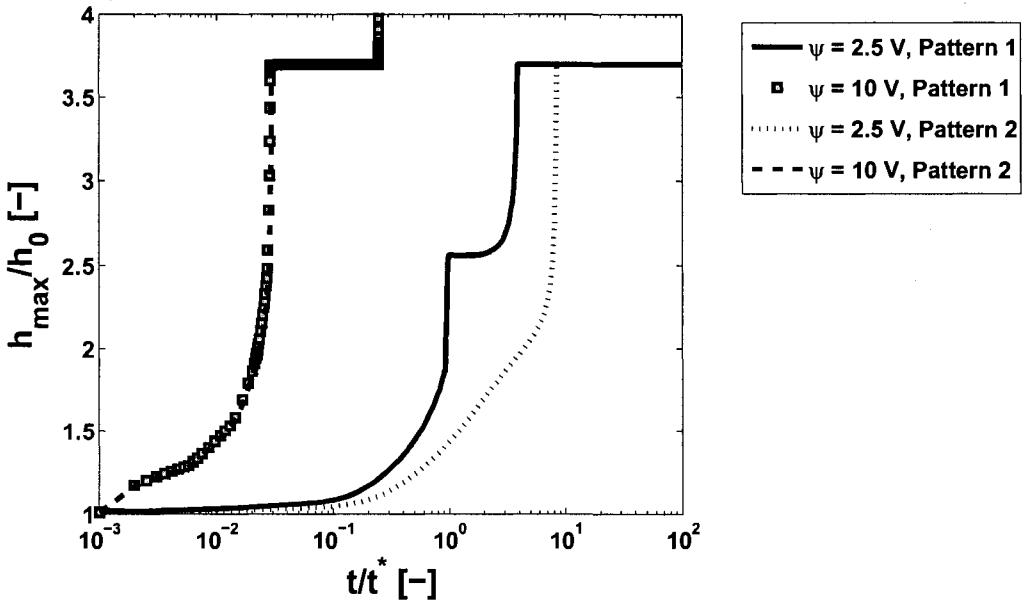

Figure 7.14: Comparison of the maximum non-dimensional film thickness evolution for a 20 nm thick film for different heterogeneities. Pattern 1 is a concurrent pattern and can be seen in Figure 7.11a. Pattern 2 is a staggered pattern and can be seen in Figure 7.11d. These cases were previously shown in Figure 7.11.

to detect, although the final film morphology is still significantly impacted.

7.6 Concluding Remarks

The use of combined patterning of the applied electric field and effective Hamaker constant exhibits behaviour attributed to both underlying phenomena. When both electrical and chemical maximums are concurrent on stripes then the structures formed have a size that is between that formed by either individually. This result indicates that the combination of electrical and chemical patterning is feasible and the production of a wide array of different sizes and types of structures is possible as the relative magnitudes are altered. When the maxima do not occur on the same stripes, but are offset (staggered), the patterns formed are very different and the structures that form can span entire stripes, where previously they would have been confined. The use of combined chemical and electrical patterning presents a wide range of opportunities for future work in this field.

Chapter 8

Conclusions and Further Research

8.1 Conclusions

A general numerical scheme using finite differences and a differential algebraic solver has been developed for simulation of the drainage of thin liquid films under the influence of intermolecular and electrical forcing. The method is capable of simulating perfect dielectric fluids under the influence of Lifshitz-van der Waals (LVDW) intermolecular forces. The method has been demonstrated to produce solutions of equivalent accuracy to the methods of other researchers in cases of both electrical and pressure based drainage. The code serves as a general simulation tool to study the drainage of thin films between chemically and electrically heterogeneous substrates, situations that emulate electro hydrodynamic (EHD) patterning based micro- and nano- lithography. The code developed is sufficiently modular to enable incorporation of free charges, and coupling of Poisson-Boltzmann electrostatics, for more generalized treatment of electro-hydrodynamically induced drainage of thin liquid films. In conjunction with large-memory fast-CPU computing clusters, and appropri-

ate parallelized algorithms for matrix operations, the program can enable simulations of very large cross-sectional area films.

The numerical code was employed in this study to observe the drainage behavior of thin films under a broad range of chemical and electrical perturbations, as well as a combination of these two types of perturbations. In the following, key conclusions of these aspects of the study are delineated.

8.1.1 Homogeneous Substrates

Numerical simulations of thin film drainage employing the long wave approximation were conducted to compare the drainage behavior under the influence of pressure and an applied electric field across the film. It is noted that apart from morphological differences in the final film structures obtained under these conditions, there is also a significant difference in time scales of the drainage, with electrostatic drainage becoming almost instantaneous compared to pressure based drainage at high applied fields. These observations indicate that drainage of films by application of electric field follows considerably different dynamics compared to pressure based drainage. The drainage of thin films under pressure based drainage showed excellent agreement with the numeric work of [Khanna and Sharma, 1997], with the drainage induced by an electric field producing results in agreement with the numeric works of [Verma et al., 2005] and experimental work of [Voicu et al., 2006].

8.1.2 Heterogeneous Substrates

8.1.2.1 Chemical Patterning

The film drainage induced by an abrupt spatial step change in effective Hamaker constants results in a moat and ridge structure being formed in the film. These structures agreed well with the results of [Kargupta and Sharma, 2001]. Changing the ratio of effective Hamaker constants does not significantly change the final film morphology but does alter the drainage speed. The numeric model employed considered an inert upper surface influencing film drainage, something that had not been previously considered. The ratio of initial film thickness to electrode spacing (d/h_0) has a small effect on film dynamics as long as the ratio is maintained above 1.25 ($d/h_0 > 1.25$). When the ratio of electrode spacing to film thickness gets below 1.25, the film drainage is slowed by the wetting of the upper surface.

When a film drains under the influence of a spatial step change in effective Hamaker constant and a homogeneous electric field, the film's morphology is altered once the field is increased above 12 MV/m. The application of a homogeneous electric field also increases the speed of drainage. Once the applied field is at a high value of 45 MV/m, the size of the resulting film structure reduces with the resulting peaks and valleys becoming more pronounced.

When a film drains in the presence of a periodically patterned effective Hamaker constant, various degrees of pattern replication are observed. The film drains to form depressions along stripe edges and then either completely or partially de-wets along the stripes of larger effective Hamaker constant. The results attained are in

good agreement with the numeric work of [Kargupta and Sharma, 2001], and has similarities to the experimental work of [Rockford et al., 1999] and [Sehgal et al., 2002]. The best pattern replication was found for stripes with a period of λ_c and width $1/2\lambda_c$ or a period of $2\lambda_c$ and stripe width $1/4\lambda_c$. Patterning of the effective Hamaker constant is a good way to de-wet the lower surface in a desired manner.

8.1.2.2 Electrical Patterning

The drainage of a thin film can be manipulated by applying a spatially varying electric field. When a step change in electric field is applied, the resulting drainage produces a series of ordered structures in the domain of larger field and a depression in the area of lower applied field. The results for step changes in the electric field were validated against the work of [Verma et al., 2005] who demonstrated similar structures in their numeric model. The influence of the step change extends into the domain of larger field creating a series of three rows of ordered structures that give way to less ordered structures far from the heterogeneity. When a constant ratio of electrode spacing to initial film thickness exists, the final film morphology will be the same with only shifts in time occurring. As the magnitude of the field is increased, faster drainage will occur on the side with larger applied field.

When a thin liquid film drains under the influence of a spatially periodic applied electric field, ordered structures will result. The type of structures that result depend closely on the ratio of electrode spacing to initial film thickness. The film may drain to form ridges, columns or wet the upper surface in a highly ordered fashion. The

film will always tend to wet the upper surface, although complete drainage is not guaranteed. Film drainage was only noted for cases where at least one of the stripes had a small width $w < 0.3\lambda_c$. If the stripe width of one or both of the stripes gets too small, then the induced flow will be competitive and less ordered structures will result.

8.1.2.3 Combined Patterning

The use of combined patterning of the applied electric field and effective Hamaker constant was explored. Two cases were considered, namely, when the larger Hamaker constant and the higher electric field were applied to the same stripe (concurrent or coincident patterns), and when the maximum Hamaker constant and higher electric fields were applied to consecutive stripes (staggered patterns). The drainage patterns that result when concurrent patterning was applied differed from when staggered patterning was employed. Using staggered patterns, structures could be made to overflow the stripe boundaries where they may not with independent or concurrent patterning. When concurrent patterning was used, structures that were not seen in either individual (chemical or electrical heterogeneity) case were observed. Even for cases where large electric fields ($> 45\ MV/m$) were applied, the underlying chemical patterning was still significant. This is a promising area for future research.

8.2 Recommendations for Future Work

Due to the large number of parameters of the model only key parameters were varied in a systematic fashion. More insight into the fluid film could be gained by performing a more detailed parametric study. In addition, a dimensional analysis of the results to isolate relevant parameters has not been performed. This field has a wide array of potential applications and areas that the program could be used to explore.

The numerical technique outlined in this dissertation was implemented using Fortran 77 with the numeric library SLATEC. An attempt has been made to ensure that the code has been written in a platform/compiler independent format which should allow its expansion and improvement in the future. Ideally the code would be expanded to model systems that incorporate a second active fluid above the film.

Once the two fluid model has been thoroughly studied, the inclusion of additional electrokinetic effects could be incorporated. The model would be able to account for interactions between two real fluids with finite conductivity deforming in an applied electric field. Numeric studies in this area could present a great deal of insight into a wide range of film dynamics.

BIBLIOGRAPHY

[Acton, 1970] Acton, F. S. (1970). *Numerical Methods that Work.* Harper and Row.

[Atherton and Homsy, 1976] Atherton, R. W. and Homsy, G. M. (1976). On the derivation of evolution equations for interfacial waves. *Chemical Engineering Communications*, 2(2):57–77.

[Benney, 1966] Benney, D. J. (1966). Long waves on liquid films. *Journal of Mathematics and Physics*, 45(2):150–&.

[Bischof et al., 1996] Bischof, J., Scherer, D., Herminghaus, S., and Leiderer, P. (1996). Dewetting modes of thin metallic films: Nucleation of holes and spinodal dewetting. *Phys. Rev. Lett.*, 77(8):1536–.

[Brown et al., 1994] Brown, P. N., Hindmarsh, A. C., and Petzold, L. R. (1994). Using krylov methods in the solution of large-scale differential-algebraic systems. *SIAM J. Sci. Comput.*, 15:1467–1488.

[Craster and Matar, 2005] Craster, R. V. and Matar, O. K. (2005). Electrically induced pattern formation in thin leaky dielectric films. *Physics of Fluids*, 17(3):032104.

[David G. Crawford, 2008] David G. Crawford, Charles R. Koch, S. B. (2008). Characteristic times for pressure and electrostatic force driven thin film drainage. *Journal of Computatoinal and Theoretical Nanoscience*, To be published.

[Grotberg, 1994] Grotberg, J. B. (1994). Pulmonary flow and transport phenomena. *Annual Review of Fluid Mechanics*, 26(1):529–571.

[Kargupta et al., 2000] Kargupta, K., Konnur, R., and Sharma, A. (2000). Instability and pattern formation in thin liquid films on chemically heterogeneous substrates. *Langmuir*, 16(26):10243–10253.

[Kargupta and Sharma, 2001] Kargupta, K. and Sharma, A. (2001). Templating of thin films induced by dewetting on patterned surfaces. *Physical Review Letters*, 86(20):4536–4539.

[Kargupta and Sharma, 2002] Kargupta, K. and Sharma, A. (2002). Creation of ordered patterns by dewetting of thin films on homogeneous and heterogeneous substrates. *Journal of Colloid and Interface Science*, 245(1):99–115.

[Khanna and Sharma, 1997] Khanna, R. and Sharma, A. (1997). Pattern formation in spontaneous dewetting of thin apolar films. *Journal of Colloid and Interface Science*, 195(1):42–50.

[Landau and Lifshitz, 1960] Landau, L. D. and Lifshitz, E. M. (1960). *Electrodynamics of continuous media.* Pergamon Press.

[Lenz and Kumar, 2007] Lenz, R. D. and Kumar, S. (2007). Competitive displacement of thin liquid films on chemically patterned substrates. *Journal of Fluid Mechanics*, 571:33–57.

[Lin et al., 2001] Lin, Z. Q., Kerle, T., Baker, S. M., Hoagland, D. A., Schaffer, E., Steiner, U., and Russell, T. P. (2001). Electric field induced instabilities at liquid/liquid interfaces. *Journal of Chemical Physics*, 114(5):2377–2381.

[Maier et al., 1993] Maier, R., Petzold, L., and Rath, W. (1993). Using daspk on the tmc cm5. experiences with two programming models. In *Scalable Parallel Libraries Conference, 1993., Proceedings of the*, pages 174–182.

[Masliyah and Bhattacharjee, 2006] Masliyah, J. H. and Bhattacharjee, S. (2006). *Electrokinetic and colloid transport phenomena.* Wiley.

[Merkt et al., 2005] Merkt, D., Pototsky, A., Bestehorn, M., and Thiele, U. (2005). Long-wave theory of bounded two-layer films with a free liquid-liquid interface: Short- and long-time evolution. *Physics Of Fluids*, 17(6):064104.

[Minkowycz et al., 1988] Minkowycz, W., Sparrow, E., Schneider, G., and Pletcher, R. (1988). *Handbook of Numerical Heat Transfer.* Wiley.

[Mitlin, 1993] Mitlin, V. S. (1993). Dewetting of solid-surface analogy with spinodal decomposition. *Journal Of Colloid and Interface Science*, 156(2):491–497.

[Oron et al., 1997] Oron, A., Davis, S. H., and Bankoff, S. G. (1997). Long-scale evolution of thin liquid films. *Reviews Of Modern Physics*, 69(3):931–980.

[Pease and Russel, 2002] Pease, L. F. and Russel, W. B. (2002). Linear stability analysis of thin leaky dielectric films subjected to electric fields. *Journal of Non-Newtonian Fluid Mechanics*, 102(2):233–250.

[Petzold, 1983] Petzold, L. (1983). Dassl: Differential algebraic system solver (d2a2). Technical report, Sandia National Laboratories.

[Reiter et al., 1996] Reiter, G., Auroy, P., and Auvray, L. (1996). Instabilities of Thin Polymer Films on Layers of Chemically Identical Grafted Molecules. *Macromolecules*, 29(6):2150–2157.

[Rockford et al., 1999] Rockford, L., Liu, Y., Mansky, P., Russell, T. P., Yoon, M., and Mochrie, S. G. J. (1999). Polymers on nanoperiodic, heterogeneous surfaces. *Physical Review Letters*, 82(12):2602–2605.

[Ruckenstein and Jain, 1974] Ruckenstein and Jain, R. K. (1974). Spontaneous rupture of thin liquid-films. *Journal of the Chemical Society-Faraday Transactions II*, 70:132–147.

[Schaffer et al., 2000] Schaffer, E., Thurn-Albrecht, T., Russell, T. P., and Steiner, U. (2000). Electrically induced structure formation and pattern transfer. *Nature*, 403(6772):874–877.

[Schaffer et al., 2001] Schaffer, E., Thurn-Albrecht, T., Russell, T. P., and Steiner, U. (2001). Electrohydrodynamic instabilities in polymer films. *Europhysics Letters*, 53(4):518–524.

[Sehgal et al., 2002] Sehgal, A., Ferreiro, V., Douglas, J. F., Amis, E. J., and Karim, A. (2002). Pattern-directed dewetting of ultrathin polymer films. *Langmuir*, 18(18):7041–7048.

[Shankar and Sharma, 2004] Shankar, V. and Sharma, A. (2004). Instability of the interface between thin fluid films subjected to electric fields. *Journal of Colloid and Interface Science*, 274(1):294–308.

[Sharma, 1993] Sharma, A. (1993). Relationship of thin film stability and morphology to macroscopic parameters of wetting in the apolar and polar systems. *Langmuir*, 9(3):861–869.

[Sharma and Jameel, 1993] Sharma, A. and Jameel, A. T. (1993). Nonlinear stability, rupture, and morphological phase separation of thin fluid films on apolar and polar substrates. *Journal of Colloid and Interface Science*, 161(1):190–208.

[Sharma and Khanna, 1998] Sharma, A. and Khanna, R. (1998). Pattern formation in unstable thin liquid films. *Physical Review Letters*, 81(16):3463–3466.

[Sharma and Khanna, 1999] Sharma, A. and Khanna, R. (1999). Pattern formation in unstable thin liquid films under the influence of antagonistic short- and long-range forces. *Journal of Chemical Physics*, 110(10):4929–4936.

[Sharma and Ruckenstein, 1986] Sharma, A. and Ruckenstein, E. (1986). Finite-amplitude instability of thin free and wetting films: prediction of lifetimes. *Langmuir*, 2(4):480–494.

[Taylor and McEwan, 1965] Taylor, G. I. and McEwan, A. D. (1965). Stability of a horizontal fluid interface in a vertical eelectric field. *Journal of Fluid Mechanics*, 22.

[Verma et al., 2006] Verma, R., Sharma, A., Banerjee, I., and Kargupta, K. (2006). Spinodal instability and pattern formation in thin liquid films confined between two plates. *Journal of Colloid and Interface Science*, 296(1):220–232.

[Verma et al., 2005] Verma, R., Sharma, A., Kargupta, K., and Bhaumik, J. (2005). Electric field induced instability and pattern formation in thin liquid films. *Langmuir*, 21(8):3710–3721.

[Voicu et al., 2006] Voicu, N. E., Harkema, S., and Steiner, U. (2006). Electric-field-induced pattern morphologies in thin liquid films. *Advanced Functional Materials*, 16(7):926–934.

[Williams and Davis, 1982] Williams, M. B. and Davis, S. H. (1982). Non-linear theory of film rupture. *Journal of Colloid and Interface Science*, 90(1):220–228.

[Wu and Chou, 2003] Wu, L. and Chou, S. Y. (2003). Dynamic modeling and scaling of nanostructure formation in the lithographically induced self-assembly and self-construction. *Applied Physics Letters*, 82(19):3200–3202.

[Wu et al., 2005] Wu, N., Pease, L., and Russel, W. (2005). Electric field induced patterns in thin polymer films: Weakly nonlinear and fully nonlinear evolution. *Langmuir*, 21(26):12290–12302.

[Wu et al., 2006] Wu, N., Pease, L., and Russel, W. (2006). Toward large scale alignment of electrohydrodynamic patterning of thin polymer films.

[Wu and Russel, 2005] Wu, N. and Russel, W. B. (2005). Dynamics of the formation of polymeric microstructures induced by electrohydrodynamic instability. *Applied Physics Letters*, 86(24):pN.PAG –.

[Xie et al., 1998] Xie, R., Karim, A., Douglas, J. F., Han, C. C., and Weiss, R. A. (1998). Spinodal dewetting of thin polymer films. *Phys. Rev. Lett.*, 81(6):1251–.

[Zhao et al., 1993] Zhao, W., Rafailovich, M. H., Sokolov, J., Fetters, L. J., Plano, R., Sanyal, M. K., Sinha, S. K., and Sauer, B. B. (1993). Wetting properties of thin liquid polyethylene propylene films. *Phys. Rev. Lett.*, 70(10):1453–.

Appendix A

Annotated Matlab Scripts

The m-files used to analyze the data in this these used Matlab versions 7.0.4.365 (R14) Service Pack 2 and 7.4.0.287 (R2007a).

Table A.1: Matlab scripts for data analysis

File Name	File Dependence	Included?	Description
buildPlots	getData, getPattern	No	This function produces the six image pseudo color plots seen indicating film evolution and inserts the appropriate color bar. It also loads the data and pattern files.
countHC	None	Yes	This function calculates the number of holes or columns using the image processing tool box. The method takes an array of thickness values and the minimum and maximum thickness used to generate a gray-scale image. After the gray-scale image is generated, two binary images are generated one for holes and a second for columns. These images are then processed to count the number of holes and columns that exist using Haralick ('Computer and Robot Vision, Volume I') counting algorithm. The objects are treated as being 8-connected. This refers to the eight pixels that surround a single pixel, 4 adjacent and 4 on diagonals. If any of these pixels have the same value as the pixel under consideration then they are considered connected. A search of the array of the binary image is performed and a count of the phenomena that register occurs.
e_field	None	Yes	This file calculates the applied electric field based on 'long-wave' approximations of the electric potential between two uniform electrodes.
getData	reformMat	Yes	This function takes the names of the data files and then loads them into a structure in matlab. It also requires a parameters structure that represents some of the typical values.

File Name	File Dependence	Included?	Description
getHC	countHC	Yes	This file will count the number of holes or columns that exist on a domain. The file uses data that has been loaded in to a structure then calls countHC.m to determine how many holes and columns exist for the time steps listed.
getMovie	None	No	This function when passed spatial locations of data points and square arrays of film thickness produces pseudo color evolution movies.
getPattern	None	No	This function reads in the pattern file and puts it into a structure.
lambda_ES	None	No	This function calculates the dominant disturbance wave length for electrostatically dominated flows.
lambda_LVDW	None	No	This function calculates the dominant disturbance wave length for pressure dominated flows.
reformMat	None	Yes	The function loads in data and then converts it from the arrays it was written in, into square arrays. It accounts for the fact that all values are written column wise in the Fortran program.
scale_LVDW	None	Yes	This file will calculate the length and time scales used for Pressure based drainage.
scale_ES	None	Yes	This file will calculate the length and time scales used for Electrostatically based drainage.

Table A.2: Fortran files

File Name	File Dependence	Description
DDASL.f	SLATEC.lib, FCN	Differential Algebraic solver from the library SLATEC.
DERXX.f	None	This function performs a three point central differencing to attain the second derivative of in the x direction. It uses the column wise storage scheme and requires the full vector of thicknesses.
DERYY.f	None	This function performs a three point central differencing to attain the second derivative of in the y direction. It uses the column wise storage scheme and requires the full vector of thicknesses.
FCN.f	PHI, DERXX, DERYY	This function performs the full Finite Difference approximation used to reduce the system of partial differential equations to a system of differential algebraic equations.
GETEX.f	None	This function searches an array and returns the location of the largest and smallest points.
OVERWRTVEC.f	None	This subroutine overwrites the values passed to the file named. If the file does not exist one is created.
PATTERN_BUILD.f	WRTVEC	Creates a pattern file of values for the effective Hamaker constants on the upper and lower surfaces, applied voltage and electrode spacing.
PHI.f	None	This function calculates the conjoining/disjoining pressure in the film. The user has the option by setting flags of using electrostatic interactions, LVDW at the lower or upper surfaces, Born like repulsion at the upper and lower surfaces and a lumped approximation of LVDW and Born at the lower surface.
READ_DATA.f	READVEC	This subroutine reads in a file and then truncates any extra values that may have been written to the file.

File Name	File Dependence	Description
READ_PATTERN.f	READ_DATA	This subroutine reads in a pattern file created by PATTERN_BUILD. It reads in the data file and truncates any extra values that may exist.
READNAMES.f	None	This subroutine reads in a series of strings that are then used as the names for file writing.
READVALUES.f	None	This subroutine reads in the numeric parameters that are passed to the THINFILM program.
READVEC.f	None	This subroutine reads in a formatted data file that has been previously written in the structure used by WRTVEC.
RECORD_PARAMS.f	None	This subroutine writes a series of problem parameters to a file.
RECORD_VALUES.f	WRTVAL, WRTVEC, OVERWRTVEC	This subroutine calls the other subroutines and writes the problem data from a given time step to the appropriate files.
REPORT_PARAMS.f	None	This subroutine writes the problem parameters to the default output for fortran.
REPORT_SCALING.f	None	This subroutine writes the problem scaling as calculated to the default output for fortran.
THINFILM.f	FCN.f, GETEX.f, OVERWRTVEC.f, PHI.f, READ_DATA.f, READ_PATTERN.f, READNAMES.f, READVALUES.f, READVEC.f, WRTDAT.f, WRTVEC.f	Main file. Includes the calculation loop where DDASSL.f is called to solve the differential algebraic system. Error checking, convergence and data writing/reading are performed in this file.
WRTDAT.f	None	This function appends a single time value and then the additional array values to to the file specified.
WRTVAL.f	None	This subroutine appends a single value to an existing data file, or starts a new file with a single value.
WRTVEC.f	None	This function appends the data passed to the specified file.

A.1 Scaling Calculating Scripts

```
%-------------------------------------------------------------------
%   START   e_field
%-------------------------------------------------------------------
%This function calculates the electric field between the
%two electrodes at a point h with the electrode spacing d.
%
%Sample Call
%e_field(Ep,Psi_b,d,h)
%
%Ep     Relative permativity ratio (-)
%Psi_b  Voltage applied at lower electrode (V)
%d      Electrode spacing (m)
%h      Point to calculate field

function e_field=f(Ep,Psi_b,d,h)
e_field = Psi_b/(d*Ep-(Ep-1)*h)

%-------------------------------------------------------------------
%   END  e_field
%-------------------------------------------------------------------
%*******************************************************************
%Start scale_LVDW
%*******************************************************************
%This function returns the scaling for time and length used in the
%non-dimensionalisation of the thin film model for LVDW flows.
%Relation taken from
%Khanna, 1997, Journal of Colloid and Interface Science
%'Pattern formation in thin Apolar films'
%
%Sample Call
%scale_LVDW(mu,gamma,h_zero,A)
%
%where:
%mu     fluid viscosity (Pa s)
%gamma  interfacial tension (N/s)
%h_zero initial film thickness (m)
%A      effective Hamaker constant (J)
%
function t_scale_LVDW=f(mu,gamma,h_zero,A)
scale_LVDW.t=12*(pi^2)*mu*gamma.*(h_zero.^5)*A^-2;
scale_LVDW.x=(h_0^2)*sqrt(2*pi*gamma/A);
%*******************************************************************
%End scale_LVDW
%*******************************************************************

%===================================================================
%Start scale_ES
%===================================================================
%This function returns the scaling time and length used in the
%non-dimensionalisation of the thin film model for ES dominated flows.
```

```
%Relation taken from
%Verma, 2005, Langmuir
%'Electric field induced instability and pattern formation in
%thin liquid films'
%
%Sample Call
%scale_ES(mu,gamma,h_0,E_p,Psi_b)
%
%Where:
%mu          viscosity [Pa s]
%gamma       interfacial tension [N/m]
%h_0         initial film thickness [m]
%E_p         permitivity of film [-]
%Psi_b       Applied potential [V]
function t_scale_ES=f(mu,gamma,h_0,E_p,Psi_b)
%permitivity of free space
E_0=8.8541878176E-12;
scale_ES.t=3*mu*gamma.*h_0.^3./(0.5*E_0*E_p*(E_p-1)*Psi_b^2)^2;
scale_ES.x=sqrt((gamma*h_0^3)/(0.5*E_0*E_p*(E_p-1)*Psi_b^2));
%=====================================================================
%End scale_ES
%=====================================================================
```

A.2 Hole and Column Counting Script

```
%**********************************************************************
%   START        getHC
%**********************************************************************
%This function returns the modified structure
%passed to it while counting the number of holes
%and columns measured.
%
%Sample Call
%getHC(struct,hmin,hmax,ArraySize,spacing)
%
%struct     Structure containing values of thickness,time,
%           minimum thickness and maximum thickness vectors
%hmin       Minimum thickness to use in calculations
%hmax       Maximum thickness to use in calculations
%Arraysize  Size of the array used to store thickness
%spacing    Take each point seperated by spacing
function getHC=f(struct,hmin,hmax,ArraySize,spacing)

    for i=1:spacing:length(struct.t_rs)
        %If the minimum thickness for this itertation is greater then the the minimum
        %value passed, then the minimum is used in determining
        %hole locations
        if(hmin<struct.hmin(i))
            Hmin=hmin;
```

```
        else
            Hmin=struct.hmin(i);
        end

        %If the maximum thickness is less then the the maximum
        %value passed, then the maximum passed is used.
        if(hmax>struct.hmax(i))
            Hmax=hmax;
        else
            Hmax=struct.hmax(i);
        end

        %call counting script
        holder=countHC_2(struct.h(1+(i-1)*ArraySize:i*ArraySize,:),Hmin,Hmax);
        counter{i}=holder;
        struct.numHoles(i)=holder.numHoles;
        struct.numCols(i)=holder.numCols;
    end %for
struct.counter=counter;
getHC=struct;
%************************************************************************
%   END       getHC
%************************************************************************

%========================================================================
%  START     countHC
%========================================================================
%Finds and counts the number of holes and columns given a surface h.
%The film thickness is turned into a gray-scale image and then
%analyzed by matlab's image processing toolbox
%
% Sample Call
%countHC(h,hmin,hmax)
%
%h      Film thickness array
%hmin   Minimum thickness used in gray-scale image
%hmax   Maximum thickness use in gray-scale image
function countHC=f(h,hmin,hmax)
    %Store the values passed in structure to be returned
    countHC.h=h;
    countHC.hmin=hmin;
    countHC.hmax=hmax;

    %First count columns
    %Create a gray-scale image using the maximum and minimum
    %values passed to create image
    gsImage=mat2gray(h,[hmin hmax]);
    countHC.gsImage=gsImage;

    %Create a binary image from the gray-scale
    binImage=im2bw(dcImage);

    %Get image properties, use 8-connected objects
```

```
%The binary image is searched using the algorithms presented
%by Haralick 'Computer and Robot Vision, Volume I'
%The binary image is generated by taking a threshold of the
%the gray-scale image. The image is then searched for 1's.
%The algorithm works row wise and as 1's are identified they
%are labeled in ascending order. The connectivity determines how
%adjacent points are treated in terms of labeling, 8 connected
%pixels are bested demonstrated by an example.
% a b c
% d e f
% g h i
%Consider the array of letters shown. When the value at e is 1, if
%any of the other letters are also valued 1 then they will be
%associated with the same object. For 4 connected pixles only objects
%that occur in b,d,f or h positions would be connected to e. This means
%that no diagonal attachment occurs.
%The image is searched, and as a one is discovered it is labeled
%with an existing label or a new label if a 8 connected object
%search comes up empty.
[binLabel,numCols]=bwlabel(binImage,8);
col_props=regionprops(binLabel,'basic');


%The number of columns and rows is corrected by
%removing objects that fall paritially in the domain.
%This correction is made due to the periodicity of the
%solution.
adjust_numc=0;
row_T=binImage(1,:);
row_B=binImage(end,:);
col_L=binImage(:,1);
col_R=binImage(:,end);

%Search the image to see if corner points occur, since they
%are the same obeject and will results in triple counting.
if(binImage(1,1)==1 & binImage(end,1)==1 ...
    & binImage(end,end)==1 & binImage(1,end)==1)
    adjust_numc=-3;
    chop=chopValues(row_T);
    row_T(chop)=0;
    chop=chopValues(row_B);
    row_B(chop)=0;
    chop=chopValues(col_L);
    col_L(chop)=0;
    chop=chopValues(col_R);
    col_R(chop)=0;
end

%Look at the upper and lower edges of the image
%compare them to find objects that overlap.
row=row_T+row_B;

%Find places where there is a boundary since this
```

```
%will results in double counting
vals=find(abs(diff(row))>1);
adjust_numc=adjust_numc-round(length(vals)/2);

%Check for left and right edge over lap
col=col_L+col_R;
vals=find(abs(diff(col))>1);
adjust_numc=adjust_numc-round(length(vals)/2);

%Correct count of columns
numCols=numCols+adjust_numc;
if(numCols<0)
    numCols=0;
end

h=countHC.h;

%Invert gray-scale image to count holes
gsImage_L=mat2gray(h,[hmin,hmax]);
gsImage_L=abs(gsImage_L-1);
countHC.gsImage_L=gsImage_L;

%make binary image for holes
binImage_L=im2bw(dcImage_L);

%count holes
[binLabel_L,numHoles]=bwlabel(binImage_L);
holes_props=regionprops(binLabel_L,'basic');

%Set up correction of holes
adjust_numh=0;
row_T=binImage_L(1,:);
row_B=binImage_L(end,:);
col_L=binImage_L(:,1);
col_R=binImage_L(:,end);

%check for corner points to avoid triple count
if(binImage_L(1,1)==1 & binImage_L(end,1)==1 &...
     binImage_L(end,end)==1 & binImage_L(1,end)==1)
    adjust_numh=-3;
    chop=chopValues(row_T);
    row_T(chop)=0;
    chop=chopValues(row_B);
    row_B(chop)=0;
    chop=chopValues(col_L);
    col_L(chop)=0;
    chop=chopValues(col_R);
    col_R(chop)=0;
end

%Check for over lap at top and bottom
row=row_T+row_B;
vals=find(abs(diff(row))>1);
```

```
    adjust_numh=adjust_numh-round(length(vals)/2);

    %Check for over lap on left and right edges
    col=col_L+col_R;
    vals=find(abs(diff(col))>1);
    adjust_numh=adjust_numh-round(length(vals)/2);

    %Correct count of holes
    numHoles=numHoles+adjust_numh;
    if(numHoles<0)
        numHoles=0;
    end

    %Store results
    countHC.image=gsImage;
    countHC.col_props=col_props;
    countHC.numCols=numCols;
    countHC.adjust_numc=adjust_numc;
    countHC.adjust_numh=adjust_numh;
    countHC.holes_props=holes_props;
    countHC.numHoles=numHoles;
    countHC.binImage_L=binImage_L;
    countHC.binImage=binImage;
%=========================================================================
%  END     countHC
%=========================================================================
```

A.3 Data Acquisition Script

```
%=========================================================================
%  START    getData
%=========================================================================
%This m file loads into a work space the data files passed.
%They are loaded into a structure and combined with the values from
%the pattern file and parameters structure.
%
%Sample Call
%getData(x_file,y_file,t_file,h_file,pat_file,...
%                    ArraySize,initLen,chop,params,case_flag)
%
%where:
%xfile          Name of the x mesh points
%yfile          Name of the y mesh points
%t_file         Name of the time file
%h_file         Name of the thickness file
%pat_file       Pattern of parameters
%ArraySize      Length of square arrays
%initLen        Initial Length of arrays
%chop           Value to chop extra values written
%               due to lines that are filled by
```

```
%               matlab with 0's
%params         Structure with:
%       .mu     Viscosity [Pa s]
%       .gamma  Interfacial Tension [N/m]
%       .h0     Initial Film thickness [m]
%       .l0     Minimum film thickness [m]
%       .Ep     Relative Permitivity [-]
%case_flag      A flag if set to 1 use LVDW scaling, else Electrostatic
%-----------------------------------------------------------------
function getData=f(x_file,y_file,t_file,h_file,vel_file,pat_file...
                   ,ArraySize,initLen,chop,params,case_flag)

%Load mesh point locations, thickness and velocity values
[getData.x,getData.y,getData.t,getData.h,getData.vel]=...
            getValues(x_file,y_file,t_file,h_file,vel_file,...
                        ArraySize,ArraySize,initLen,chop);

%Read in pattern file
pat_all=dlmread(pat_file);

%Reformat data from pattern file
getData.AL_d = ...
        reformMat(pat_all(1:initLen,:),1,ArraySize,...
                            ArraySize,initLen,chop,1);
getData.AU_d = ...
        reformMat(pat_all(initLen+1:2*initLen,:),1,ArraySize,...
                            ArraySize,initLen,chop,1);
getData.D_d = ...
        reformMat(pat_all(1+2*initLen:3*initLen,:),1,ArraySize,...
                            ArraySize,initLen,chop,1);
getData.V_d = ...
        reformMat(pat_all(1+3*initLen:end,:),1,ArraySize,...
                            ArraySize,initLen,chop,1);

%Get the parameters that are fixed in the domain
getData.mu=params.mu; getData.gamma=params.gamma;
getData.h0=params.h0; getData.l0=params.l0; getData.Ep=params.Ep;

%Find the maximum and minimum values of the electrode spacing (d),
%applied voltage (V), lower surface Hamaker constant (AL) and
%upper surface Hamaker Constant (AU)
getData.dmin=min(min(getData.D_d));
getData.dmax=max(max(getData.D_d));

getData.Vmin=min(min(getData.V_d));
getdata.Vmax=max(max(getData.V_d));

getData.ALmin=min(min(getData.AL_d));
getData.ALmax=max(max(getData.AL_d));

getData.AUmin=min(min(getData.AU_d));
getData.AUmax=max(max(getData.AU_d));
```

```
%Re-scale time based on the case flag either ES or LVDW
if(case_flag==1)
    holder=scale_LVDW(getData.mu,getData.gamma,getData.h0,getData.ALmin);
else
    holder=scale_ES(getData.gamma,getData.h0,getData.Ep,getData.Vmin);
end

%store time to scale by and create dimensional time
getData.tscl=holder.t; getData.t_rs=getData.t*getData.tscl;

%find the minimum and maximum film thicknesses for all time
for i=1:length(getData.t)
    getData.hmin(i)=min(min(getData.h(1+(i-1)*ArraySize:i*ArraySize,:)));
    getData.hmax(i)=max(max(getData.h(1+(i-1)*ArraySize:i*ArraySize,:)));
end;
%=====================================================================
%  END    getData
%=====================================================================

%*********************************************************************
%   START reformMat
%*********************************************************************
%This is an mfile that reshapes matrices of data from the fortran routines
%and puts them into matrices that will plot properly

%This mfile requires the definition of Mnew,Nnew and M,N where MxN are the
%current matrix dimensions and MnewxNnew are the desired dimensions
%This is for a single time step, so should be based on the grid used
%
%reformMat(u,t,Mnew,Nnew,arrayLen,chop,debug)
%
%where:
%u          Array to be reshaped
%t          Time vector (or vector of length equal to length
%           of array to be reformed).
%Mnew       Number of rows
%Nnew       Number of columns
%arrayLen   Initial array length
%chop       The number of points to cut off
%debug      If this flag is set output values
%=====================================================

function reshaped=f(u,t,Mnew,Nnew,arrayLen,chop,debug)

%Debug output
if(debug==1)
    fprintf('Reformating matrices\n')
    fprintf('Using Mnew %i, Nnew %i\n',Mnew,Nnew)
    fprintf('ArrayLen %i\n',arrayLen)
    fprintf('Chop Length %i\n',chop)
    fprintf('Matrix dimensions are: %i\n',size(u))
end
```

```
%first get times and locations of times
[len,wid]=size(u);

%this is the reformed u matrix
urf=zeros(length(t)*Mnew,Nnew);

%Iterate throught for each times step
for i=1:length(t)
    %Calculate the counters of locations in old array
    st=1+(i-1)*arrayLen;
    ed=i*arrayLen;

    %Calculate locations in new array
    ST=1+(i-1)*Mnew;
    ED=i*Mnew;

    %Load values from current vector and reshape
    temp=u(st:ed,:);
    temp=reshape(temp',1,(ed-st+1)*wid);

    %Chop extra values added by matlab during reading of file
    temp=temp(1:end-chop);

    %Put values in main array
    urf(ST:ED,:)=reshape(temp,Mnew,Nnew);
end

%Set values to return
reshaped=urf;

%Print an exit statement
if(debug==1)
    fprintf('\nFinished reshaping\n')
end
%*********************************************************************
%   END reformMat
%*********************************************************************
```

Appendix B

List of Cases Presented

B.1 Homogeneous Substrate Cases

B.2 Chemically Heterogeneous Substrate Cases

B.3 Electrical Heterogeneity Cases

B.4 Combined Heterogeneity Cases

h_0 [nm]	d [nm]	E [MV/m]
20	100	0
20	100	0.45
20	100	11.36
20	100	27.27
20	100	45.45
50	100	0
80	100	0

Table B.1: Homogeneous substrate case list

h_0 [nm]	d [nm]	$A_1[J]$	$A_2[J]$	E [MV/m]
20	100	1×10^{-19}	1×10^{-21}	0
50	100	1×10^{-19}	1×10^{-21}	0
80	100	1×10^{-19}	1×10^{-21}	0
20	100	1×10^{-19}	5×10^{-19}	0
20	100	1×10^{-19}	1×10^{-20}	0
20	100	1×10^{-19}	1×10^{-22}	0
10	50	1×10^{-19}	1×10^{-21}	0
40	50	1×10^{-19}	1×10^{-21}	0
45	50	1×10^{-19}	5×10^{-19}	0
45	50	1×10^{-19}	1×10^{-20}	0
45	50	1×10^{-19}	1×10^{-21}	0
45	50	1×10^{-19}	1×10^{-22}	0
20	100	1×10^{-19}	1×10^{-21}	0.45
20	100	1×10^{-19}	1×10^{-21}	11.36
20	100	1×10^{-19}	1×10^{-21}	27.27
20	100	1×10^{-19}	1×10^{-21}	45.45

Table B.2: Step change in effective Hamaker constant case list

h_0 [nm]	d [nm]	$A_1[J]$	$A_2[J]$	Ψ_{low} [V]	w [λ_c]	L_p [λ_c]	λ_c [μm]
20	100	1×10^{-19}	1×10^{-21}	0	1	2	7.77
20	100	1×10^{-19}	1×10^{-21}	0	1/2	1	7.77
20	100	1×10^{-19}	1×10^{-21}	0	1/4	1/2	7.77
25	100	1×10^{-19}	1×10^{-21}	0	1/2	2	12.14
50	100	1×10^{-19}	1×10^{-21}	0	1/2	2	48.54
80	100	1×10^{-19}	1×10^{-21}	0	1/2	2	124.3
90	100	1×10^{-19}	1×10^{-21}	0	1/2	2	157.3
20	100	1×10^{-19}	1×10^{-21}	0	0.15	2	7.77
20	100	1×10^{-19}	1×10^{-21}	0	0.25	2	7.77
20	100	1×10^{-19}	1×10^{-21}	0	0.35	2	7.77
20	100	1×10^{-19}	1×10^{-21}	0	0.45	2	7.77

Table B.3: Striping in effective Hamaker constant case list

h_0 [nm]	d_1 [nm]	$E_{p1}[MV/m]$	$E_{p2}[J]$	A [J]
75	100	72.72	7.27	1×10^{-19}
10	100	42.55	4.25	1×10^{-19}
45	60	121.1	56.59	1×10^{-19}
60	80	90.90	18.36	1×10^{-19}
90	120	222.2	22.22	1×10^{-19}

Table B.4: Step change in applied electric field case list

h_0 [nm]	d_1 [nm]	$E_{p1}[MV/m]$	$E_{p2}[MV/m]$	A $[J]$	w $[\lambda_c]$	L_p $[\lambda_c]$	λ_c $[\mu m]$
20	100	45.45	9.09	1×10^{-19}	1	2	5.06
20	100	45.45	9.09	1×10^{-19}	1/2	1	5.06
20	100	45.45	9.09	1×10^{-19}	1/4	1/2	5.06
20	100	45.45	9.09	1×10^{-19}	1.90	2	5.06
20	100	45.45	9.09	1×10^{-19}	1.70	2	5.06
20	100	45.45	9.09	1×10^{-19}	0.9	2	5.06
20	100	45.45	9.09	1×10^{-19}	0.3	2	5.06
20	100	45.45	9.09	1×10^{-19}	0.11	2	5.06
50	100	57.14	9.48	1×10^{-19}	1	2	3.57
80	100	76.93	9.83	1×10^{-19}	1	2	2.30

Table B.5: Striping in applied electric field case list

h_0 $[nm]$	d_1 $[nm]$	E_{p1} [MV/m]	E_{p2} [MV/m]	A_1 $[J]$	A_2 $[J]$	w $[\lambda_c]$	L_p $[\lambda_c]$	λ_c $[\mu m]$
20	75	63.49	45.45	1×10^{-19}	1×10^{-21}	1/2	1	7.77
20	75	15.87	11.36	1×10^{-19}	1×10^{-21}	1/2	1	7.77
20	75	0	0	1×10^{-19}	1×10^{-21}	1/2	1	7.77
20	75	63.49	45.45	1×10^{-21}	1×10^{-19}	1/2	1	7.77
20	75	15.87	11.36	1×10^{-21}	1×10^{-19}	1/2	1	7.77
20	75	0	0	1×10^{-21}	1×10^{-19}	1/2	1	7.77
20	75	63.49	45.45	1×10^{-19}	1×10^{-21}	1	2	7.77
20	75	63.49	45.45	1×10^{-19}	1×10^{-21}	1/2	1	7.77
20	75	63.49	45.45	1×10^{-19}	1×10^{-21}	1/3	2/3	7.77

Table B.6: Combined patterning case list

Appendix C

Instruction on running Fortran program

C.1 Introduction

The following document is a step by step instructional manual on running the thin film fortran program developed by David Crawford. The manual will follow the steps generally required to run a case using this program. The steps that will be presented are: picking a test case, building a pattern file, creating the configuration files, executing the program and finally using the Center for Excellence in Integrated Nanotechnology (CEIN) cluster. The instruction presented will be for running the code on a unix system although most of the commands will be shown in a form that should work in a DOS environment.

C.2 Picking a Test Case

The code running process starts with the selection of an appropriate test case. It is assumed that the program has been compiled and is now ready to run. The files required for compilation are listed in Appendix A. Now that the program is compiled a test case must be selected.

The first step in this process is deciding whether a pattern is desired on the lower surface. Even for cases where a pattern is not applied a pattern file is still required

Table C.1: Patterned problem parameters

Parameter	Symbol	Description
Electrode Spacing	d	The electrode spacing will be set in nano-meters.
Applied Electric Potential	ψ_{low}	The applied electric potential in Volts (V).
Effective Hamaker Constant at Lower surface	A_L	The effective Hamaker constant felt through the film due to interactions between the lower solid surface, surrounding gas and film through the film. Units Joules (J).
Effective Hamaker Constant at Upper surface	A_U	The effective Hamaker constant felt through the film due to interactions between the upper solid surface, surrounding gas and film through the film. Units Joules (J).

and will be discussed in the next section. The problem parameters will be divided into two groups: pattern parameters and static parameters. The problem parameters that are governed by the pattern file will be discussed first.

The program can incorporate patterning in both the applied electric field and effective Hamaker constant experienced between a surface, the gas above and the fluid through the film. The electric field patterning can be performed by varying the applied electric potential or electrode spacing, or both if so desired. The values that can be varied in the pattern file are listed in Table C.1. The program also requires a number of parameters that are uniform throughout the domain. These parameters will be called the static parameters and are listed in Table C.2.

Using the values listed in Tables C.1 and C.2 the desired run can be laid out. The end time for the simulation will only be of interest if a known time is required. The program is hard coded to check for convergence by looking at the linear norm of the film thickness to see if it decreases below 10^{-12}. This value can be changed by changing the value of the variable NORM_LIM. The code will execute until this

Table C.2: Static problem parameters

Parameter	Symbol	Description
Initial Film Thickness	h_0	Initial film thickness in nano-meters (nm).
Permittivity Ratio	ϵ_p	Permittivity ratio of the film to surrounding gas (dimensionless) (-).
Film Viscosity	μ	Fluid viscosity of the film in Pascal seconds (Pa s)
Interfacial Tension	γ	The interfacial tension between the fluid film and surrounding gas in Newtons per meter (N/m).
Minimum film thickness	l_0	The minimum thickness that the film is allowed to drain to. The model uses an absorbed layer model with close range Born like repulsion at the surfaces, this value is the point at which this force will dominate. The distance is in nanometers (nm).
Domain Size		The domain size as a multiple of the dominant wave length λ_c. This is a dimensionless value (-).
Scaling Flag		Flag to set which type of scaling, pressure or electrostatic, is used in solution.
Conjoining/Disjoining pressure flags		Flags to indicate which conjoining/disjoining pressure components will be used for the case in question. There are six flags for this.
Restart Flag		This flag tells the program that the run occurring is a re-start.
Initial Perturbation		The initial perturbation is a value less then one, that is applied as the initial perturbation to the system. It is split equally above and below the mean thickness. This is a dimensionless quantity.
Start time	t_{start}	The dimensionless start time. This value will be read from the data files if the case is a re-start.
End time	t_{end}	The dimensionless end time for the current run.

condition has been reached or 65,000 iterations have been performed.

C.3 Building a Pattern File

Now that a parameter list has been set, a pattern file must be generated. The pattern file will be created by the program PATTERN_BUILD. The process for pattern generation that is recommended is the creation of a pattern configuration file, the execution of the pattern building program and the confirmation of the file before extensive runs are pursued.

The processes of pattern building begins by creating a configuration file. The configuration file has the following form:

Pattern Name A_{L1} A_{L2} A_{U1} A_{U2} d_1

d_2 V_1 V_2 w w_2 n

Where *Pattern Name* is a 8 character name for the pattern file that will be created, A_{L1} is the first of the lower surface effective Hamaker constants in Joules, A_{L2} is the second of the lower surface effective Hamaker constants in Joules, A_{U1} is the first of the upper surface effective Hamaker constants in Joules, A_{U2} is the first of the upper surface effective Hamaker constants in Joules, d_1 is the first electrode spacing in meters, d_2 is the second electrode spacing in meters, V_1 is the first applied electric potential in Volts, V_2 is the second applied electric potential in Volts, w is the stripe width of the first values listed given in the number of grids, w_2 is the second stripe width is a whole number multiple of the grid width and n is the number of striped patterns to repeat. The pattern program will repeat the given pattern n times where the first stripe is split between the left and right edges of the domain. The stripes created are in the x direction.

There are some important notes on the format of the configuration file. Each value takes up 8 characters. For numbers, decimals and negative signs count for this total. The individual values should be separated by two spaces, and if scientific notation

is being used then D indicates the exponent. A sample configuration file is shown below, it is named $CPD1.DAT$.

```
 CPD1.PAT     1.00D-19  1.00D-19  1.00D-21  1.00D-21  100.0D-9
75.00D-9  5.0000D0  5.0000D0  3.0000D1  3.0000D1  1.0000D0
```

Now that a configuration file has been created, the pattern building utility PATTERN_BUILD can be called, with the configuration file passed to the program through the standard input. A sample call is shown below.

```
./PATTERN_BUILD < CPD1.DAT
```

Where ./ at the beginning is required by some unix systems to execute a program in the current directory, < allows the passing of parameters through the standard input and $CPD1.DAT$ is the name of the configuration file. The pattern building utility creates output and the output from this run is:

```
THE PARAMETERS READ ARE:CPD1.PAT              1.E-19  1.E-19  1.E-21
1.E-21 1.E-07  7.5E-08  5.  5.  30.  30.  1.
 THE VALUE OF STRIPES ARE:  1 1 1 1 1 1 1 1 1 1 1 1 1 1 1 0 0 0 0 0 0 0
 0 0 0 0 0 0 0 0 0 0 0 0 0 0 0 0 0 0 0 0 0 0 0 0 1 1 1 1 1 1 1 1 1 1 1
 1 1 1 1
 VALUES WRITTEN TO FILE: CPD1.PAT
```

The program begins by outputting the parameters it has read, then shows the pattern it will apply where 1's indicated value one will be used and 0's indicate value two will be used. It also gives the file name written too. After the file has been generated its values should be confirmed using the Matlab script getPattern.m.

C.4 Creating the Configuration Files

The pattern file required to run the program has been generated. The next step would be the creation of the general parameter and naming configuration files. The naming configuration file passes the names to be used for data files to be generated and the pattern file to be read. The parameter configuration file passes the static parameters discussed previously.

C.4.1 Name Configuration File

The name configuration file lists the names of the data files that will be generated and the pattern file to be read. The file should have the following format.

Paramater file name

X data file name

Y data file name

Thickness data file name

Velocity data file name

Time data file name

Re-start thickness data file

Re-start velocity data file

Pattern file to read

The file names should each be given on a separate line and must not exceed a length of 20 characters including punctuation. The parameter file has problem parameters written to it at the start of program execution. The x,y,thickness,velocity and time data files are filled with values at each time step. The re-start data files record the last time steps thickness and velocity profiles, to be used in the case of a restart. The pattern file is the name of a pattern file in the format created by the PATTERN_BUILD utility. A sample configuration file is shown below.

```
PARAM_D1
X_D1.DAT
Y_D1.DAT
H_D1.DAT
V_D1.DAT
T_D1.DAT
RS_D1_U
RS_D1_VEL
CPD1.PAT
```

C.4.2 General Parameter Configuration File

The general parameter file is a file listing a series of parameters that the program requires for execution. Some of the parameters are values that the code will use in the calculation and others are option flags that tell the program which portions of the code to use. In total 25 parameters will be read in by the program.

Name of Paramater	Notes
De-bugging flag	0 gives no output, 1 gives some output and 2 gives extensive run time output.
Variable time stepping flag	0 or 1 (1=use variable time stepping)
Relative permittivity ratio	
Applied electric potential One	In units of volts (V)
Applied electric potential Two	In units of volts (V)
Film viscosity	In units of Pascal seconds (Pa s)
Interfacial tension between the film and surrounding gas	In units of Newtons per meter (N/m)
Larger effective Hamaker constant at lower surface	In units of Joules (J)
Minimum film thickness	In meters (m)
Initial film thickness	In meters (m)
Electrode spacing one	In meters (m)
Electrode spacing two	In meters (m)
Applied perturbation	A value between 0-1 that represents the initial perturbation.
Starting time	Dimensionless time to start at
End time	Dimensionless ending time
Scaling flag	A value of 0 for LVDW based scaling and 1 for electrostatic based scaling
Electrostatic conjoining/disjoining pressure flag	Set to 1 to include this force
LVDW at lower surface conjoining/disjoining pressure flag	Set to 1 to include this force

Name of Paramater	Notes
Born like close range repulsion force at lower surface conjoining/disjoining pressure flag	Set to 1 to include this force
LVDW at upper surface conjoining/disjoining pressure flag	Set to 1 to include this force
Combined LVDW and Born like repulsion at lower surface flag	Set to 1 to include this force
Re-start flag	Set to 1 if the case is a re-start
Domain scaling factor	A value that will scale the domain by giving a total domain size of two times domain scaling times the dominant wave length
Largest Effective Hamaker constant on the upper surface	In Joules (J).

The values passed for voltage, effective Hamaker constant and electrode spacing will be over ridden by values in the pattern file. These values are used in the reporting of parameters and it is best to ensure that they are in agreement with the pattern file used. A sample general parameter configuration file is shown below.

```
2.0
1.0
2.5
5.0
5.0
1.0
0.038
```

```
1.0D-19
1.0D-9
20.0D-9
100.0D-9
75.0D-9
0.01
0.0
10.D7
1.0
1.0
1.0
1.0
1.0
0.0
0.0
0.0
1.0
1.0D-21
```

C.5 Executing the Program

The thin film program has been compiled and the required configuration files created, now the program can be executed. The program requires the names of the names and general parameter configuration files be passed to it on the command line so that it can execute. If we assume that the parameter files have the names NAMES and PARAMS, then the program can be called with:

```
./THINFILM NAMES PARAMS
```

The program name is given first and then the names of the two parameter files. For batch running it might be convenient to input the file names in another file and this can be done with a routing command using the < input.

C.6 Running on CEIN Unix Cluser

The majority of the runs performed in this thesis were executed on the CEIN cluster at the University of Alberta. The following is a sample unix shell script in bash shell used to submit a job.

```
#!/bin/bash
# set the shell scripting environment

#$ -l arch=lx26-amd64
#set the architecture as AMD64 processors

#Define the job name #$ -N D_D4
#Create a job name for the case submitted

#Change the working directory
cd /homes/dgc2/FORTRAN/SOURCE/DEVELOPMENT/CHEM_PAT/LOW_SURF/CHEM/COMBINED

#Execute fortran program
echo "Starting program execution: `date`"
echo "Starting case DD4: `date`"
../../../../THINFILM < D_D4

echo "Program execution complete: `date`"
```

The shell script would be passed to the cluster que using the command QSUB SCRIPT_NAME. After submitting a job you can check its status in the queue by entering the command QSTAT -u USER_NAME or see all cases in the queue QSTAT -f.